การปรับปรุงสภาพนำไฟฟ้าของเพอรอฟสไกต์ $La_{0.3}Sr_{0.7}Co_{0.9}Fe_{0.1}O_3$ สำหรับเซลล์เชื้อเพลิงออกไซด์ของแข็ง

นายอนุชา เกิดตรวจ

วิทยานิพนธ์นี้เป็นส่วนหนึ่งของการศึกษาตามหลักสูตรปริญญาวิทยาศาสตรมหาบัณฑิต
สาขาวิชาเคมี ภาควิชาเคมี
คณะวิทยาศาสตร์ จุฬาลงกรณ์มหาวิทยาลัย
ปีการศึกษา 2555

IMPROVEMENT OF ELECTRICAL CONDUCTIVITY OF $La_{0.3}Sr_{0.7}Co_{0.9}Fe_{0.1}O_3$ PEROVSKITES FOR SOLID OXIDE FUEL CELL

Mr. Anucha Koedtruad

A Thesis Submitted in Partial Fulfillment of the Requirements
for the Degree of Master of Science Program in Chemistry
Department of Chemistry
Faculty of Science
Chulalongkorn University
Academic Year 2012

อนุชา เกิดตรวจ : การปรับปรุงสภาพนำไฟฟ้าของเพอรอฟสไกต์ $La_{0.3}Sr_{0.7}Co_{0.9}Fe_{0.1}O_3$ สำหรับเซลล์เชื้อเพลิงออกไซด์ของแข็ง. (IMPROVEMENT OF ELECTRICAL CONDUCTIVITY OF $La_{0.3}Sr_{0.7}Co_{0.9}Fe_{0.1}O_3$ PEROVSKITES FOR SOLID OXIDE FUEL CELL) อ.ที่ปรึกษาวิทยานิพนธ์หลัก : ผศ.ดร.โสมวดี ไชยอนันต์สุจริต, 97 หน้า.

ศึกษาการนำไฟฟ้าและการซึมผ่านออกซิเจนของ $La_{0.3}Sr_{0.7}Co_{0.9}Fe_{0.1}O_3$ (LSCF) ที่โดปด้วย Ca^{2+}, Zn^{2+} และ Mg^{2+} ได้ตรวจสอบเอกลักษณ์ของวัสดุที่สังเคราะห์ด้วยเทคนิค XRD, XPS และ XAS จากการสังเคราะห์ LSCF ด้วยวิธิซิเทรตประยุกต์และศึกษาผลของอุณหภูมิในการซินเตอร์ พบว่า LSCF ที่ซินเตอร์ที่อุณหภูมิ 1200 องศาเซลเซียส มีการซึมผ่านของออกซิเจนสูงและมีโครงสร้างเป็นลูกบาศก์สมบูรณ์มากกว่า LSCF อื่นๆ และสามารถสังเคราะห์เพอรอฟสไกต์ $La_{0.3}Sr_{0.7-x}Ca_xCo_{0.9}Fe_{0.1}O_3$ และ $(La_{0.3}Sr_{0.5})_{1-x}Ca_xCo_{0.9}Fe_{0.1}O_3$ ได้โดยการแทนที่ La^{3+} และ Sr^{2+} ด้วย Ca^{2+} โดย $La_{0.3}Sr_{0.7-x}Ca_xCo_{0.9}Fe_{0.1}O_3$ จะแสดงโครงสร้างเฟสเดี่ยวของลูกบาศก์เพอรอฟสไกต์เมื่อ X เท่ากับ 0 ถึง 0.5 ขณะที่ $(La_{0.3}Sr_{0.5})_{1-x}Ca_xCo_{0.9}Fe_{0.1}O_3$ แสดงโครงสร้างเฟสเดี่ยวของลูกบาศก์เพอรอฟสไกต์และเตตระโกนอล เมื่อ X เท่ากับ 0 ถึง 0.2 และ X เท่ากับ 0.3 ถึง 0.4 ตามลำดับ ในงานนี้วิจัยนี้ $La_{0.3}Sr_{0.5}Ca_{0.2}Co_{0.9}Fe_{0.1}O_3$ มีค่าการนำไฟฟ้าสูงสุดเนื่องจากมี IS Co^{4+} และ HS Co^{3+} มาก เพื่อพัฒนาการซึมผ่านออกซิเจนของ $La_{0.3}Sr_{0.5}Ca_{0.2}Co_{0.9}Fe_{0.1}O_3$ ไอออน Co^{3+} และ Fe^{3+} จะถูกแทนที่ด้วยไอออน Zn^{2+} และ Mg^{2+} เพื่อให้ได้ $La_{0.3}Sr_{0.5}Ca_{0.2}Co_{0.9-y}M_yFe_{0.1}O_3$ และ $La_{0.3}Sr_{0.5}Ca_{0.2}(Co_{0.9}Fe_{0.1})_{1-y}M_yO_3$ (M คือ Zn^{2+} และ Mg^{2+} โดย Y เท่ากับ 0 ถึง 0.05) ผลการทดลองพบว่าสามารถสังเคราะห์ $La_{0.3}Sr_{0.5}Ca_{0.2}Co_{0.9-y}Zn_yFe_{0.1}O_3$ ที่แสดงโครงสร้างเฟสเดี่ยวของลูกบาศก์ได้เมื่อ Y มีค่าเท่ากับ 0 ถึง 0.03 และอัตราการซึมผ่านออกซิเจนจะเพิ่มขึ้นเมื่อเพิ่มปริมาณ Zn^{2+} เนื่องจากมี high spin $Co^{2+,3+}$ และช่องว่างออกซิเจนเพิ่มขึ้น.

ภาควิชา เคมี ลายมือชื่อนิสิต

สาขาวิชา เคมีอนินทรีย์ ลายมือชื่อ อ.ที่ปรึกษาวิทยานิพนธ์หลัก

ปีการศึกษา 2555

5372373623: MAJOR CHEMISTRY

KEYWORDS: PEROVSKITE/ LANTHANUM COBALTITE/ CATHODE MATERIAL/ ELECTRICAL CONDUCTIVITY/ OXYGEN PERMEATION

ANUCHA KOEDTRUAD: IMPROVEMENT OF ELECTRICAL CONDUCTIVITY OF $La_{0.3}Sr_{0.7}Co_{0.9}Fe_{0.1}O_3$ PEROVSKITES FOR SOLID OXIDE FUEL CELL. ADVISOR: ASST. PROF. SOAMWADEE CHAIANANSUTCHARIT, Ph.D., 97 pp.

The electrical conductivity and oxygen permeation of Ca^{2+}, Zn^{2+} and Mg^{2+}-doped $La_{0.3}Sr_{0.7}Co_{0.9}Fe_{0.1}O_3$ (LSCF) were investigated. The synthesized materials were characterized by XRD, XPS and XAS. LSCFs were synthesized by modified citrate method and studied for the effect of sintering temperature. LSCF sintered at 1200 ^oC showed the higher oxygen permeation rate and more idealized cubic structure than others. By replacing La^{3+} and Sr^{2+} ions of LSCF with Ca^{2+} ions, $La_{0.3}Sr_{0.7-x}Ca_x Co_{0.9}Fe_{0.1}O_3$ (X = 0 - 0.7) and $(La_{0.3}Sr_{0.7})_{1-x}Ca_xCo_{0.9} Fe_{0.1}O_3$ (X = 0 - 0.4) were successfully synthesized. $La_{0.3}Sr_{0.7-x}Ca_xCo_{0.9}Fe_{0.1}O_3$ showed pure perovskite phase with primitive cubic form when X = 0 - 0.5 whereas $(La_{0.3}Sr_{0.7})_{1-x}Ca_xCo_{0.9}Fe_{0.1}O_3$ exhibited pure perovskite phase with primitive cubic and tetragonal forms when X = 0-0.2 and X = 0.3 - 0.4, respectively. $La_{0.3}Sr_{0.5}Ca_{0.2}Co_{0.9}Fe_{0.1}O_3$ showed the highest electrical conductivity in this work due to a lot of IS Co^{4+} and HS Co^{3+}. To improve oxygen permeation of $La_{0.3}Sr_{0.5}Ca_{0.2}Co_{0.9}Fe_{0.1}O_3$, Co^{3+} and Fe^{3+} ions were replaced with Zn^{2+} and Mg^{2+} ions to obtain $La_{0.3}Sr_{0.5}Ca_{0.2}Co_{0.9-y}M_yFe_{0.1}O_3$ and $La_{0.3}Sr_{0.5}Ca_{0.2}(Co_{0.9}Fe_{0.1})_{1-y} M_yO_3$ (M = Zn^{2+}, Mg^{2+}, Y = 0 - 0.05). Only $La_{0.3}Sr_{0.5}Ca_{0.2}Co_{0.9-y}Zn_yFe_{0.1}O_3$ (Y = 0 - 0.03) were achieved as pure perovskite phase with primitive cubic structure. The oxygen permeation rate was increased with increasing Zn^{2+} content because high spin $Co^{2+,3+}$ and oxygen vacancies were increased.

Field of Study: Chemistry Student's Signature

Academic Year: 2012 Advisor's Signature

ACKNOWLEDGEMENTS

The author would like to express deepest gratitude to his family especially father, mother and sister for their support, love, care and encouragement.

The success of this thesis can be attributed to the extensive support, valuable advices, kindness and encouragement from Assistant Professor Dr. Soamwadee Chaianansutcharit, author’s advisor. The author really wishes to express greatest gratitude to her. He also would like to gratefully thank Associate Professor Dr. Koichiro Mitsuke from Institute for Molecular Science, and Professor Yoshida from Nagoya University, Japan, JENESYS program advisors, for their kindness, help and valuable advices during he stayed in Japan.

Moreover, the author wishes to express appreciation to Assistant Professor Dr. Warinthorn Chavasiri, Assistant Professor Dr. Boosayarat Tomapatanaget, and Dr. Siriporn Larpkeattavorn for serving as the chairman and members of this thesis committee, respectively, for all of their valuable advices and comments in the research.

The author would like to thank Office National Research Council of Thailand (NRCT), Center of Excellence on Petrochemical and Materials Technology, and Graduate School Chulalongkorn University for financial support. In addition, student exchange grant from the Japan-East Asia Network of Exchange for Students and Youths (JENESYS) program 2011, Institute for Molecular Science, Japan, and MOU scholarship between Chulalongkorn University and Institute for Molecular Science, are also acknowledged. Finally, he would like to thank the members of Material chemistry and Catalysis Research Unit for their help and friendship.

CONTENTS

Page

Page

LIST OF TABLES

LIST OF FIGURES

Page

Page

Page

Page

LIST OF ABBREVIATIONS

SOFC	Solid oxide fuel cell
DMFC	Direct methanol fuel cell
PEMFC	Proton exchange membrane fuel cell
AFC	Alkaline fuel cell
PAFC	Phosphoric acid fuel cell
MCFC	Molten carbonate fuel cell
MIEC	Mixed ionic electronic conductor
XRD	X-ray diffractometry
XPS	X-ray photoelectron spectroscopy
XAS	X-ray absorption spectroscopy
XANES	X-ray absorption near edge spectroscopy
SEM	Scanning electron microscopy
$J\mathrm{o}_2$	Oxygen permeation rate
J	Oxygen permeation flux
T	temperature
^{o}C	degree Celsius
K	Kelvin
ml	milliliter
hrs	hours
min	minute
g	gram
mm	millimeter
cm	centimeter
μm	micrometer
Å	angstrom
σ	specific conductivity
E_a	activation energy
%	percent
a, c	unit lattice parameter
t	tolerance factor

r	ionic radius
L	length
I	current
T	thickness
V	voltage
W	width
E_b	binding energy
E_c	conduction band energy
BE	binding energy
HS	high spin
LS	low spin
IS	intermediate spin
ORR	oxygen reduction reaction
LMCT	ligand to metal charge transfer

CHAPTER I

INTRODUCTION

Nowadays, the global demand in energy is increasing while energy sources such as petroleum are limited. Moreover, global-warming phenomenon caused by the emission of green house gases, i.e. CO, CO_2 and NO_x, becomes more serious. Therefore, efficient and environmental friendly energy sources such as biomass, solar cell, wind power and fuel cells are gaining attention from scientists.

1.1 Fuel cells [1-2]

Fuel cells, energy conversion devices, can convert the chemical energy of fuel gases to electrical energy and heat without combustion. Their conversion efficiencies are much higher than the conventional thermomechanical method. The operation scheme of fuel cell is similar to that of battery, i.e. electrical generation from the electrochemical reaction between reactants, a fuel gas (hydrogen), an oxidant gas (oxygen), electrodes and ion conducting electrolyte. Unlike the battery in requiring the recharging status, fuel cells can continuously operate as long as the fuel and the oxidant are supplied to the electrodes.

Fuel cells are classified by the type of electrolytes as summarized in Table 1.1. The first six types are operated at low temperatures (50–210 °C) resulting in their relatively low electrical generation efficiency of 40–50%. On the other hand, the high operating temperatures (600–1,000 °C) of the latter two types promote high electrical generation efficiency of 45–60%. Nowadays, proton exchange membrane fuel cell (PEMFC) and solid oxide fuel cells (SOFC) are of research interested because PEMFC is suitable for motor vehicles while SOFC is suitable for high power generating station. Moreover, some fuel cell companies have pushed effort on development of SOFC as a power source of motor vehicles.

Table 1.1 Types of fuel cells [3]

Fuel cell type	**Electrolyte**	**Operating temperature (^{o}C)**	**Fuel**
Alkaline fuel cell (AFC)	Potassium hydroxide (KOH)	50-200	Pure hydrogen or hydrazine
Direct methanol fuel cell (DMFC)	Polymer	60-200	Liquid methanol
Phosphoric acid fuel cell (PAFC)	Phosphoric acid	160-210	Hydrogen from hydrocarbons and alcohol
Sulphuric acid fuel cell (SAFC)	Sulphuric acid	80-90	Alcohol or impure hydrogen
Proton-exchange membrane fuel cell (PEMFC)	Polymer, proton exchange membrane	50-80	Less pure hydrogen from hydrocarbons or methanol
Solid polymer fuel cell (SPFC)	Solid sulphonated polystyrene	90	Hydrogen
Molten carbonate fuel cell (MCFC)	Molten salt such as nitrate, sulphate, carbonates	630-650	Hydrogen, carbon monoxide, natural gas, propane, marine diesel
Solid oxide fuel cell (SOFC)	Stabilized zirconia and doped perovskite	600-1000	Natural gas

1.1.1 Solid oxide fuel cells (SOFCs) [1]

SOFC differs in many respects from other fuel cells. Firstly, it composes all solid materials. Secondly, it operates at temperature as high as 1000°C, significantly hotter than other fuel cell. And finally, since its components are all solid characters, there has no fundamental restriction on the cell configurations which are usually tubular cells (rolled tubes) and flat-plate cells. SOFC offers a clean, pollution-free technology to produce electricity at high efficiency. It has a lot of advantages over traditional energy conversion systems such as high efficiency, reliability, modularity, fuel adaptability, long life time, and very low levels of toxic gas emission as shown in Table 1.2. Quiet and vibration-free operation of SOFC also eliminates noise usually related to conventional power generation systems. In addition to the high operating temperature (600-1000 ^{o}C) of SOFC, natural gas can reform within the cell itself eliminating the need for expensively external reformer system. SOFC can also be combined with gas turbines for co-generated system in order to improve the efficiency which can be up to 70%. Due to such advantages, SOFC is best suited for large-scale to small-scale power generations and also portable/emergency power generators. Examples of the most needed uses are:

- The high reliability of power source on computer facilities, communication facilities, and high technology manufacturing facilities.
- Minimization of emission gases in urban areas, industrial facilities and airports zones with stricted emission standards or in waste treatment plants. By SOFC, biological waste gases is converted directly to electricity and heat with minimal environment intrusion.

Table 1.2 The amount of released gases from fossil-fuel plant and SOFC.

	Released gases (kg/year)					
	SO_x	**NO_x**	**CO**	**CO_2**	**Organic**	**Particles**
Fossil-fuel plant	12,740	18,850	12,797	1,840.020	213	228
SOFC	0	0	32	846,300	0	0

1.1.2 Operation of SOFCs [1]

SOFC consists of two electrodes (one anode and one cathode) which sandwich around ceramic electrolyte. The operation scheme of SOFC is shown in Figure 1.1. Hydrogen gas is fed into the anode as a fuel while oxygen gas is fed into the cathode as the oxidant. On the anode, the oxygen concentration is low leading to the migration of oxygen ions from the electrolyte to react with hydrogen gas. Consequently, electrons (e^-) are released and move toward the cathode via electrical connection between these electrodes resulting in useful electrical power. On the cathode, the oxygen gas is reduced by electrons into oxide ions which diffuse to the anode through the electrolyte. The diffusion of oxide ions is driven by the oxygen pressure gradient and the difference in electrical potential due to the imbalance charge between the anode and the cathode sides. Byproducts of the system are only water, CO_2 and heat. The SOFC reactions are shown below:

Anode: $H_2 + O^{2-} \rightarrow H_2O + 2e^-$ or $CO + O^{2-} \rightarrow CO_2 + 2e^-$ (1.1)

Cathode: $1/2O_2 + 2e^- \rightarrow O^{2-}$ (1.2)

Cell: $H_2 + 1/2O_2 \longrightarrow H_2O$ or $CO + 1/2O_2 \longrightarrow CO_2$ (1.3)

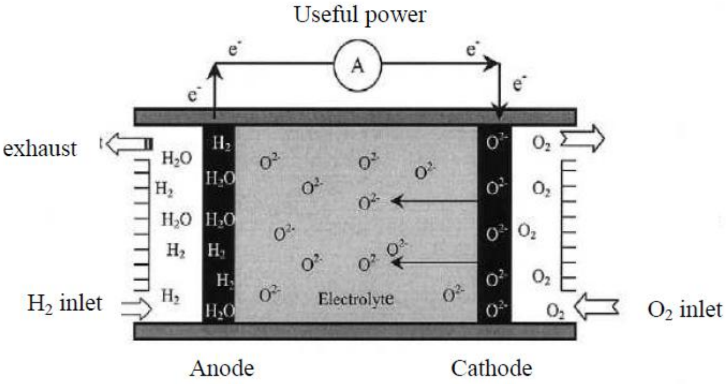

Figure 1.1 SOFC operation scheme

1.1.3 Components of SOFCs [1]

Two electrodes and solid electrolytes are main components of SOFC. Each component functions severally and must meet certain requirements such as:

- Thermal stability during cell operation and cell fabrication
- Proper conductivity
- Non-reactivity with other cell components
- Closely thermal expansion to prevent cracking during the cell fabrication and cell operation.
- Dense electrolyte to avoid the direct combination between fuel gas and oxygen.
- Porous anode and cathode to provide more active sites
- Fabricability
- Low cost

1.1.3.1 Cathode

Cathode materials have to meet the following requirements [1,2,4]:

- High electronic and ionic conductivity.
- Chemical stability in encountered environment during cell use.
- Thermal expansion matching with other cell components.

- Non-reactivity with electrolytes or interconnections where the cathode comes into contact.
- Sufficient porosity to provide more triple-phase boundaries (TPB) where the reaction takes place, and to facilitate transportation of molecular oxygen from the gas phase to the cathode/electrolyte interface.

To satisfy these requirements, metal oxides with the ABO_3 perovskite structure, where A is alkaline or alkaline earth metal, B is transition metal and O is oxygen, are good candidates as cathode materials because they show high ionic and electronic conductivity and also thermal stability. For high temperature SOFC (working temperature is 800-1,000 °C), lanthanum strontium manganite, $La_{1-x}Sr_xMnO_3$ (LSM) and lanthanum calcium manganite, $La_{1-x}Ca_xMnO_3$ (LCM) are usually used because of their great thermal expansion matching with electrolytes and good conducting properties. For low temperature SOFC (working temperature is 600-800 °C), lanthanum strontium cobaltite ferrite, $La_{1-x}Sr_xCo_{1-y}Fe_yO_3$ (LSCF) and barium strontium cobaltite ferrite, $Ba_{1-x}Sr_xCo_{1-y}Fe_yO_3$ (BSCF) are available because they exhibit higher conductivity than LSM and LCM in this temperature range. Beside the metal oxide materials, a composite material between metal oxide cathode and electrolytes is an alternative choice of electrode because it improves electrode properties by increasing the TPBs. The reaction mechanism at the cathode side is explained as following equations [5]:

1) Adsorption of O_2 onto the cathode surface

   $$O_2\ (g) \longrightarrow O_2\ (ad) \qquad (1.4)$$

2) Charge-transfer from transition metals to O_2 (ad) on cathode surface

   $$O_2\ (ad) + 2e^- \longrightarrow O_2^{2-}\ (ad) \qquad (1.5)$$

3) Dissociation of O_2^{2-} (ad) at high temperature

   $$O_2^{2-}\ (ad) + 2e^- \longrightarrow 2O^{2-}\ (ad) \qquad (1.6)$$

4) Diffusion of O^{2-}(ad) from cathode surface into the bulk

   $$O^{2-}\ (ad) \longrightarrow O_o^x\ (perovskite) \qquad (1.7)$$

5) Transfer of O^{2-} to the electrolyte

   $$O_o^x\ (perovskite) \longrightarrow O_o^x\ (electrolyte) \qquad (1.8)$$

1.1.3.2 Electrolyte [1,2,6]

Electrolyte materials must exhibit purely ionic conductivity (with no electronic conductivity) and stable in such environment. They allow the migration of oxide ions from the cathode to the anode, thus, they will expose both reducing atmosphere on the anode and oxidizing atmosphere on the cathode.

Metal oxides with fluorite structure, i.e. yttria stabilized zirconia (YSZ), samarium doped ceria (SDC), gadoliniums doped ceria (GDC) and bismuth yttrium oxide (BYO), and with perovskite structure, i.e. lanthanum strontium gallium magnesium (LSGM), have been widely studied as the electrolyte. Among these materials, Figure 1.2, YSZ is the most favorable electrolyte due to availability and cost. Even though YSZ has low ionic conductivity, yttrium oxide (Y_2O_3) dopant stabilizes cubic zirconia (ZrO_2) at high temperature to produce oxygen vacancies through the following defect reaction:

$$Y_2O_3 \xrightarrow{ZrO_2} 2Y'_{Zr} + 3O_O^{\times} + V_O^{\bullet\bullet} \qquad (1.9)$$

For the crystalline array of ZrO_2, each zirconium ion has surrounded by two oxide ions while in Y_2O_3, yttrium ion has surrounded only by 1.5 oxide ions. By substitution of Y in Zr, oxygen vacancies in the structure will be produced. These vacancies promote the oxide ion conductivity in YSZ.

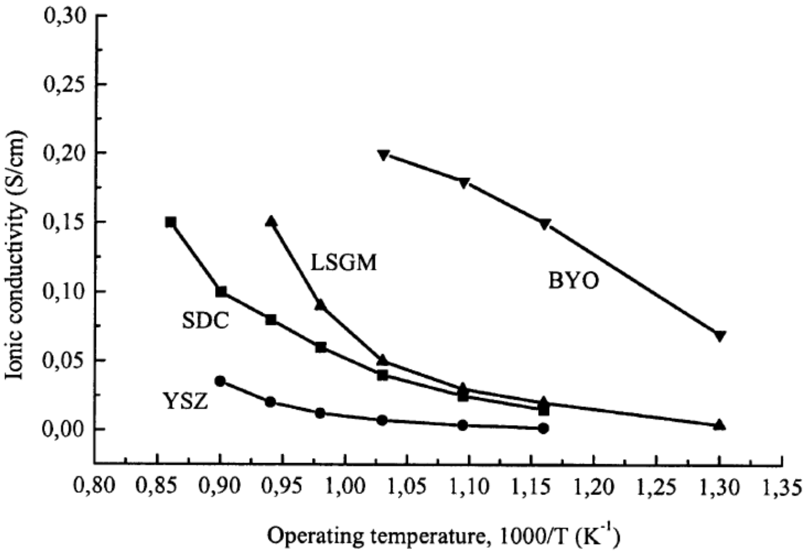

Figure 1.2 Ionic conductivity of electrolyte materials as a function of temperature [1]

1.1.3.3 Anode [1,2,4]

Since the oxidation reaction of H_2 and CO gases according to the reaction 1.10 and 1.11 takes place at the anode side, anode materials should be stable in the reducing environment of the fuels, electronically conducting and sufficiently porous to allow the transportation of the fuels to and the transportation of H_2O and CO_2 products away from electrolyte/anode interface where the oxidation reaction occurs.

$$O^{2-}{}_{(s)} + H_{2\,(g)} \longrightarrow H_2O_{(g)} + 2e^- \qquad (1.10)$$

$$O^{2-}{}_{(s)} + CO_{(g)} \longrightarrow CO_{2(g)} + 2e^- \qquad (1.11)$$

Nickel metals (alternately cobalt or ruthenium) are commonly used as anode materials under reducing conditions. However, the high thermal expansion of nickel is still a problem for using with YSZ electrolyte. Nickel can be sintered by the high operating temperature resulting a decreasing of porosity. These problems can be solved by using the composite electrode between YSZ and nickel oxide, NiO, which is subsequently reduced to nickel metal under the reducing condition. The composite electrode inhibits the sintering of nickel particles, reduces the thermal expansion coefficient closed to that of YSZ electrolyte, and provides excellent adhesion of the anode with YSZ electrolyte

1.1.3.4 Interconnection [1,2]

Interconnection functions electric contact to the cathode and also protects the cathode from reducing environment of fuels from the anode side. Requirements of interconnection include the following.

- High electronic conductivity.
- Stability in both oxidizing and reducing atmospheres because it exposes to both oxygen gas on the cathode side and fuels on the anode side.
- Thermal expansion close to that of the cathode and the electrolyte.
- Minimal reactivity with the cathode and electrolyte.
- High density with no porosity to prevent the direct gas mixing between fuel gas and oxygen gas.

Doped lanthanum chromite ($LaCrO_3$) can be used as the interconnection. This material shows *p*-type conductivity because of small polaron hopping. Its conductivity can be improved by substitution either La or Cr ions with lower valence metal ions e.g. Ca, Mg, Sr, etc.

1.2 Perovskite [7]

1.2.1 Crystal structure of perovskite

Perovskites are inorganic compounds which crystal structures relate to perovskite mineral, $CaTiO_3$. The chemical formula of perovskites is defined as ABX_3 where A is alkaline or alkaline earth metal, B is mostly transition metal and X is often O and also F or Cl is possible. Ideal cubic perovskite consists of A and O ions forming a cubic close packed lattice. The B ion occupies in octahedral holes created by O ions. The three dimensional structure of perovskite has a net of corner sharing $[BO_6]$ octahedra with the A ion in 12-fold coordination between the polyhedra (Figure 1.3). The A ion is in position ½,½,½, the B ion in 0,0,0 and the O ion in ½,0,0; 0,½,0; 0,0,½. However, the ideal cubic perovskite structure is hardly found and $CaTiO_3$ itself is also slightly distorted. Perovskite oxide is more attractive family because it exhibits surprising variety of properties, e.g. magnetic and electrical properties, and it is flexible to accommodate several elements. Due to these properties, the perovskite has great impact for industrial application, especially SOFC and ferroelectric-concerned industries.

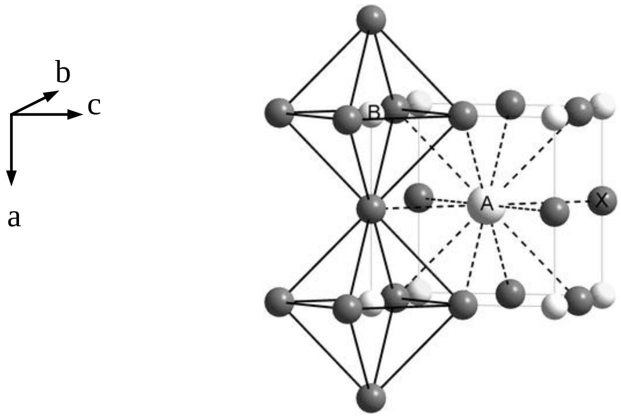

Figure 1.3 Perovskite structure [8]

Perovskite structure is very flexible because A and B ions can be varied resulting in the large number of compounds with perovskite or related structures. There are three main factors causing the distortion of perovskites: the size of A and B cations, nonstiochiometric composition, and Jahn-Teller effect.

1) Effects of cation size

For ideal cubic perovskites (Figure 1.4), the B-O distance equals to *a*/2 (*a* is a cubic unit cell parameter) while the A-O distance equals to $a/\sqrt{2}$. Thus, the relationship between ionic radii and the unit cell parameter can be described by following equations:

$$a = 2\times B - O = 2\times(r_B + r_O) \qquad (1.1)$$

and $$a = \sqrt{2}\times(r_A + r_O) \qquad (1.2)$$

The ratio of two expressions for the *a* is called Goldschmidt's tolerance factor (*t*).

$$t = \frac{\sqrt{2}\times(r_A + r_O)}{2\times(r_B + r_O)} = \frac{(r_A + r_O)}{\sqrt{2}\times(r_B + r_O)} \qquad (1.3)$$

where r_A, r_B and r_O are the ionic radii of A, B and O ions, respectively.

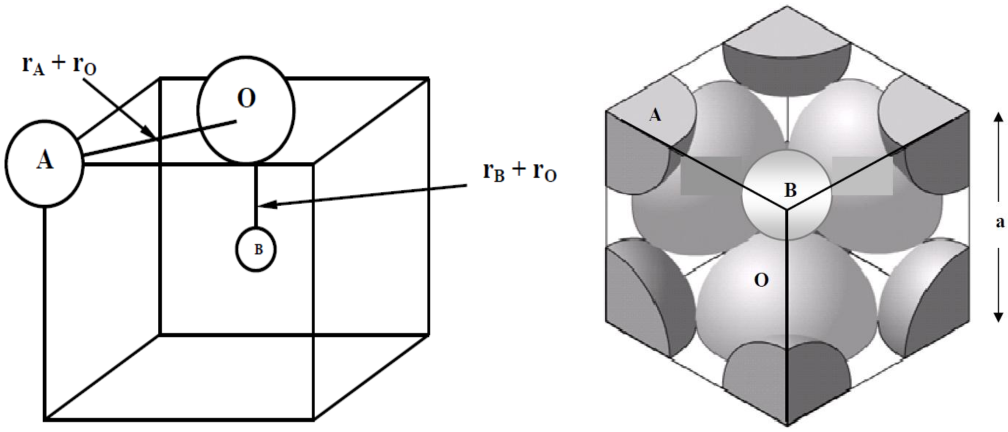

Figure 1.4 The relationship of ionic radii in a cubic unit cell basing on the assumption that all atoms touch one another as shown in the right picture

The Goldschmidt's tolerance factor is used to measure the degree of distortion from ideal cubic perovskite structure. The ideal cubic perovskite must has $t = 1$ such as $SrTiO_3$ (r_A = 1.44 Å, r_B = 0.605 Å, and r_O = 1.40 Å). If the A ion is smaller than the ideal value, the *t* value is smaller than 1. Consequently, [BO_6] octahedra tilt to fill space leading to the distorted perovskite structure. However, the cubic structure is still stable if $0.89 < t < 1$. But lower values of *t* indicate lower symmetry of crystal structure. For example, $GdFeO_3$ has orthorhombic structure with $t = 0.81$ ($r_A = 1.107$ Å and $r_B = 0.78$ Å), Figure 1.5a. With the t value < 0.8, ilmenite structure is formed. On the other hand, if the t value is higher than 1 due to a large A or a small B ion, the perovskite with hexagonal structure is stable, for example $BaNiO_3$ has $t = 1.13$ ($r_A = 1.61$ Å and $r_B = 0.48$ Å). In this case, the atomic layers are stacked in a hexagonal manner leading to face sharing of $[BO_6]$ octahedra, see Figure 1.5b. However, the calculation of the t is based on ionic radii. Since perovskites are not completely ionic compounds and the t value also depends on what value is chosen for the ionic radii, the tolerance factor is only a rough estimation.

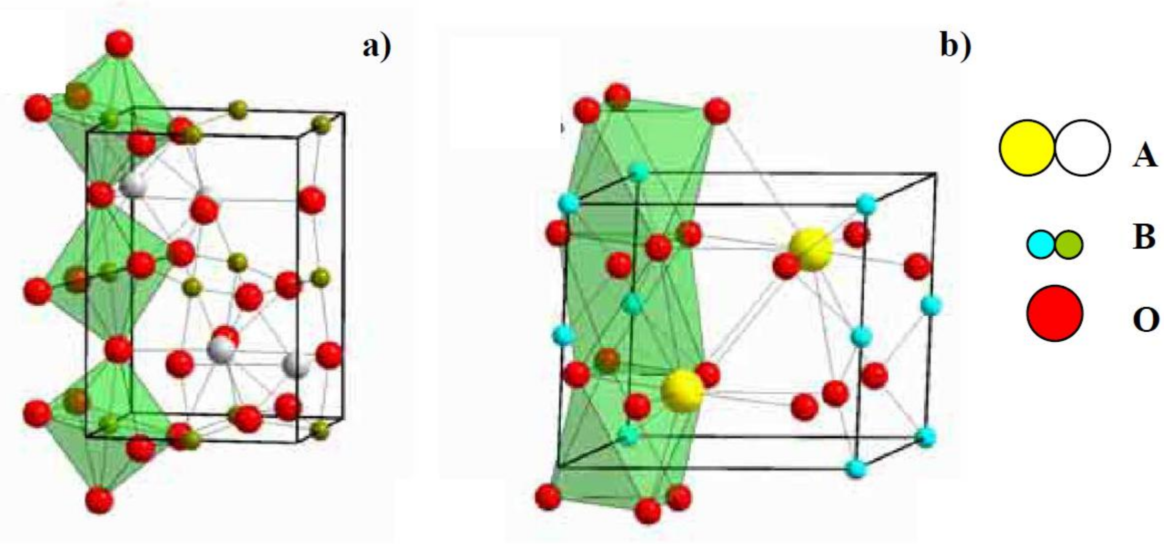

Figure 1.5 Perovskite structure with **a)** orthorhombic symmetry **b)** hexagonal symmetry.

2) Effects of nonstoichiometric composition

A nonstoichiometric composition from ideal ABO_3 is often due to oxygen deficiency. The oxygen deficiency is accomplished by substituting ions of similar size but different valence, or thermal reduction of B ions. For example, some of La^{3+} ions in $LaBO_3$ are replaced by Sr^{2+} ions to obtain $La_{1-x}Sr_xBO_3$. Consequently, oxygen vacancies are created in order to maintain charge neutrality of the structure. Another example is $SrFeO_3$. The oxygen content can be varied between 2.5 and 3 by heating the sample in either oxidizing or reducing environment leading to the formation of some FeO_5 square pyramids. Also the oxidation state of Fe ions changes from 4+ to 3+ leading to the increase in ionic radii. These effects cause the distortion of perovskite structure.

3) Jahn – Teller effects

The distortion of some perovskites may be due to Jahn – Teller active B ions. For example in $LnMnO_3$ (Ln = La, Pr or Nb) with Mn^{3+} ions, the $3d^4$ electrons divide up into t_{2g}^{3} and e_g^{1}. The odd number of electrons in the e_g orbital causes an elongation of the $[MnO_6]$ octahedron.

1.2.2 Properties of perovskites

Due to the variety of structures and chemical compositions, perovskites illustrate a large variety of properties. The well-known properties of perovskites are mixed ionic and electronic conductivity (MIEC), oxygen permeation and magnetic property. Based on these properties, perovskites are chosen as components for SOFC.

1.2.2.1 Electronic conductivity (σ_e) [9]

As given that B cations locate in octrahedral holes generated by O anions. The nuclear charge of B cations attracts anionic *p* orbitals strongly. Because of polarizability of anions, the anionic *p* orbitals can spread towards the t_{2g} orbitals of B cations and both orbitals might overlap (Figure 1.6). So, *d* electrons of the t_{2g} orbital can delocalize to the t_{2g} orbital of adjacent B cations through the anionic *p* orbitals. The electronic conductivity in perovskite compounds concerns with mobile charge carriers (excess electrons/electron holes) along the B–O–B chains. The higher amount of the mobile charge carriers is, the higher conductivity is. The mobile charge carrier is typically generated by the substitution of trivalent cations with divalent cations at the A site. This case results in a decrease in total positive charge in the structure. As a result the imbalance charge is compensated either by the increase in valence of the B cation (electronic compensation) or the formation of oxygen vacancies (ionic compensation). However, the relative proportion between two types of the charge compensation is unpredictable because it depends on several factors such as temperature, pO_2 and material-specific. If the electronic compensation is predominant, the electron holes (B^{4+}) are formed. These holes act as hopping sites for electrons. The electronic conductivity due to the electron hole is call *p*-type conductivity. On the other hand, if the formation of oxygen vacancies is predominant, excess electrons due to the reduction of B cations are generated. These electrons are loosely bound by a weak electrostatic attraction leading to free or conducting electrons. The electronic conductivity due to the excess electron is call *n*-type conductivity. Beside, the excess electrons can be also formed by thermal reduction of B cations at high temperature.

In addition to the doping of aliovalent cation on the A site, the mobile charge carriers can be generated by a charge-disproportionation effect as shown in reaction 1.12 [10-11,25].

$$2B^{3+} \longrightarrow B^{2+} + B^{4+} \qquad (1.12)$$

For example, the electronic conductivity of $La_{1-x}Sr_xFeO_3$ and $LaMnO_3$ is improved by the charge disproportionation of Fe^{3+}/Fe^{5+} and Mn^{2+}/Mn^{4+} ion pairs, respectively. This effect depends on entropy-driven, temperature and the relative stability of electron configuration of B cations.

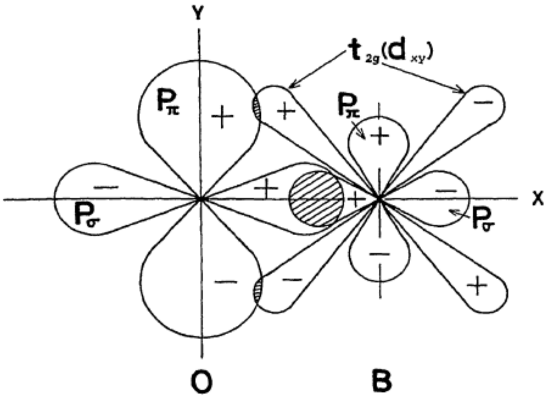

Figure 1.6 Covalent bonds between anionic *p* orbital and t_{2g} orbital of B cations.

The electronic conductivity of materials can be calculated from an electrical conductivity (σ). The electrical conductivity is the summation of electronic and ionic conductivity (σ_i), as follow:

$$\sigma = \sigma_e + \sigma_i \qquad (1.4)$$

The σ_i can be calculated from oxygen permeation flux. Either contribution may predominate depending on the material, its purity, and temperature.

1.2.2.2 Ionic conductivity (Oxide ion conductivity, σ_i) [9,12]

As earlier mentioned, oxygen vacancies are formed either by aligovalent substitution of A cations and thermal reduction of B cations. These vacancies promote great ionic conductivity because the oxide ion diffusion takes place by exchange of oxide ion position with an adjacent vacancy along octahedral edge. The diffusion has to pass through a ‘‘saddle point’’ built by two A cations and one B cation (Figure 1.7).

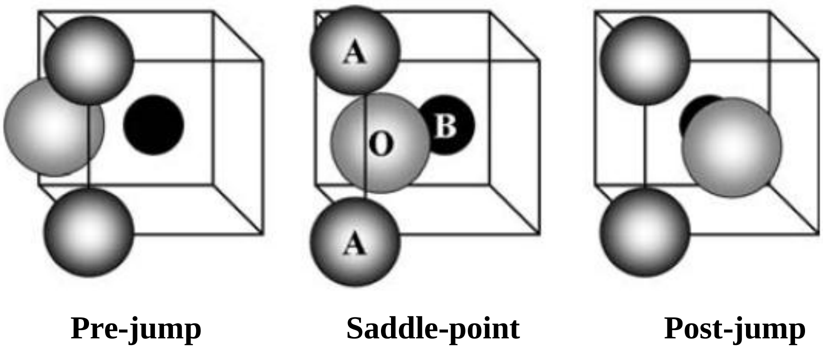

Figure 1.7 The migration of the oxygen ion pass through the saddle point.

The maximum ionic radius of mobile ions to pass through the saddle point is represented by critical radius (r_{cr}) calculated from equation 1.5.

$$r_{cr} = \frac{a_0(\frac{3}{4}a_0 - \sqrt{2}r_B) + r_B^2 - r_A^2}{2(r_A - r_B) + \sqrt{2}a_0} \qquad (1.5)$$

where r_A and r_B are the ionic radius of the A ion and B ion, respectively, and a_0 is the pseudo cubic lattice parameter.

For general perovskite, the critical radius is about 1.05 Å. Since the radius of the oxide ion is 1.4 Å in the six-fold coordination and is 1.36 Å in the three-fold coordination, the thermally outward relaxation of the cations (away from the mobile oxide ion) is important for the migration of oxide ion. This relaxation depends on following factors.

1) The cationic mass and size

Reduction of the cationic mass increases the amplitude of thermal relaxation. In addition, large B cations and small A cations achieve larger r_{cr}, therefore, enhances the oxide ion conductivity.

2) Structural stress

A stress-free lattice is also another factor for fast oxygen ion conductivity. The stress-free lattice is provided by cubic symmetry which tolerance factors close to 1. The increase in lattice distortion affects a high degree of anisotropy of oxide ions in the structure. The jump of oxygen ions is hampered by this effect. Hence, substitutions of cations must be done in a considerate manner, i.e. the host and substituting cations must have similar size in order to maintain the distortion-free structure.

3) Metal–oxygen bonding energy

Further factor which supports oxide ion diffusion is the weak bond strength of B-O bond. The interaction between the B cation and oxide ions increases with the valence state of the B cation. Therefore, the best oxide ion conductivities are expected to be within the $A^{3+}B^{3+}O_3$ perovskites.

The ionic conductivity, σ_i, can be calculated from permeation fluxes (J) through a perovskite pellet of the thickness L by means of the Wagner equation [13]:

$$\sigma_i = \frac{16F^2JL}{TR\ln(pO_2'/pO_2'')} \qquad (1.6)$$

Where F is Faraday constant, R is gas constant, T is temperature, P_{O_2}' and P_{O_2}'' are the oxygen partial pressure in the poor and rich oxygen compartment, respectively.

1.2.2.3 Oxygen permeation [13-14]

Due to the ionic conductivity, perovskites can be developed as oxygen-permeated discs. The oxygen permeation is driven by a difference in oxygen partial pressure between rich and poor oxygen compartments, while overall charge neutrality was maintained by a counter balancing flux of electron (and/or electron holes), see Figure 1.8. Mechanism for oxygen permeation through the perovskite disc can be described as follows:

1) At high oxygen pressure side of the disc, oxygen gas transfers to a disc surface and interacts with B cations at oxygen vacancy sites along grain boundaries to produce adsorbed O_2. The adsorbed O_2 can be held on the disc surface by both chemical

interaction between the B cation and O_2, and physical interaction between the grain boundary and O_2.

2) The adsorbed O_2 is reduced and dissociated giving adsorbed O^{2-}. This specie incorporates in the surface layer of the disc and diffuses to low oxygen pressure side via bulk oxygen vacancies. At this side, the adsorbed O^{2-} is oxidized to produce adsorbed O_2 and electrons which transfer back to the B cation.

3) The adsorbed O_2 is desorbed and transferred from the disc surface to the gas phase by low oxygen pressure.

These processes do not need for an external current but the sample disc requires the mixed ionic and electronic conductivity to permit the reverse flow of the electrons needed for the oxygen dissociation. The oxygen permeation (J_{O_2}) through the sample disc with the thickness *d* relates to the permeation flux (*J*) as equation 1.7 [15].

$$J = \frac{J_{O_2}}{d}\ln\left(\frac{P''_{O_2}}{P'_{O_2}}\right) \qquad (1.7)$$

The oxygen permeation flux depends on the disc thickness and the difference in oxygen partial pressure between the two compartments.

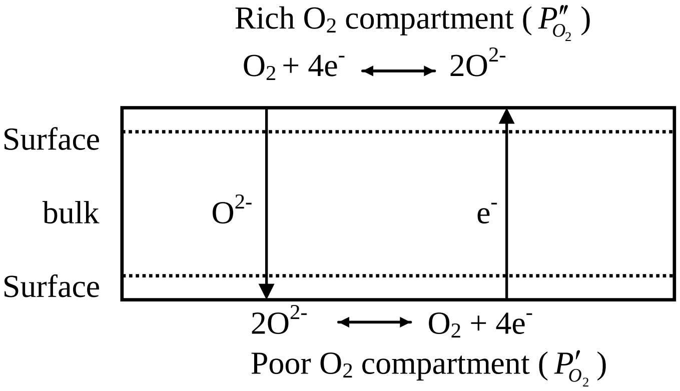

Figure 1.8 Oxygen transport during oxygen permeation [14]

1.2.2.4 Magnetic property [16]

In ideal cubic perovskites, two B ions share one oxide ion forming B-O-B chain with angle of 180°. The molecular bonding orbital of octahedral symmetry is mainly occupied by electrons of oxide ions, while the antibonding orbital is partially occupied by 3*d* electrons of B cations. This effect leads to the localization of *d* spin from one of B cations to the others through oxide ion.

There are two spins in the oxygen ion site, the up-spin state (+) and down-spin state (-). Because of the overlap of wave functions, either of *p* electrons from these state hops to one of B ions. The remaining unpaired *p* electron on the oxygen ion then exchanges directly with the electron of other B ions with an exchange interaction. The resultant interaction between the B ions coupled through oxygen ions is antiferromagnetic or ferromagnetic. For examples, $LnMnO_3$ exhibits both antiferromagnetic and ferromagnetic behavior depending on the amounts of Mn^{3+} and Mn^{4+} ions. Ferromagnetic behavior is observed in the range from 25 to 35% Mn^{4+}. A similar kind of behavior was found for the combination of Co^{3+} and Co^{4+}, but the Cr and Fe compounds were found to be antiferromagnetic

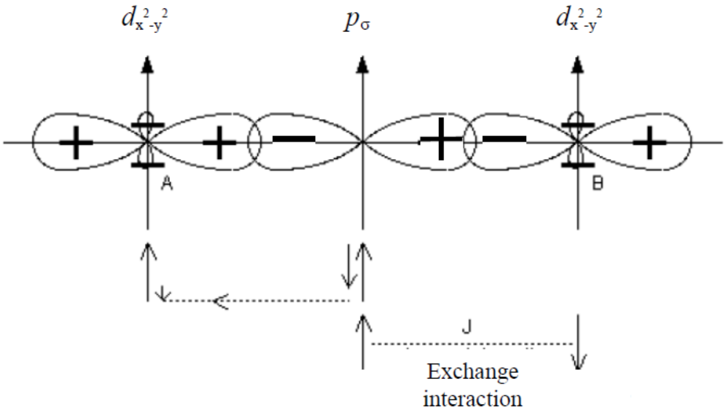

Figure 1.9 Schematic representation of the exchange interaction between B ions and oxide ions [16].

1.2.3 Perovskite synthesis [17]

There are many methods to synthesize perovskite such as a conventional solid-state method and solution methods e.g. sol-gel process and co-precipitation process.

1.2.3.1 Solid-state method

A solid state method is the most common method for synthesizing perovskite compounds. Starting materials, i.e. metal oxides, metal carbonates and metal hydroxides, are directly mixed and fired at high temperature for a long period so that metals can diffuse and react with others to form desired perovskite structure. This method is very easy to handle because it is simple and no solvent used. However, the homogeneity and the purity of the powder are poor due to mechanical mixing of starting materials and grinding processes. Furthermore, this method requires high temperature leading to high energy consumption. Other problems may arise when some components in the compounds (i.e. Cr and Pb) vaporize during the process resulting nonstoichiometric component and toxicity.

1.2.3.2 Solution method

A solution method is a traditional method for producing perovskite compounds. This technique provides higher purity, homogeneity and stoichiometry in perovskite oxide than the solid state reaction. Moreover, perovskite powders made from solution method are very fine particles resulting high surface area for oxygen reduction reaction. In addition, this method generates porous easily in material and enhances ability to control particle size. The popular solution methods are sol gel, coprecipitation and hydrothermal methods.

1) Sol-gel technique

This technique is an important wet chemical route for synthesizing novel ceramic oxide materials, especially perovskite oxide. It concerns with solution preparation, network formation between metal ions and chelating agents, gel dehydration and gel combustion. Generally, metal nitrates will be used as starting material because of their high water solubility. The chelating agents, such as ethylenediaminetetraacitic acid (EDTA), citric acid, alanine and glycine, are added into the solution in order to prevent partial metal segregation which can form in the case of different stabilities of metal ions in the solution. This method provides high chemical homogeneity.

The formation of metal framework consists of the metal centers and oxygens, namely oxo (M-O-M) or hydroxo (M-OH-M) bridges. For example, the metal-citrate framework of $LaMnO_3$ perovskites is shown in Figure 1.10 [18].

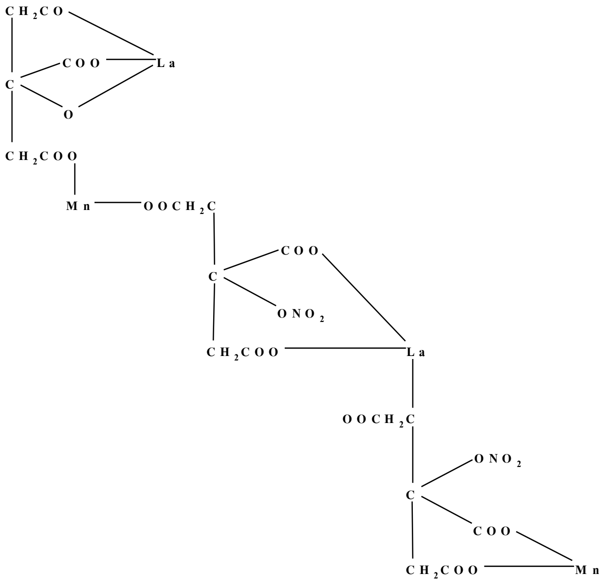

Figure 1.10 The manganese citrate-nitrate precursor.

2) Co-precipitation

The co-precipitation is generally used for synthesizing nano-materials. This process associates with mixing an aqueous solution containing the desired cations and another solution acting as a precipitation agent. The precipitation of product under high super saturation condition, filtration, drying and thermal decomposition follow to the desired product. Physical properties of the product depend on pH, mixing rates, temperatures and concentrations. This method provides stoichiometric and high purity product. Moreover, low calcine and sintering temperature are required because of the high dispersion of different metals in the precipitate and the small particle size in the range of nanometers, that facilitates in sinterbility.

3) Hydrothermal synthesis

This method is commonly used for synthesis advanced mixed oxide, a compound with specific functionality such as pigments for electronics. This method requires temperature in the range of boiling point of water and pressure can be as high as 15 MPa. Hence, this method does not need calcinations and can be used as assistant in sol-gel method for controlling particle sizes. The advantages of this method are low material cost, easy to control the particle size and shape, and stoichiometric amount of compositions.

1.2.3.3 Calcination [19]

The calcination, a thermal treatment process, is applied to solid materials for bringing up a thermal decomposition, phase transformation or removal of volatile fraction. This process normally occurs at temperature below a melting point of materials and mainly aims to oxidize metal to metal oxide and also eliminate volatile constituents such as water or organic compounds.

1.2 3.4 Sintering [20]

The sintering process is a thermal treatment of powders or compact discs in order to increase their density and strength by fusing together of adjacent particles. This process is sometime called densification.

When a powder is sintered, neck forms between the particles that results in the increase in density of materials. The growth of the neck relates to the transport of matter (Figure 1.11). Normally, sintering is occurred in three sequential stages. During the initial stage, the necks form at the point of particle contact and the particles usually approach each other except the individual particles are still distinguishable. Next, for the intermediate stage, the neck grows larger resulting in the formation of interconnected pore structure. And the final stage begins when the pores pinch off and are isolated. After a long period, these pores are finally disappeared.

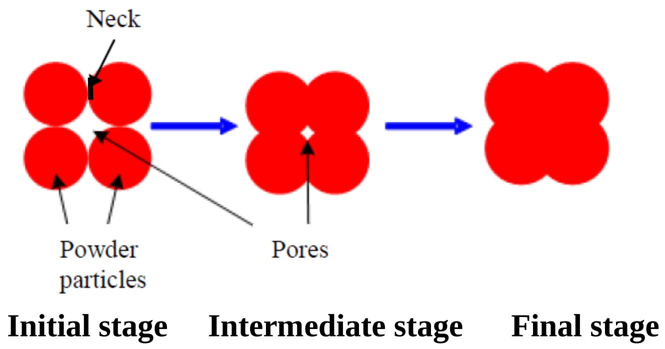

Figure 1.11 The models for three stages of sintering [21]

1.3 Literature reviews

SOFCs have been developing as electrical generator in plants and automotive because of its high power generation efficiency and fuel flexibility. However, the cell use is limited by the high working temperature range (800-1,000 ^{o}C) affecting to the degradation of constructing materials. The development of SOFC for working at low temperature (500-800^{o}C) is being of great interest. Unfortunately, the lower the working temperature is, the higher the polarization resistant of the cell, resulting in severely deactivated efficiency. In order to improve its efficiency at reduced temperature, cathode materials with high catalytic and conducting properties are required.

Mixed metal oxides with A_2BO_4- and ABO_3-type perovskites, such as La_2NiO_4, $Ba_{1-x}Sr_xCo_{1-y}Fe_yO_3$ (BSCF) and $La_{1-x}Sr_xCo_{1-y}Fe_yO_3$ (LSCF) are widely studied because of their great electronic and ionic conductivity properties. The high efficiency of low temperature SOFC is recently revealed by the use of LSCF cathode with doped cerea electrolytes. Therefore, there are a lot of publications concerning the properties of such cathode as a function of synthesized method, sintering temperature, composition and also types of dopant.

Mineshige et al.[22] studied the properties of $La_{1-x}Sr_xCoO_3$ ($0 \leq x \leq 0.7$). They found that the excess charge induced by substituting La^{3+} with Sr^{2+} ions in this compound was predominantly compensated by increasing oxidation state of Co ions from Co^{3+} to Co^{4+} when $X < 0.5$, and by the creation of oxygen vacancy when $X > 0.5$. Moreover, when $X = 0.6$-0.7, $La_{1-x}Sr_xCoO_3$ exhibited more idealized cubic than other compositions. Also an increase in Sr^{2+} ion content and measuring temperature resulted in a decrease of tilting of CoO_6 octahedra and the increase in Co-O-Co angle (θ) closely to 180^{o}. The increasing of θ enhanced the orbital overlapping ability between O2*p* and Co3*d* orbital. This effect decreases the energy gap between an occupied O2*p* valence band and an unoccupied Co3*d* conduction band, which, therefore, enhancing electronic conductivity of materials.

Hueso et al. [23] investigated the correlation of structural and electronic defects in $La_{1-x}Sr_xCoO_3$ ($X = 0, 0.5$) by means of Co and O K-edge x-ray absorption spectroscopy. After doping of Sr^{2+} ions, the oxidation state of Co ions did not change, which still presented as 3+. This observation indicated that the formation of oxygen vacancies for charge neutrality was predominant. On the other hand, the electronic configuration of Co^{3+} ions changed from low spin to high spin, indicating a decreasing of coordination number of Co^{3+} ions due to the formation of oxygen vacancy and a good alignment of Co-O-Co chain. Both effects decreased ligand field splitting energy in molecular orbital of CoO_6 octahedral symmetry resulting in such high spin electronic configuration.

Cherry et al.[24] investigated the oxygen vacancies in La_{1-x} $(AE)_xCoO_3$ (AE = Ca, Mg, Sr, Ba). They found that replacing La^{3+} ions with Ca^{2+} and Sr^{2+} ions provided higher oxygen vacancies than the substitution of La^{3+} ions with other ones. These vacancies supported oxide ion conductivity. Moreover, the high oxide ion conductivity was also due to the smaller size of Ca^{2+} ions.

Petric et al. [25] studied the electrical conductivity of $La_{0.3}Sr_{0.7}Co_{1-y}Fe_yO_3$ (Y = 0.0 – 1.0) and $La_{1-x}Sr_xCo_{0.2}Fe_{0.8}O_3$ (X = 0.0 – 1.0). The result revealed that $La_{0.3}Sr_{0.7}Co_{0.9}Fe_{0.1}O_3$ (LSCF3791) showed the highest conductivity comparing to other LSCFs but it decreased gradually with temperature.

Onuma et al. [26] examined the oxygen vacancies in $La_{1-x}AE_xCrO_3$ (AE = Sr, Ca and X = 0.1-0.3) by a thermogravimetric analysis. It was shown that the oxygen vacancy increased with increasing Ca^{2+} and Sr^{2+} ion content and there were no difference in oxygen vacancy values between Ca-doped and Sr-doped compounds under the same dopant conditions.

Ding et al. [27] investigated the cathodic overpotential of $La_{0.7}AE_{0.3}CuO_3$ (AE = Ca, Sr, Ba) by an impedance spectroscopy. They found that the lowest cathodic overpotential was obtained from $La_{0.7}Ca_{0.3}CuO_3$. The lowest cathodic overpotential implied to the high oxide ion conductivity and electronic property of the sample.

Hung et al. [28] measured the electrical conductivity of $La_{1-x}Ca_xFeO_3$ (X = 0-0.5) in the temperature range of 100-800 ^oC. It was found that the electrical conductivity jumped about two orders of magnitude after doping Ca^{2+} ions in 15 mol%.

Xia et al. [29] reported that the electrical conductivity of $Sr_2Fe_{1-x}Zn_xNbO_6$ was improved by substituting of Fe^{3+} ions with Zn^{2+} ions. The electrical conductivity reached the highest value when Zn = 0.2.

Lakshminarayanan et al. [30] examined oxygen vacancies of $La_{0.6}Sr_{0.4}(Co_{0.18}Fe_{0.72}X_{0.1})O_3$ (X = Zn, Cu, Ni) by thermogravimetric analyses (TGA). It was shown that $La_{0.6}Sr_{0.4}(Co_{0.18}Fe_{0.72}Zn_{0.1})O_3$ (LSCF-Zn) exhibited the best results in oxygen vacancy creation at low temperature of 400 °C and a much higher vacancy content at 700 ◦C comparing to the undoped compound and also the Cu and Ni-doped ones. Consequently, LSCF-Zn exhibited excellent performance on oxidation activity.

Vijayanandhini et al. [31] reported that the substitution of Mn^{3+} ions with Zn^{2+} ions in $La_{0.6}Sr_{0.4}Mn_{1-y}Zn_yO_3$ is chargely compensated by the formation of oxygen vacancy. These vacancies increased with increasing Zn^{2+} ion concentration.

Datta et al. [32] studied the relationship between a unit cell free volume and an oxide ion conductivity of $La_{0.9}Sr_{0.1}Ga_{1-x}Mg_xO_3$ (X = 0.05 - 0.2). They found that the unit cell free volume increased with increasing Mg^{2+} ion content. This was because of a larger size of Mg^{2+} ions (ionic radius (r) = 0.72 Å) than Ga^{3+} ions (r = 0.62 Å). The increase in unit cell free volume resulted in easier movement of oxide ions through the saddle point leading to the high oxide ion conductivity.

Choi et al. [33] investigated oxide ion conductivity of $La_{0.9}Ba_{0.1}Ga_{1-x}Mg_xO_3$ (X = 0.05-0.2). They found that the oxide ion conductivity increased significantly with increasing Mg^{2+} contents. This was because the oxygen vacancies were created for charge neutrality after replacing of $Ga^{3+}$with Mg^{2+} ions.

From the literatures, LSCF3791 is one of the most interesting compounds in LSCF group because of not only its high electrical conductivity but also its high oxygen vacancies and more idealized cubic structure as expected from the reports of Mineshige and Hueso. Moreover, doping of Ca^{2+}, Mg^{2+} and Zn^{2+} ions can improve the conducting properties of perovskites. Since, there has no report concerning about the properties of structural distortion, electronic and structural defects, and oxygen permeation of LSCF3791, this work is aimed to investigate such properties of LSCF3791 and improve its electrical conductivity and oxygen permeation by doping Ca^{2+}, Mg^{2+} and Zn^{2+} ions in the structure.

1.4 The objectives of the thesis

1.4.1 To synthesize Ca, Zn, Mg-doped LSCF3791 perovskites with ABO_3 structure as below:

- $La_{0.3}Sr_{0.7-x}Ca_xCo_{0.9}Fe_{0.1}O_3$ (X = 0-0.7)
- $(La_{0.3}Sr_{0.7})_{1-x}Ca_xCo_{0.9}Fe_{0.1}O_3$ (X = 0-0.5)
- $La_{0.3}Sr_{0.5}Ca_xCo_{0.9-y}(Zn, Mg)_yFe_{0.1}O_3$ (Y = 0-0.05)
- $La_{0.3}Sr_{0.5}Ca_x(Co_{0.9}Fe_{0.1})_{1-y}(Zn, Mg)_yO_3$ (Y = 0-0.05)

1.4.2 To prepare sample discs and characterize their structure and surface morphology by X-ray diffractometry (XRD) and scanning electron microscopy (SEM), respectively.

1.4.3 To measure electrical conductivity and oxygen permeation of the sample discs.

1.4.4 To examine the distortion of structure, the electronic and structural defects of samples by X-ray absorption spectroscopy (XAS) and X-ray photoelectron spectroscopy (XPS).

1.5 Scope of the work

Firstly, LSCF3791 was synthesized by a modified citrate method at different sintering temperatures of 1100 ^{o}C, 1200 ^{o}C and 1300 ^{o}C. The effects of sintering temperature on structural distortion, surface morphology, structural and electronic defects, electrical conductivity and oxygen permeation were investigated. All LSCF3791s were characterized for single phase ABO_3 structure by XRD, for surface morphology by SEM and for structural distortion and the defects by XAS and XPS. The properties of LSCF3791 were examined for electrical conductivity and oxygen permeation. LSCF3791 with more idealized cubic and highest oxygen permeation was chosen for the further study.

Secondly, Ca^{2+} ions were introduced into the A site to obtain $La_{0.3}Sr_{0.7-x}Ca_xCo_{0.9}Fe_{0.1}O_3$ (X = 0-0.7) and $(La_{0.3}Sr_{0.7})_{1-x}Ca_xCo_{0.9}Fe_{0.1}O_3$ (X = 0-0.5). The synthesized samples were characterized for the single phase ABO_3 structure by XRD, for structural distortion and the defects by XAS and XPS. The properties of samples were investigated for electrical conductivity and oxygen permeation. The one that shows the highest electrical conductivity was chosen for further study.

Finally, Zn^{2+} and Mg^{2+} ions were introduced into the B site to obtain $La_{0.3}Sr_{0.5}Ca_xCo_{0.9-y}(Zn, Mg)_yFe_{0.1}O_3$ and $La_{0.3}Sr_{0.5}Ca_x(Co_{0.9}Fe_{0.1})_{1-y}(Zn, Mg)_yO_3$ (Y = 0-0.05). Single phase ABO_3 structure, structural distortion and the defects were investigated by XRD and XAS, XPS, respectively. The properties of samples were studied for electrical conductivity and oxygen permeation.

1.6 Assumption

1. Doping of Ca^{2+} ions can improve electrical conductivity of LSCF3791 in the temperature range of 600-800 ^{o}C because Ca^{2+} ions are smaller than Sr^{2+} ions resulting in structural distortion from ideal cubic perovskite structure (Figure 1.12b). With increasing temperature to 600-800 ^{o}C, the unit cell expands and ideal cubic structure is resulted (Figure 1.12c) leading to high electrical conductivity.

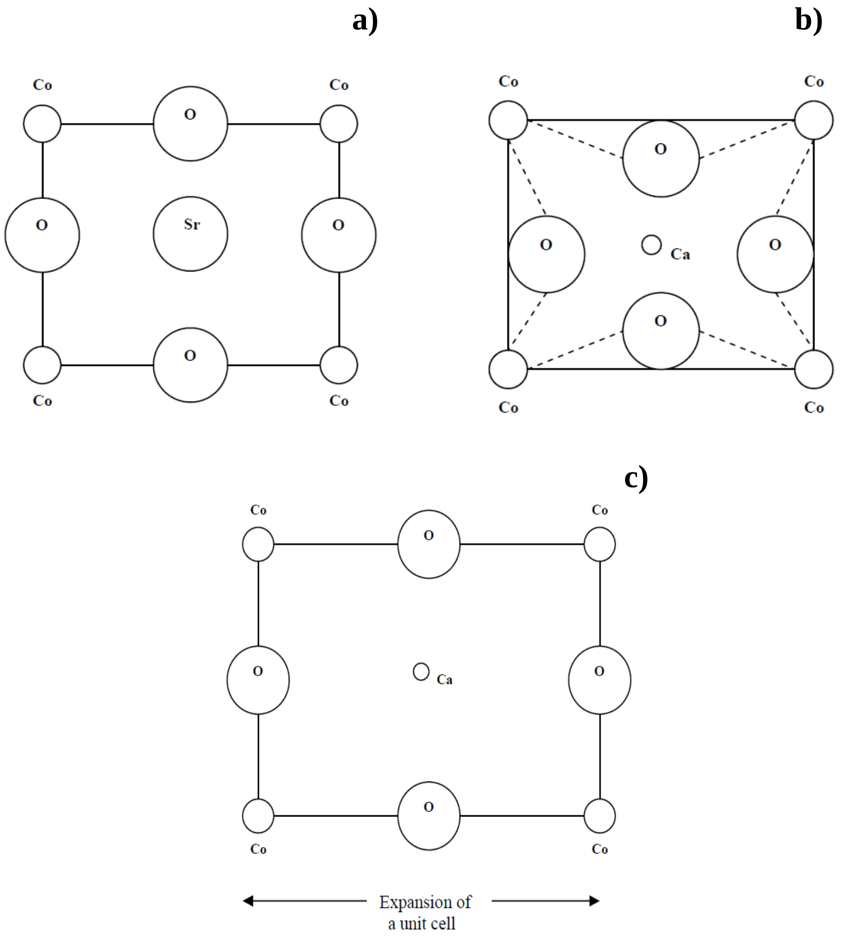

Figure 1.12 Proposed structural models of LSCF3791 a) before substitution of Sr^{2+} ions with Ca^{2+} ions b) after substitution of Sr^{2+} ions with Ca^{2+} ions c) structure of Ca-doped LSCF3791 at temperature of 600-800 °C

2. Doping of Ca^{2+} ions can improve oxygen permeation of LSCF3791 in the temperature range of 600-800 °C because of the transformation to ideal cubic structure in such temperature range. The ideal cubic structure leads to more random distribution of oxygen vacancy [30]. Moreover, the relaxation at the saddle point of Ca-doped LSCF3791 occurs easily due to the less ionic mass of Ca^{2+} ions than that of Sr^{2+} ions. These effects support the ionic conductivity resulting in high oxygen permeation.

3. Doping of Zn^{2+} and Mg^{2+} ions can improve oxygen permeation of LSCF3791 due to two main reasons. Firstly, doping of these ions generates more oxygen vacancies in the structure for charge neutrality because of their unchangeable oxidation state which only presents as 2+. Secondly, weak electrostatic force between cations and oxide ions due to the larger size and lower oxidation state of these ions than that of Co^{3+} and Fe^{3+}

ion;m’s supports the movement of oxide ions leading to high oxygen permeation (ionic radii (*r*) of Zn^{2+} = 0.74 Å, Mg^{2+} = 0.72 Å, Co^{3+} = 0.54 Å and Fe^{3+} = 0.64 Å [29,33-35]).

4. Doping of Zn^{2+} and Mg^{2+} ions does not affect electrical conductivity of LSCF3791 because only small amounts of them are introduced. The hopping of electrons is still limited by Co and Fe ion sites.

1.7 Benefit

To obtain perovskite discs with high electronic and oxygen permeation for using as cathode materials in SOFC.

CHAPTER II

EXPERIMENTAL

2.1 Chemicals

Chemicals and reagents for synthesis of perovskite materials were listed in Table 2.1. They were used without further purification.

Table 2.1 Chemicals and reagents for synthesis of perovskite materials

Chemicals and reagents	Formula weight	Purity (%)	Company
$La(NO_3)_3.6H_2O$	433.04	99.0	Himedia
$Sr(NO_3)_2$	211.63	-	Sigma-aldrich
$Co(NO_3)_2.6H_2O$	291.03	$\geq$ 98.0	Univar
$Fe(NO_3)_3.9H_2O$	404.00	$\geq$ 98.0	Fluka
$Ca(NO_3)_2.4H_2O$	236.15	99.0	Analytical
$Zn(NO_3)_2.6H_2O$	297.48	99	Fluka
$Mg(NO_3)_2.6H_2O$	256.41	99	Merck
$C_6H_{10}O_8$	210.14	$\geq$ 99.5	Merck
HNO_3	63.01	65	Merck
Liq. NH_3	35.05	25	Merck

2.2 Perovskite synthesis

All perovskite materials in Table 2.2 were synthesized in basic solution based on a modified citrate method. Stoichiometric quantities of metal nitrates as starting materials were mixed and dissolved in nitric acid. To the solution, citric acid solution with mole ratio of citric acid to metal ions of 2:1 was added as chelating agent. The solution was stirred at room temperature for 24 hrs and its pH was adjusted to 9 with ammonia solution. After that, the solution was dried and combusted at 200 ^{o}C on a hot plate, resulting grayish ash. The ash was then grinded using a mortar and calcined in air at 1,000 °C for 5 hrs with a heating rate of 6.5 °C/min to produce perovskite phase structure.

Table 2.2 The components of all samples

Dopant	**Components**	**Abbreviation**
-	$La_{0.3}Sr_{0.7}Co_{0.9}Fe_{0.1}O_3$	LSCF
Ca (Subtiutution Sr with Ca)	$La_{0.3}Sr_{0.6}Ca_{0.1}Co_{0.9}Fe_{0.1}O_3$	$L(SCa_{0.1})CF$
	$La_{0.3}Sr_{0.5}Ca_{0.2}Co_{0.9}Fe_{0.1}O_3$	$L(SCa_{0.2})CF$
	$La_{0.3}Sr_{0.4}Ca_{0.3}Co_{0.9}Fe_{0.1}O_3$	$L(SCa_{0.3})CF$
	$La_{0.3}Sr_{0.3}Ca_{0.4}Co_{0.9}Fe_{0.1}O_3$	$L(SCa_{0.4})CF$
	$La_{0.3}Sr_{0.2}Ca_{0.5}Co_{0.9}Fe_{0.1}O_3$	$L(SCa_{0.5})CF$
	$La_{0.3}Sr_{0.1}Ca_{0.6}Co_{0.9}Fe_{0.1}O_3$	$L(SCa_{0.6})CF$
	$La_{0.3}Ca_{0.7}Co_{0.9}Fe_{0.1}O_3$	LCCF
Ca (Subtiutution Sr and La with Ca)	$(La_{0.3}Sr_{0.7})_{0.9}Ca_{0.1}Co_{0.9}Fe_{0.1}O_3$	$(LS)Ca_{0.1}CF$
	$(La_{0.3}Sr_{0.7})_{0.8}Ca_{0.2}Co_{0.9}Fe_{0.1}O_3$	$(LS)Ca_{0.2}CF$
	$(La_{0.3}Sr_{0.7})_{0.7}Ca_{0.3}Co_{0.9}Fe_{0.1}O_3$	$(LS)Ca_{0.3}CF$
	$(La_{0.3}Sr_{0.7})_{0.6}Ca_{0.4}Co_{0.9}Fe_{0.1}O_3$	$(LS)Ca_{0.4}CF$
	$(La_{0.3}Sr_{0.7})_{0.5}Ca_{0.5}Co_{0.9}Fe_{0.1}O_3$	$(LS)Ca_{0.5}CF$
Zn (Substitution Co with Zn in $L(SCa_{0.2})CF$)	$La_{0.3}Sr_{0.5}Ca_{0.2}Co_{0.89}Zn_{0.01}\ Fe_{0.1}O_3$	$LSC(CZn_{0.01})F$
	$La_{0.3}Sr_{0.5}Ca_{0.2}Co_{0.88}Zn_{0.02}\ Fe_{0.1}O_3$	$LSC(CZn_{0.02})F$
	$La_{0.3}Sr_{0.5}Ca_{0.2}Co_{0.87}Zn_{0.03}\ Fe_{0.1}O_3$	$LSC(CZn_{0.03})F$
	$La_{0.3}Sr_{0.5}Ca_{0.2}Co_{0.86}Zn_{0.04}\ Fe_{0.1}O_3$	$LSC(CZn_{0.04})F$
	$La_{0.3}Sr_{0.5}Ca_{0.2}Co_{0.85}Zn_{0.05}\ Fe_{0.1}O_3$	$LSC(CZn_{0.05})F$

Dopant	Components	Abbreviation
Zn (Substitution Co and Fe with Zn in L($SCa_{0.2}$)CF)	$La_{0.3}Sr_{0.5}Ca_{0.2}(Co_{0.9}Fe_{0.1})_{0.89}Zn_{0.01}O_3$	LSC(CF)$Zn_{0.01}$
	$La_{0.3}Sr_{0.5}Ca_{0.2}(Co_{0.9}Fe_{0.1})_{0.88}Zn_{0.02}O_3$	LSC(CF)$Zn_{0.02}$
	$La_{0.3}Sr_{0.5}Ca_{0.2}(Co_{0.9}Fe_{0.1})_{0.87}Zn_{0.03}O_3$	LSC(CF)$Zn_{0.03}$
	$La_{0.3}Sr_{0.5}Ca_{0.2}(Co_{0.9}Fe_{0.1})_{0.86}Zn_{0.04}O_3$	LSC(CF)$Zn_{0.04}$
	$La_{0.3}Sr_{0.5}Ca_{0.2}(Co_{0.9}Fe_{0.1})_{0.85}Zn_{0.05}O_3$	LSC(CF)$Zn_{0.05}$
Mg (Substitution Co with Mg in L($SCa_{0.2}$)CF)	$La_{0.3}Sr_{0.5}Ca_{0.2}Co_{0.89}Mg_{0.01}\ Fe_{0.1}O_3$	LSC($CMg_{0.01}$)F
	$La_{0.3}Sr_{0.5}Ca_{0.2}Co_{0.88}Mg_{0.02}\ Fe_{0.1}O_3$	LSC($CMg_{0.02}$)F
	$La_{0.3}Sr_{0.5}Ca_{0.2}Co_{0.87}Mg_{0.03}\ Fe_{0.1}O_3$	LSC($CMg_{0.03}$)F
	$La_{0.3}Sr_{0.5}Ca_{0.2}Co_{0.86}Mg_{0.04}\ Fe_{0.1}O_3$	LSC($CMg_{0.04}$)F
	$La_{0.3}Sr_{0.5}Ca_{0.2}Co_{0.85}Mg_{0.05}\ Fe_{0.1}O_3$	LSC($CMg_{0.05}$)F
Mg (Substitution Co and Fe with Zn in L($SCa_{0.2}$)CF)	$La_{0.3}Sr_{0.5}Ca_{0.2}(Co_{0.9}Fe_{0.1})_{0.89}Mg_{0.01}O_3$	LSC(CF)$Mg_{0.01}$
	$La_{0.3}Sr_{0.5}Ca_{0.2}(Co_{0.9}Fe_{0.1})_{0.88}Mg_{0.02}O_3$	LSC(CF)$Mg_{0.02}$
	$La_{0.3}Sr_{0.5}Ca_{0.2}(Co_{0.9}Fe_{0.1})_{0.87}Mg_{0.03}O_3$	LSC(CF)$Mg_{0.03}$
	$La_{0.3}Sr_{0.5}Ca_{0.2}(Co_{0.9}Fe_{0.1})_{0.86}Mg_{0.04}O_3$	LSC(CF)$Mg_{0.04}$
	$La_{0.3}Sr_{0.5}Ca_{0.2}(Co_{0.9}Fe_{0.1})_{0.85}Mg_{0.05}O_3$	LSC(CF)$Mg_{0.05}$

2.3 Sample disc preparation

After calcination, the obtained single phase perovskites were re-grinded with ethanol using a pestle. A 1.8 g of powdered sample was loaded into a die cavity with 2 cm in diameter, and slowly pressed to 2 Tons for 10 min to obtain a disc. Then, the disc was sintered at 1,200^{o}C in air with a heating rate of 1 ^{o}C/min for 6 hrs to obtain the dense perovskite disc.

2.4 Characterization

2.4.1 X-ray diffractometry (XRD)

The structure and phase formation were identified by XRD using monochromatic Cu Kα radiation (40 kV, 30 mA). The XRD spectrum was carried out on a Rigaku Dmax-2200 Ultima$^+$ at Department of Chemistry, Faculty of Science, Chulalongkorn University. The data was recorded in the range of 20 – 70 degree with scan speed of 5 degree/min.

2.4.2 X-ray photoelectron spectroscopy (XPS)

The sintered powder was pressed into a pellet (3 mm in diameter and 1mm in thickness) and measured for surface property using X-ray photoelectron spectroscopy model Kratos AXIS HSi 165 and ULTRA instrument, at Institute for Molecular Science (IMS), Japan. The sample was irradiated with Al Kα radiation of 1486.6 eV and pass energy of 20 eV. The binding energy scale was calibrated using C1*s* spectrum with binding energy of 284.6 eV. The vacuum chamber was pressurized under 10^{-8} Torr.

2.4.3 Scanning Electron Microscopy (SEM)

Surface morphology of the sample discs was studied using a JEOL JSM- 5800LV scaning electron microscopy, Oxford Instrument (model Link ISIS series 300) at the Scientific and Technological Research Equipment Center (STREC), Chulalongkorn University.

2.4.4 X-ray absorption near edge spectroscopy (XANES)

The XANES measurements for La3*d* and O1*s*, Co2*p* were performed using the BL2A beamline with Beryl double-crystal monochromator, and the BL4B beamline of which monochromator was Varied-Line-Spacing Plane Grating (G1) of SiO_2 (VLS-PGM monochromator), respectively, at UVSOR synchrotron facility, Institute for Molecular Science (IMS), Japan. The energy scale of the spectra was recorded in the total-electron-yield (TEY) mode and calibrated using MgO. The pressure in the experimental chamber was lower than 10^{-8} Torr.

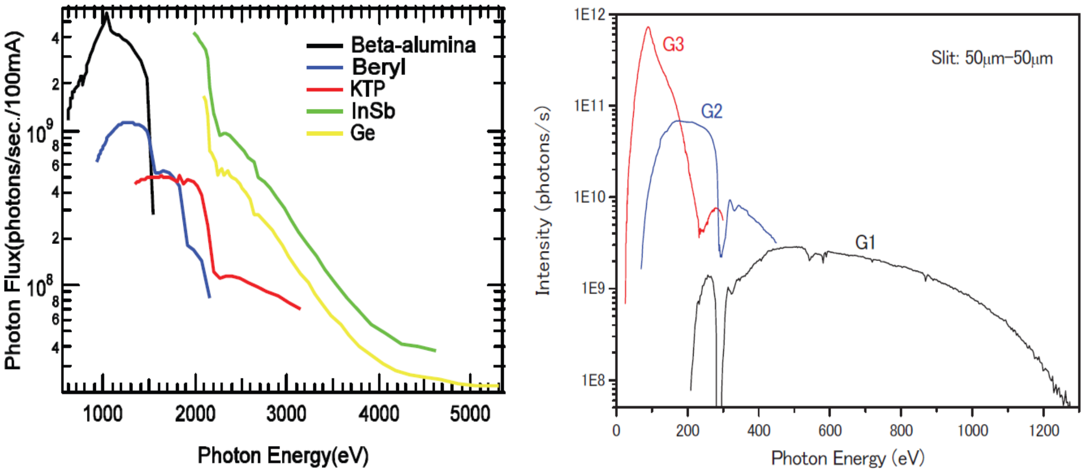

a) b)

Figure 2.1 Throughput spectra of a) the double crystal monochromator at BL1A beamline and b) the VLA-PGM monochromator on BL4B beamline.

Table 2.3 BL1A and BL4B beamline specifications

Beamline	**Monochromator**	**Resolution (E/ΔE)**	**Experiments**
BL1A	Double-crystal (2d value, energy range): Beryl (15.965 Å, 826-2271 eV)	1,500	Photoabsorption spectroscopy
BL4B	Varied-Line-Spacing Plane Grating (25 – 1000 eV)	> 5,000	Soft X-ray spectroscopy (mainly, photoelectron spectroscopy for gaseous and solid targets)

2.4.5 Electrical conductivity measurement

The electrical conductivity was measured in a tube furnace in air by a DC 4-probe method using Pt wire as electrodes. The sintered disc was cut into a rectangular shape (5 mm x 12 mm x 1.5 mm). Four Pt wire electrodes-two current contacts and two voltage contacts-were fabricated with the sample disc using Pt paste as a binder as shown in Figure 2.2. The specimen was fired at 950 ^{o}C for 10 min with a heating rate of

5 ^{o}C/min, to produce a firm contact between the electrodes and the sample disc. The different voltage (V) between the two voltage contact electrodes was recorded every temperature of 50 ^{o}C from 600 ^{o}C to 800 ^{o}C with a heating rate of 5 ^{o}C/min, after applying the current of 0.25 A. The electrical conductivity was then calculated using Equation 2.1.

$$\sigma = (I*L)/(V*W*T) \qquad (2.1)$$

Where σ is electrical conductivity

I is applied current

L is length between two voltage contact electrodes

V is different potential between two voltage contact electrodes

W is width of rectangular specimen

T is thickness of rectangular specimen

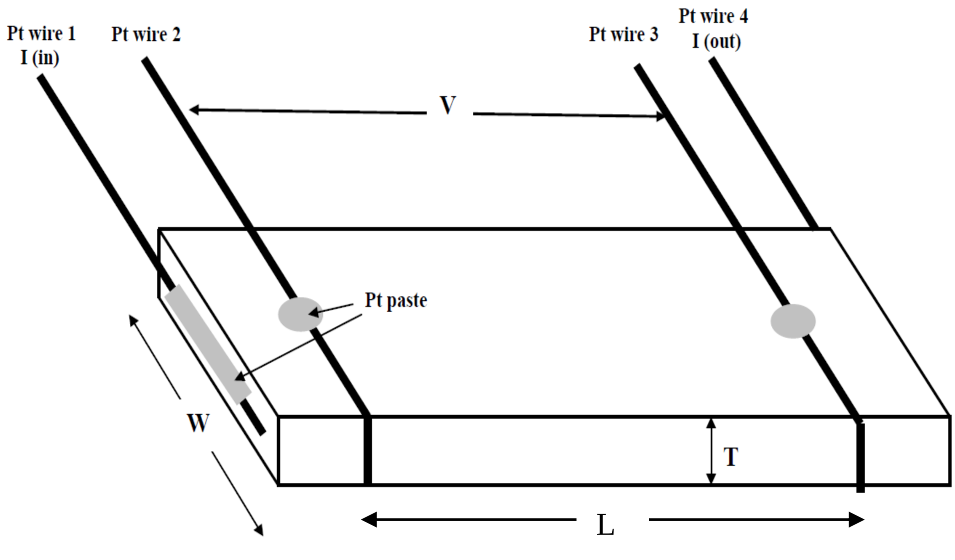

Figure 2.2 A rectangular specimen with four Pt wire electrodes (Pt wire 1, 4 were current contact electrodes and Pt wire 2, 3 were voltage contact electrodes)

2.4.6 Oxygen permeation measurement

Oxygen permeation measurement from air to He was carried out on a gas reactor (Figure 2.3). The sample discs were polished into 0.7 mm in thickness and placed between the alumina tubes which connect to gases. Dry air and He gases were purged into the alumina tubes at a flow rate of 50 ml/min on the top and the bottom of the sample disc, respectively. The oxygen gas permeated through the sample disc was collected by a gas tight syringe and analyzed by a gas chromatography (VARIAN, CP-3800) equipped with Moleculare sieve 13X column.

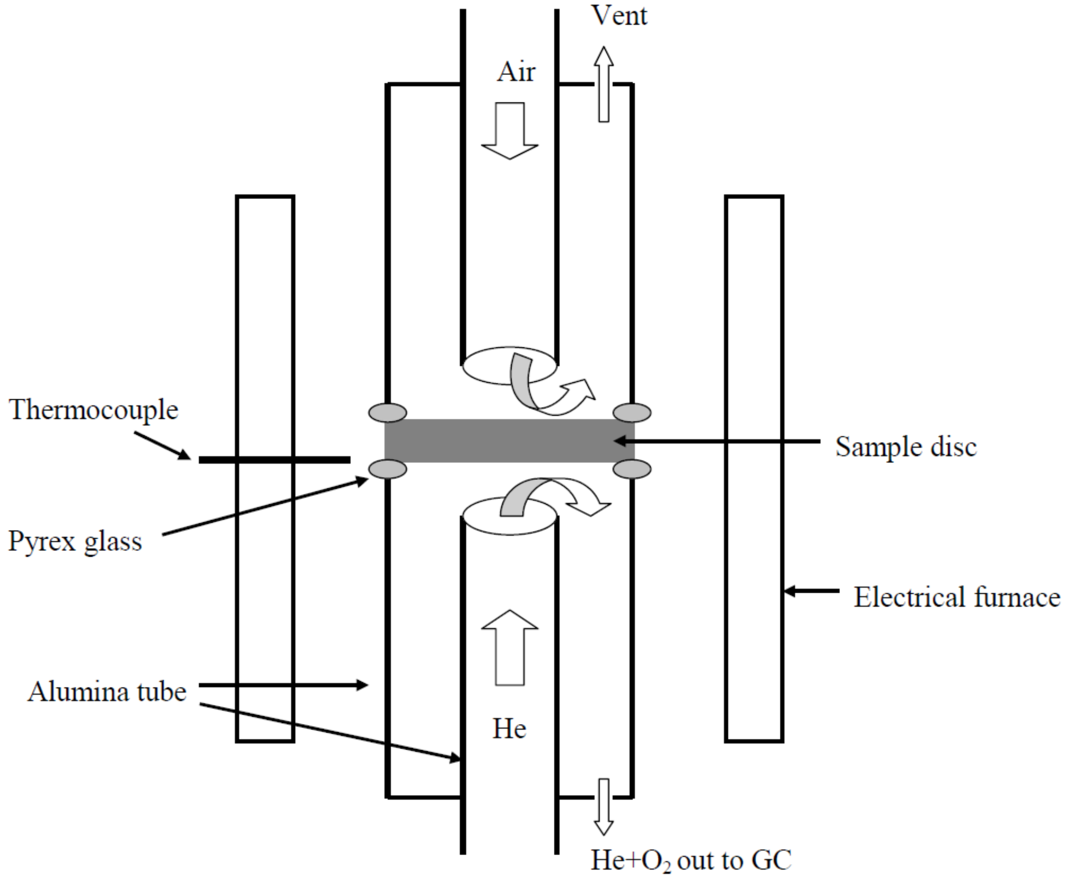

Figure 2.3 A Gas reactor for oxygen permeation measurement.

CHAPTER III

RESULTS AND DISCUSSION

3.1 Synthesis and properties of $La_{0.3}Sr_{0.7}Co_{0.9}Fe_{0.1}O_3$ (LSCF)

LSCFs were synthesized and calcined at 1000 ^{o}C. The effect of sintering temperature from 1100 - 1300 ^{o}C on LSCF discs was studied. Phase structure, surface morphology, surface chemistry and bulk property of all LSCFs were investigated by XRD, SEM, XPS and XAS, respectively. The conducting properties were also investigated for electrical conductivity and oxygen permeation. LSCF with more idealized cubic and highest oxygen permeation rate was chosen for doping of Ca ions in the structure in order to improve the electrical conductivity.

3.1.1 XRD analyses

The XRD patterns of LSCF discs sintered at different temperatures, Figure 3.1, indicate pure ABO_3-perovskite structure in primitive cubic form. With increasing the sintering temperature from 1,100 to 1,200 ^{o}C, the diffraction peak of (110) plane shifts towards lower angle suggesting the increase in lattice parameters, which can be explained by thermal reduction of smaller $Co^{3+,4+}$ cations to larger Co^{2+} cation (ionic radii (r) of Co^{2+} = 0.745 Å, Co^{3+} = 0.61 Å and Co^{4+} = 0.53 Å) [36-37]. The lattice parameters of the samples were calculated and summarized in Table 3.1.

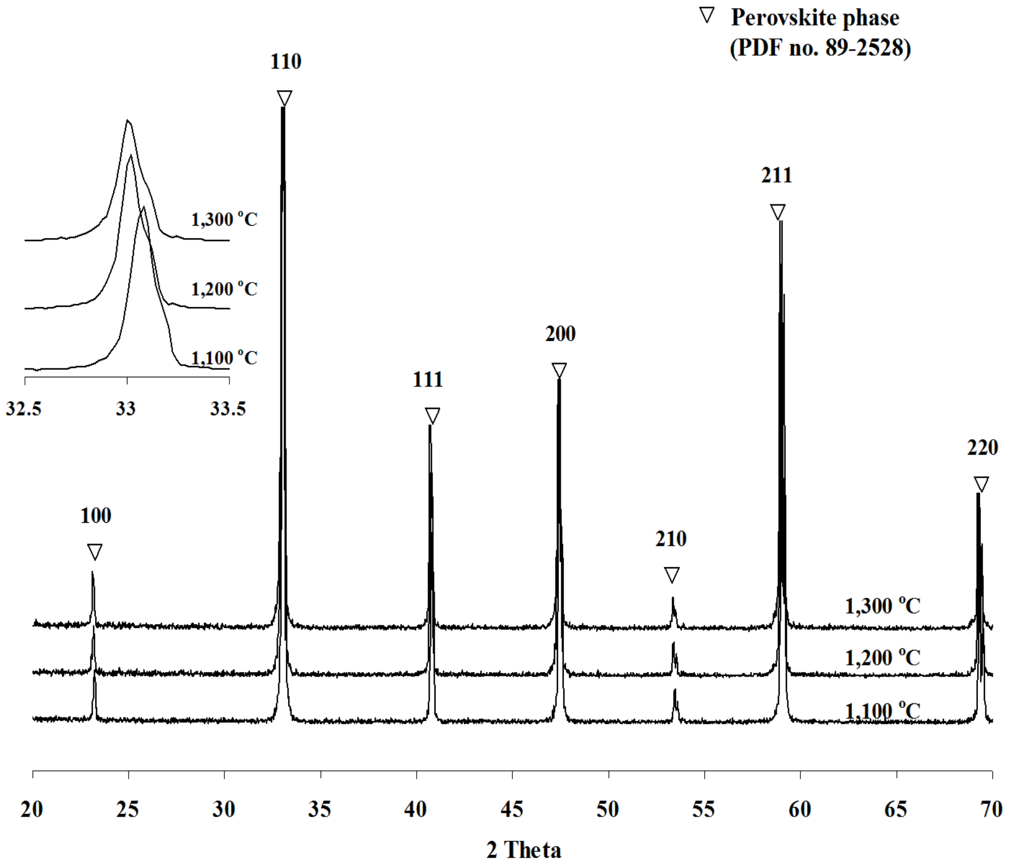

Figure 3.1 XRD patterns of LSCF discs sintered at various temperatures.

Table 3.1 Lattice parameters of LSCFs sintered at different temperatures.

Samples	* Lattice Parameter (Å)
LSCF sintered at 1,100 °C	3.828(9)
LSCF sintered at 1,200 °C	3.834(0)
LSCF sintered at 1,300 °C	3.834(5)

*The average lattice parameter is calculated from the diffraction peaks of (110), (111), (200) and (211) planes.

3.1.2 SEM analyses

SEM images of LSCF discs in Figure 3.2 illustrate the agglomeration of grains and the reduction of porosity when the sintering temperature is increased. The growth of grains may be due to the releasing of lattice oxygen activated by high sintering temperature [28,38].

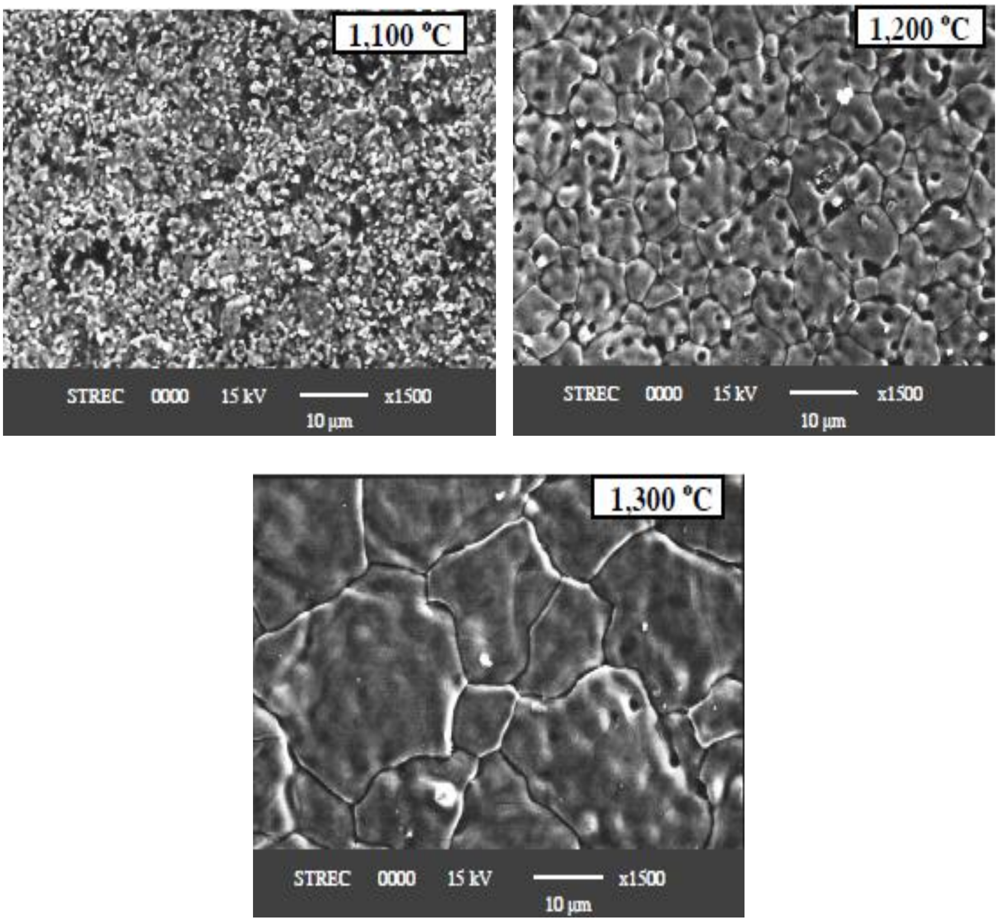

Figure 3.2. SEM images of LSCFs sintered at different temperatures.

3.1.3 Electrical conductivity analyses

The electrical conductivity of LSCFs is shown in Figure 3.3. From the results, LSCF sintered at 1,100 ^{o}C shows a great electrical conductivity at low temperatures but it decreases continuously with increasing temperature, indicating a metallic-like behavior ($\partial\sigma/\partial T < 0$) of the material. For LSCFs sintered at higher temperatures, the electrical conductivity is lower than the one sintered at 1100 ^{o}C but it increases with temperature and reaches the maximum value at 550 ^{o}C, and becomes decreasing continuously. This suggests semiconducting-like behavior ($\partial\sigma/\partial T > 0$) of the materials at low temperature range of 250-550 ^{o}C and metallic-like behavior at high temperature range of 550-800 ^{o}C.

When the concentration of Fe cation is very low with respect to Co content, the electrical conductivities of these LSCFs will be controlled by the hopping of e_g^* electrons [10,39] and electronic configuration of Co cations. For example, the electronic configuration of Co^{3+} was responsible for the metallic-like behavior of lanthanum cobaltite based-materials [40-43]. Therefore, in this work, the high electrical conductivity and metallic-like behavior of LSCF sintered at 1100 ^{o}C may be caused by HS Co^{3+} and Co^{4+}. Since the e_g^* electron of HS Co^{3+} has low binding energy (E_b) as shown in Figure 3.4, it is easily activated to conduction band, leading to a lot of localized electrons/holes. Moreover, the movement of electrons/holes is also supported by Co^{4+} without thermally activated need because of small difference in conduction band energy (ΔE_c) between Co^{4+} and Co^{3+} cations [36,44]. These effects result in high electrical conductivity of the material at low temperatures. When the temperature goes up, high energetic electrons move no direction and the vibration of lattice sites reduce the ability of electron/hole movement leading to the decrease of conductivity. For the semiconducting-like behavior and low electrical conductivity of LSCFs sintered at high temperatures, it may be explained by the changing in electronic configuration of Co^{3+} from HS Co^{3+} to LS Co^{3+} state, and/or the reduction of high valence state $Co^{3+, 4+}$ to low valence state Co^{2+}. Because LS Co^{3+} ($t_{2g}^{*6}e_g^{*0}$) has only t_{2g}^* electrons which E_b is higher than that of e_g^* electrons in HS state, small amounts of electrons are introduced to the conduction band. Moreover, these electrons/holes will be trapped at Co^{2+} sites because the conduction band energy of Co^{2+} cations is much lower than those of Co^{3+} cations [45]. These effects lead to low electrical conductivity of the materials. When the temperature is increased, in spite of the lattice vibrates and the electron moves no direction, the electrical conductivity is increased. This is because the electron has high energy, which can move towards the Co^{2+} site without electronic trapping.

Table 3.2 shows the activation energy (E_a) for the hopping of electrons. The result reveals that LSCF sintered at 1100 ^{o}C has the lowest E_a followed by the one sintered at 1300 and 1200 ^{o}C, respectively. According to the report of Kostogloudis et al. [36], the activation energy equals to the summation of E_b and ΔE_c. Therefore, the low E_a value of LSCF sintered at 1100 ^{o}C may be resulted from HS Co^{3+} and Co^{4+} which provides both low E_b and ΔE_c. The high E_a values of LSCFs sintered at 1300 and 1200 ^{o}C are caused by the high contents of LS Co^{3+} and/or Co^{2+}, which affects high E_b and ΔE_c as explained previously.

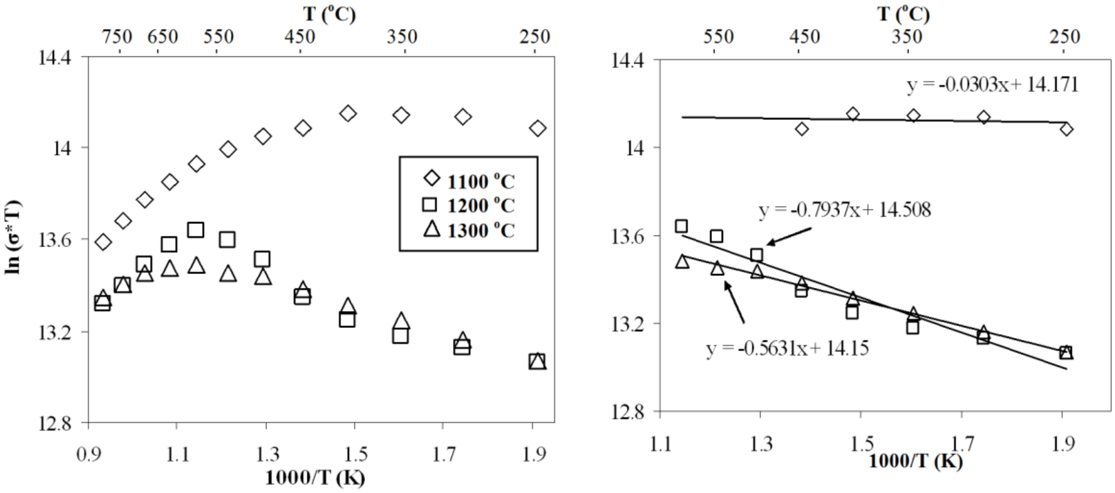

Figure 3.3 The temperature-dependent conductivity of LSCFs sintered at different temperatures.

Table 3.2 Activation energy (E_a) of LSCFs sintered at different temperatures.

Samples	E_a (kJ/mol)
LSCF sintered at 1,100 °C	0.2519 (250 – 450 °C)
LSCF sintered at 1,200 °C	6.5992 (250 – 600 °C)
LSCF sintered at 1,300 °C	4.6819 (250 – 600 °C)

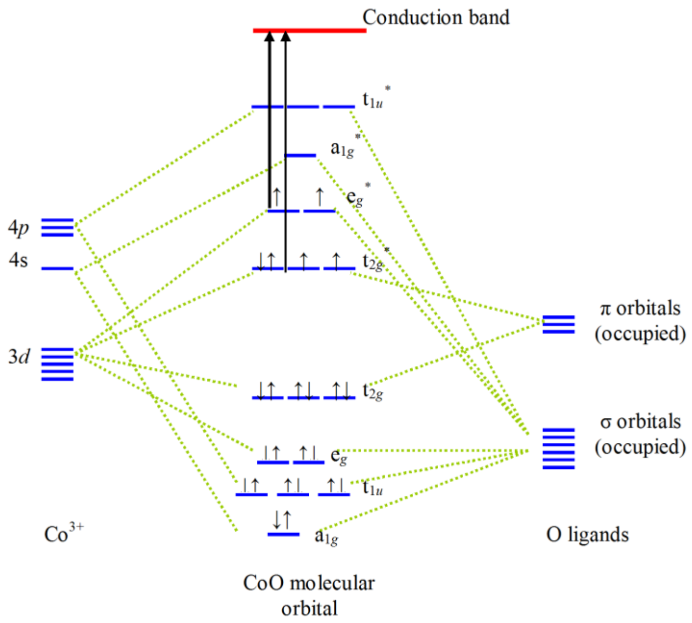

Figure 3.4. Electronic transition to the conduction band of HS Co^{3+} sites [46-47]

3.1.4 Oxygen permeation analyses

According to the semiconducting behavior, LSCFs sintered at 1,200 and 1,300 °C are chosen for oxygen permeation analysis and the data are shown in Figure 3.5. It has been found that LSCF sintered at 1200 °C shows higher oxygen permeation rate than the other one. The high oxygen permeation rate of LSCF comes from the ability of oxygen reduction reaction (ORR) ability to produce surface oxide ions and the bulk diffusion of these ions, that is resulted from the large numbers of oxygen vacancies and active Co^{2+} cations. Since Co^{2+} cations have larger ionic size and lower oxidation number comparing to $Co^{3+,4+}$, the Co^{2+}-O bond is weaker than that of the other. Thus, the expansion of saddle point is proposed for the great bulk diffusion of oxide ions. Moreover, an idealized cubic structure which provides stress-free lattice is also proposed to be another reason to promote oxygen permeation in this sample.

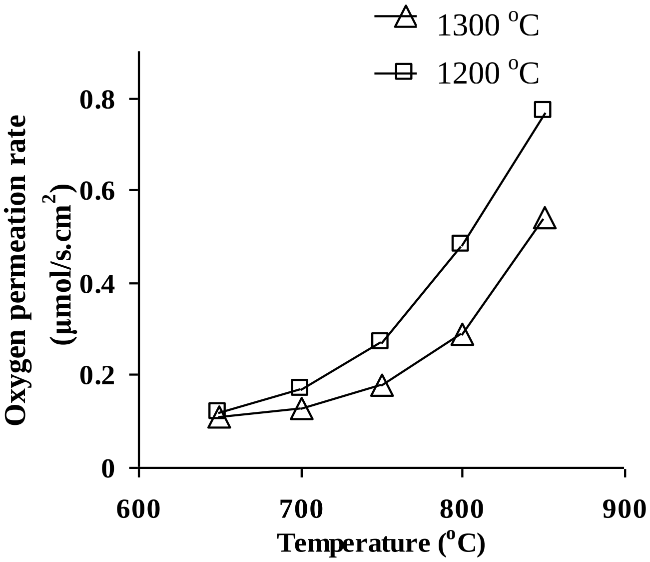

Figure 3.5 Oxygen permeation rate of LSCFs sintered at different temperatures

3.1.5 XPS analyses

The C1*s* spectra (Figure 3.6) illustrate three main peaks appearing at ca. 284, 286 and 288 eV. The low BE peak at ~284 eV relates to adventitious carbon and the remaining peaks relate to $La_2(CO_3)_3$ and surface carbonates e.g. CO_3^{2-}, respectively [48]. The highest contents of $La_2(CO_3)_3$ and carbonates are observed on LSCF sintered at 1100 °C and the value becomes decreasing after increasing the sintering temperature.

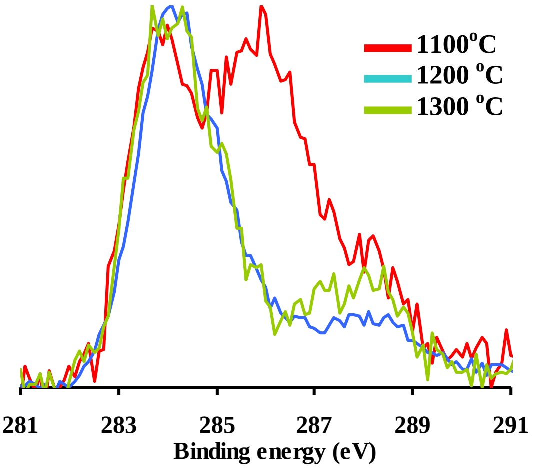

Figure 3.6 The C1*s* core level XPS spectra of LSCFs at different sintering temperatures.

The XPS spectra of Sr are shown in Figure 3.7. The main peaks at 131 and 133 eV can be assigned to 3$d_{5/2}$ sub band of Sr^{2+} surrounded by oxygen vacancies in SrO_{1-x} suboxide and of the regular Sr in perovskite lattice (SrO), respectively [49]. From the results, it is clear that oxygen vacancies of LSCFs sintered at 1200 and 1300 °C are higher than those of the one sintered at 1100 °C.

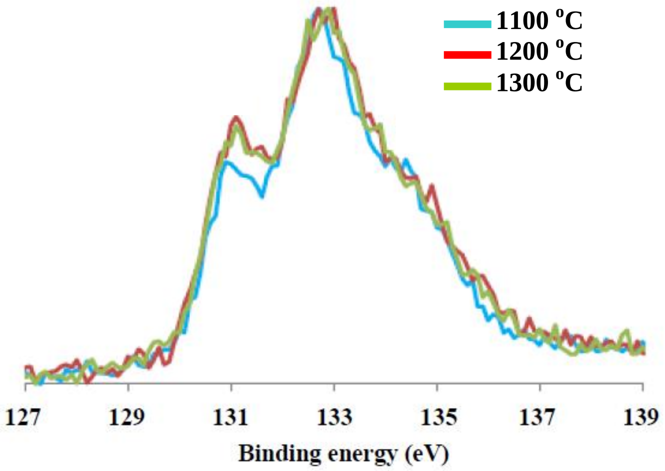

Figure 3.7 Normalized Sr3*d* core level XPS spectra of LSCFs at different sintering temperatures.

The deconvoluting of O1*s* peaks, which are represented by letter A-E, is shown in Figure 3.8. Peaks A and B (ca. 527 and 528 eV) are attributed to lattice O^{2-} coordinated with La, Sr at A-site and Co, Fe at B-site, respectively [50-52]. The different BE of oxide ions at A and B-sites (~1eV) corresponds to the La_2O_3 and Co_2O_3, Fe_2O_3 standards reported by Barr [53]. The high BE peak (530 eV) is contributed to –OH species, which locate at higher BE (2-2.5 eV) than those of lattice O^{2-} [50]. Peak D (531.5 eV) is assigned to CO_3^{2-} species confirmed by the appearance of CO_3^{2-} species in C1*s* spectra. And the last broadening peak locating at ca 533 eV is assigned to adsorbed O_2^{2-} and O_2^{-} species [54-55]. From the spectra, LSCF sintered at 1100 °C exhibits the highest quantities of –OH species. For LSCFs sintered at 1,200 °C, the intensity of peak B is lower than those of peak A, suggesting low amount of lattice O^{2-} at B site. This indicates the oxygen vacancies in this sample prefer to coordinate with cations at the B site more than the A site. Besides, it is well known that the formations of Co^{2+} and oxygen vacancies are the cooperative reaction as shown in reaction 3.1 and 3.2 [56]. Thus, it is reasonable to conclude that LSCF sintered at 1,200 °C shows the highest amount of oxygen vacancies and Co^{2+}, followed by the one sintered at 1,300 and 1,100 °C, respectively.

$$Co^{3+}O^{2-}Co^{3+} \longrightarrow Co^{3+}O^{-}Co^{2+} \quad \cdots\cdots\cdots \quad (3.1)$$

$$Co^{3+}O^{-}Co^{2+} \longrightarrow Co^{2+}V_oCo^{2+} + 1/2O_2(g) \quad \cdots\cdots\cdots \quad (3.2)$$

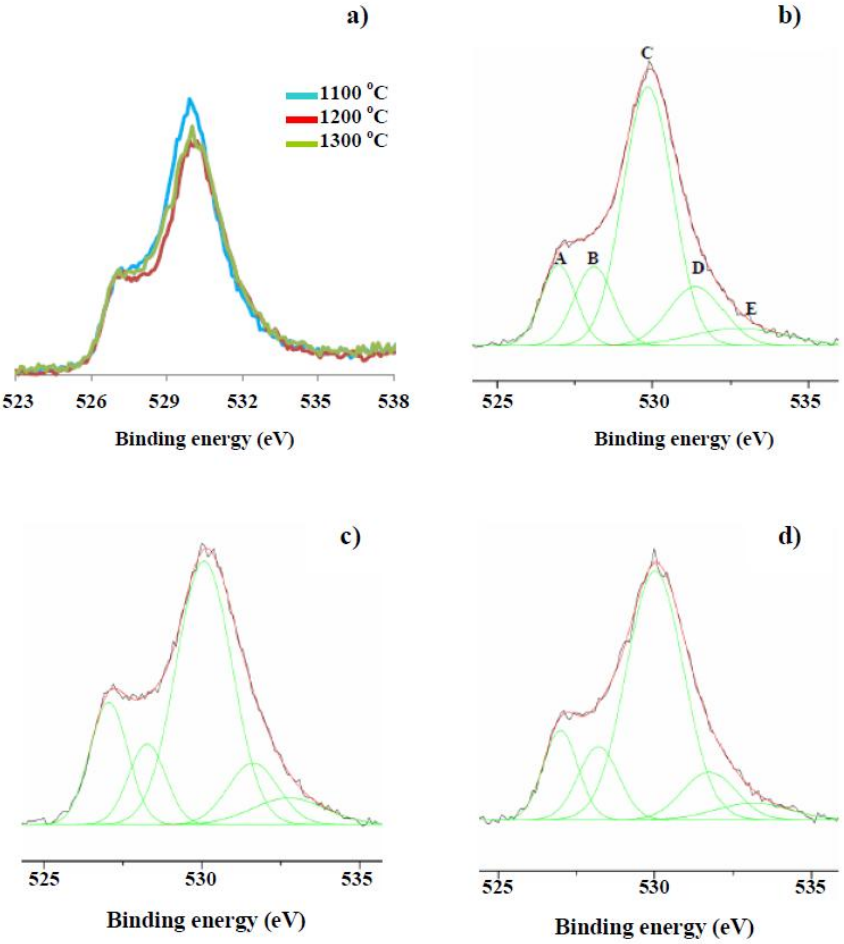

Figure 3.8 O1*s* core level XPS spectra of LSCFs at different sintering temperatures a) Normalized spectra b) Deconvoluting of O1*s* peak of perovskite sintered at 1100 °C c) Deconvoluting of O1*s* peak of perovskite sintered at 1200 °C d) Deconvoluting of O1*s* peak of perovskite sintered at 1300 °C

The La3$d_{5/2}$ XPS spectra of La_2O_3 are shown in Figure 3.9. The doublet peak of La3$d_{5/2}$ sub band indicates inequivalent La^{3+} ions in the structure due to the difference in final excited state. The lower binding energy peak (~833.5 eV) corresponds to $3d^0f^0$ final state and the higher energy one (~837 eV) corresponds to $3d^0f^n\underline{L}$ final state (where n > 0 and $\underline{L}$ = ligand hole), which resulted from the charge transfer from O2*p* to La4*f* orbitals [48,50,57]. LSCFs sintered at 1300 and 1100 °C show the intense peak of $3d^0f^n\underline{L}$ final state. This indicates strong charge transfer from O2*p* to La4*f* orbitals which may result from the short distance between La and O, and the structural distortion (Figure 3.10b) as reported by Houeso [23]. On the contrary, the weak intensity of $3d^0f^n\underline{L}$ final state observed on LSCF sintered at 1200 °C indicates weak charge transfer from O2*p* to La4*f* orbitals, suggesting a weak structural distortion in the sample as shown in Figure 3.10a.

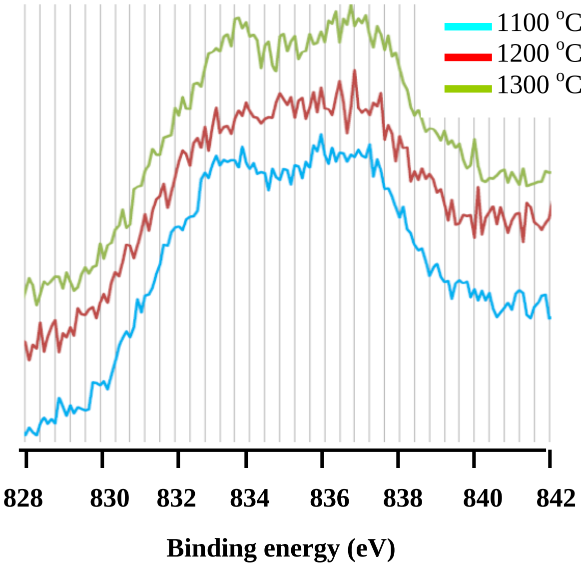

Figure 3.9 The La3*d* core level XPS spectra of LSCFs sintered at different temperatures.

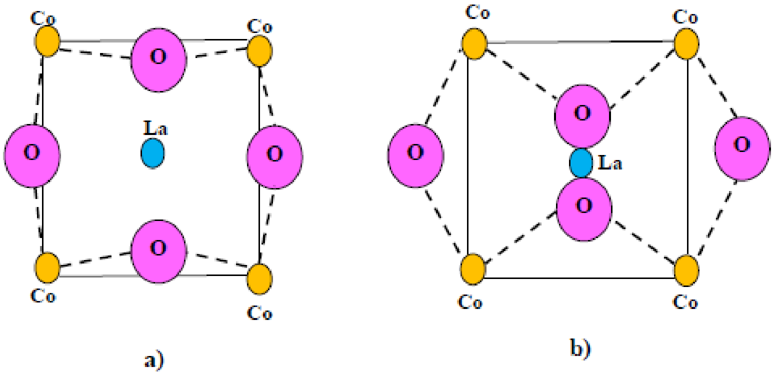

Figure 3.10. Proposed structure of LSCF with a) weak structural distortion b) strong structural distortion [23]

The Co2*p* spectra (Figure 3.11) split into Co2$p_{3/2}$ sub-band (~779 eV) and Co2$p_{1/2}$ sub-band (~794 eV) due to spin-orbit interaction. The Co2$p_{3/2}$ sub-band is resolved into 2 main components. The first component locating at ~779 eV is assigned to Co^{2+} and Co^{3+} ions which the different BE is ~0.6 eV [58-59]. The second component locating at ~1 eV upscale from Co^{2+} and Co^{3+} peaks associates with Co^{4+} [52]. According to a small difference in BE, it is difficult to discriminate the Co state by using the peak position alone. The better way to elucidate these state is to use the different BE (ΔE) between $Co_{3/2}$ sub-band and $Co_{1/2}$ sub-band, and the satellite shake up peak, which are sensitive to the changing in electronic state and electronic configuration of *d* electron of Co and also other first low transition metals. The ΔE value depends on the number of unpaired *d* electrons, which means that a lot of unpaired *d* electrons provide large ΔE [60]. Thus, the ΔE value of HS Co^{2+} in CoO is higher than those of LS Co^{3+} in Co_2O_3, which are close to 15.5-16 eV and 15 eV, respectively [58,60-62]. Moreover, the peak feature and the shake up satellite peak can also be used to predict the state of Co in materials. From the previous reports by several researchers [61,63-68], satellite peaks found on the high binding energy side (~5-10 eV) of *L*-shell photoelectron lines of 3*d* metal oxides arise from charge transfer and atomic shake up transition: $e_g \rightarrow e_g^*$, $t_{2g} \rightarrow t_{2g}^*$, and $e_g^* \rightarrow a_{1g}^*$ ($3d \rightarrow 4s$) transition, respectively (Figure 3.12). For HS Co^{2+} ($t_{2g}^{*5}e_g^{*2}$), all transitions are allowed leading to the strong and broadening shake up peak, which can overlap with the parent peaks resulting in the broadening Co2*p* main peaks. In the case of LS Co^{3+} ($t_{2g}^{*6}e_g^{*0}$), only $e_g \rightarrow e_g^*$ transition is occurred resulting in the weak and sharp sake up peak, as well as the narrow Co2*p* main peaks. However, not only electronic configuration, but the shake up transition also depends on ligand to metal charge transfer (LMCT). Strong LMCT supports $e_g \rightarrow e_g^*$ and $t_{2g} \rightarrow t_{2g}^*$ shake up transition affecting the intense and broadening shake up peak. On the other hand, weak LMCT results in weak shake up transition and shake up peak [68].

The ΔE value (15 eV) and the weak HS Co^{2+} shake up peak intensity of LSCFs sintered at 1100 ^oC indicates that Co in this sample exhibits mainly as LS Co^{3+}. For LSCFs sintered at 1200 ^oC, the ΔE value (15.3 eV) and strong shake up peak indicate HS Co^{2+} and strong LMCT. In case of LSCF sintered at 1300 ^oC, the weak intensity of HS Co^{2+} shake up peak is observed with ΔE value of 15.3 eV indicating the mixed HS Co^{2+} and LS Co^{3+}. This may be resulted from weak LMCT due to strong structural distortion.

From all XPS results, it has been concluded that LSCF sintered at 1200 ^oC has a lot of surface oxygen vacancies and Co^{2+} species, weak structural distortion, low surface CO_3^{2-} and –OH. These factors promote high surface ORR and oxygen permeation, which is in agreement with the result in section 3.1.4.

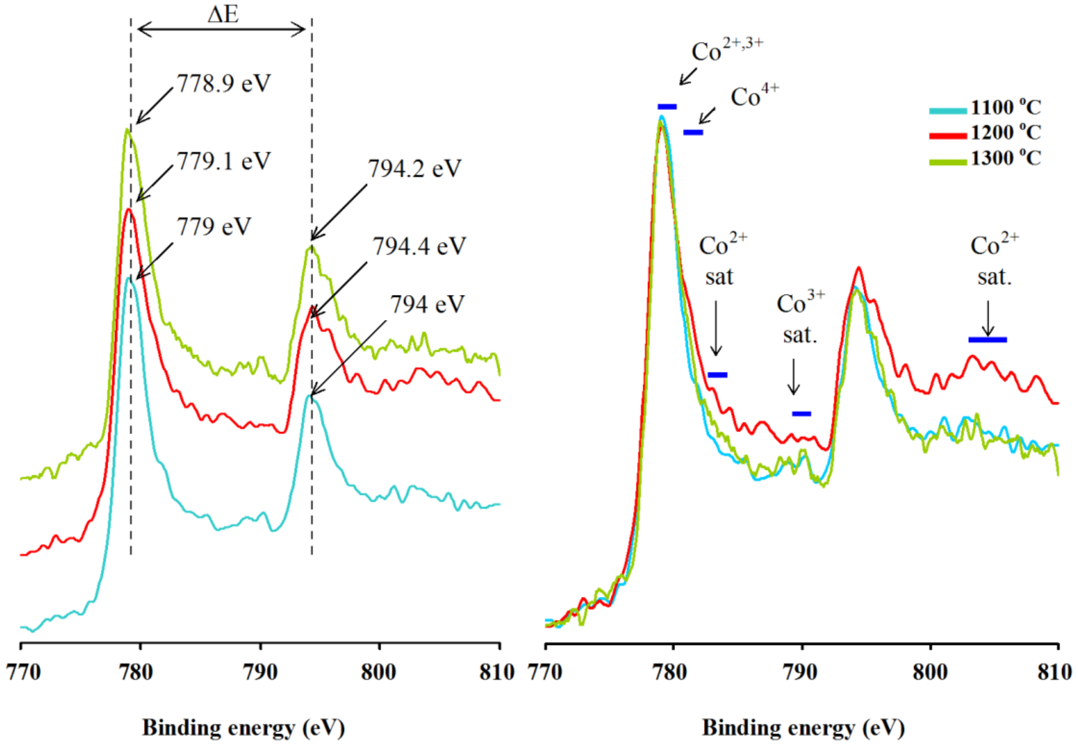

Figure 3.11. Normalized Co2*p* core level XPS spectra of LSCFs sintered at different temperatures.

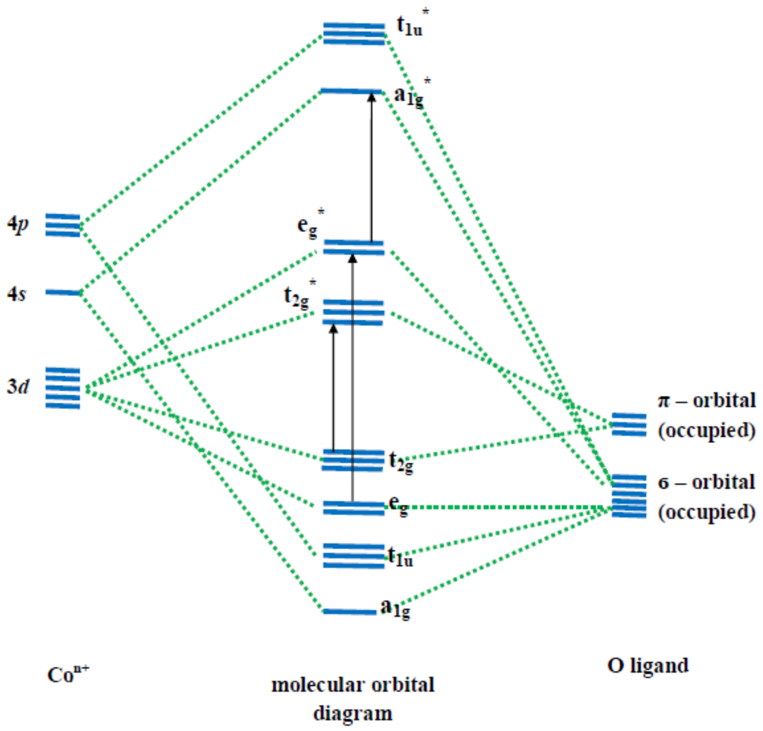

Figure 3.12. Charge transfer shake up process in metal oxide compounds

3.1.6 XAS analyses

The bulk properties of LSCF were investigated for oxygen deficiency, structural distortion, oxidation state and electronic configuration of Co ions by X-ray absorption near edge spectroscopy (XANES).

3.1.6.1 La M-edge X-ray absorption spectroscopy (La M-edge XAS)

Figure 3.17 shows the X-ray absorption spectra assigned to La3*d* → La4*f* transition. The lower and higher photon energy peaks indicate La$3d_{5/2}$ and La$3d_{3/2}$ sub band, respectively. The transition of La3*d* → La4*f* at 1100 °C and 1200 °C are higher than that of 1300 °C. The low absorption intensity of LSCF sintered at 1300 °C may be resulted from the strong distortion of structure, which allows the LMCT from O2*p* orbital to La4*f* orbital, as previous discussed in XPS part. That situation results in high density of electrons in La4*f* orbitals and prohibits the La3*d* → La4*f* transition.

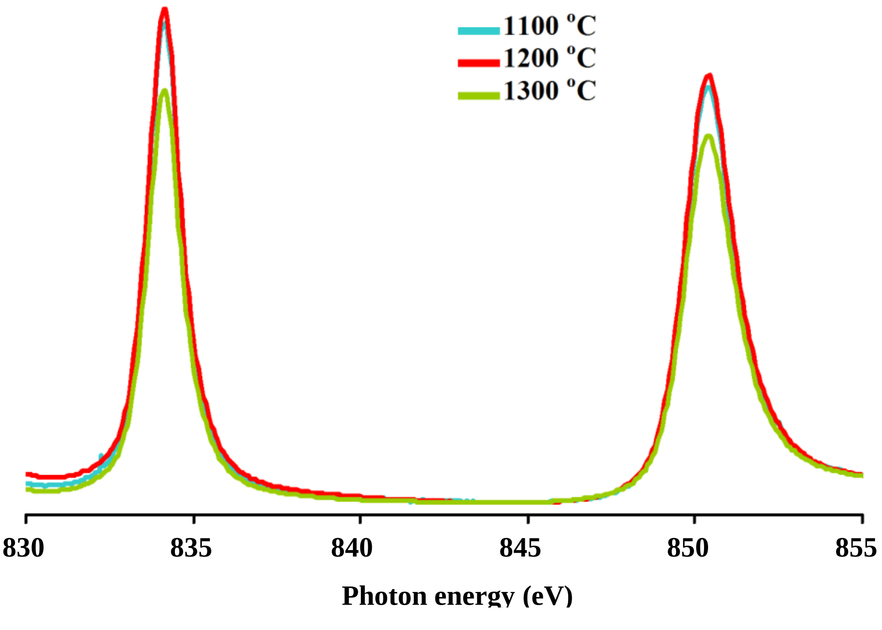

Figure 3.13. Normalized La L-edge region X-ray absorption spectra of LSCFs sintered at different temperatures

3.1.6.2 Co L-edge X-ray absorption spectroscopy (Co L-edge XAS)

Figure 3.14 shows the X-ray absorption spectra of LSCFs which indicates the transition from Co2*p* to t_{2g}^{*} and e_{g}^{*} orbitals. The spectra are spitted into two main peaks because of spin-orbit interaction, which are Co$2p_{3/2}$ (lower photon energy) and Co$2p_{1/2}$ (higher photon energy) sub band [46]. From the result, LSCF sintered at 1300 °C exhibits the highest peak intensity compared with others, suggesting less electron density in t_{2g}^* and e_g^* orbitals. This may be due to strong distortion in Co-O-Co bond which results in poor overlapping between the Co and O leading to weak LMCT from O to Co. Furthermore, the high quantity of Co^{4+} specie is another plausible reason because this specie has less electron in t_{2g}^* and e_g^* orbitals with respect to Co^{2+} and Co^{3+}. On the contrary, the lowest peak intensity of LSCF sintered at 1200 °C can be explained by weak distortion in Co-O-Co bond, and may be resulted from the high quantities of Co^{2+} specie which has high electron in t_{2g}^* and e_g^* orbitals [74].

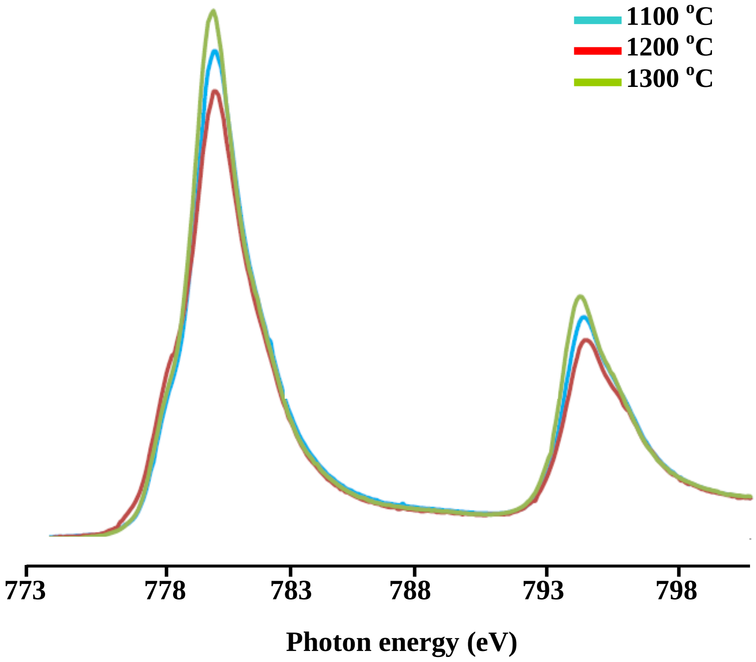

Figure 3.14. Normalized Co L-edge region X-ray absorption spectra of LSCFs sintered at different sintering temperatures

3.1.6.3 O K-edge X-ray absorption spectroscopy (O K-edge XAS)

The O K-edge spectra of LSCF, Figure 3.15, show important features, which corresponds to the electronic transition as follows: transition of electrons from O1*s* orbital of lattice O^{2-} to hybridized O2*p*-t_{2g}^* hole state (feature A), transition of electrons from O1*s* orbital of lattice O^{2-} hybridized O2*p*-e_g^* hole state (feature B and C, Figure 3.16), transition of electrons from σ_{1s} orbital to σ^* resonance of adsorbed O_2^- species (feature D, Figure 3.17), transition of electrons from O1*s* orbital of lattice O^{2-} O1*s* orbital of lattice O^{2-} to hybridized O2*p*-La5*d*/Sr4*d* hole state (feature E), transition of electrons from σ_{1s} orbital to Co4*sp* orbital hybridizing with O_2^- (feature F), and transition of electrons from σ_{1s} orbital to Co4*sp* hybridizing with monoxidic species (feature G) [69-70].

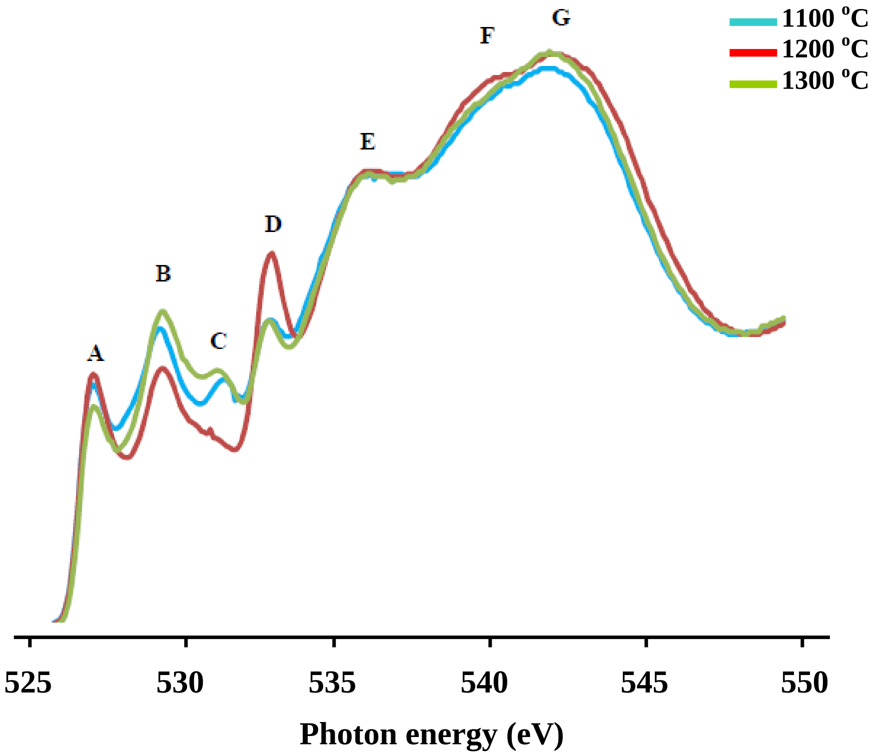

Figure 3.15. Normalized O K-edge region X-ray absorption spectra of LSCFs sintered at different temperatures

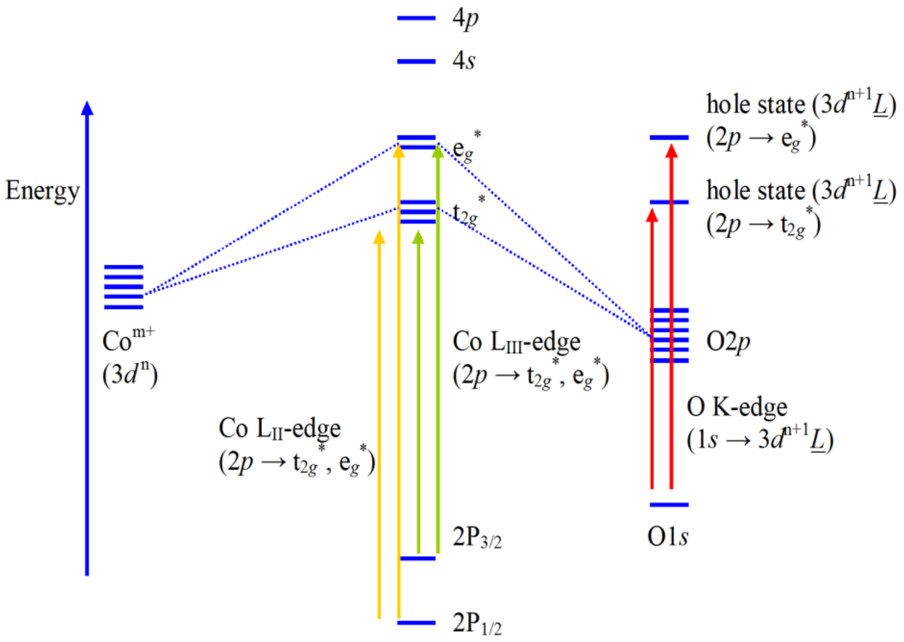

Figure 3.16. Electronic transition in the O K- edge and Co L-edge regions

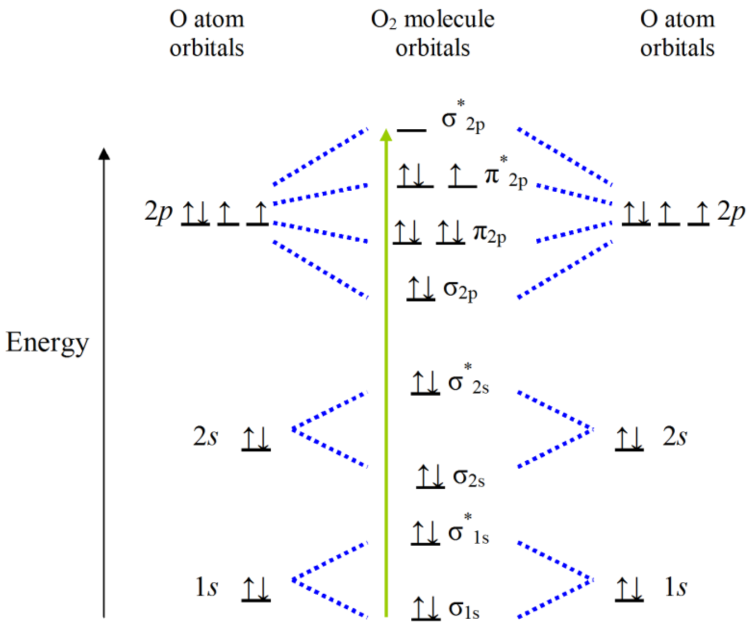

Figure 3.17. Electronic transition in O_2^- specie [71]

In feature A – C, these transitions deal with electrons in O1s orbital of lattice O^{2-} to the hybridized hole state between O2*p* and Co3*d* ($3d^{n+1}\underline{L} \longrightarrow \underline{c}3d^{n+1}$, where $\underline{L}$ and $\underline{c}$ denotes hybridized O2*p* hole state and O1*s* core hole, respectively). The peak intensity is sensitive to the quantity of $3d^{n+1}\underline{L}$ hole state.

The transition in feature B and C are in the following sequence: LSCF sintered at 1300 °C > 1100 °C > 1200 °C, which suggests the high quantity of O2p-e_g^* hole state in the series of LSCF sintered at 1300 °C > 1100 °C > 1200 °C. This result relates to the oxidation state and electronic configuration of Co ions. Co^{2+} has electron density in hybridized O2p-e_g^* orbital higher than Co^{3+} and Co^{4+}, therefore, the transition of electrons from O1s to hybridized O2p-e_g^* orbitals will be limited. Therefore, it can be concluded that the quantity of Co^{2+} is in the following sequence: LSCF sintered at 1200 °C > 1100 °C > 1300 °C.

Many researchers reported a mixed oxidation state of Co cations as HS Co^{2+}, LS Co^{3+}, HS Co^{3+} and IS Co^{4+} in lanthanum cobaltite based-perovskites [42,44,72-74]. And the transition of electrons from O1s to O2p-e_g^* hole state in feature C is the distinction of IS Co^{4+} ($t_{2g}^{*4}e_g^{*1}$), as shown in Figure 3.19 [69,74]. From feature C, it has been concluded that the content of IS Co^{4+} is in the following sequence: LSCF sintered at 1300 °C > 1100 °C > 1200 °C. Considering feature B, this feature represents electronic transition from O1s orbital to hybridized O2*p*-e_g^* hole state, which is strongly influenced by LS Co^{3+}. The intensity of this feature of LSCF sintered at 1300 ^oC is higher than LSCFs sintered 1100 and 1200 ^oC, respectively. This indicates the high quantity of LS Co^{3+} in the series of LSCF sintered at 1300 ^oC > 1100 ^oC > 1200 ^oC. On the contrary, feature A, which corresponds to electronic transition from O1*s* orbital to hybridized O2*p*-t_{2g}^* hole state, is strongly influenced by HS Co^{3+}. It is clear that LSCF sintered at 1200 ^oC shows the highest intensity of this feature followed by the ones sintered at 1100 and 1300 ^oC, respectively. This suggests the order of HS Co^{3+} content as follow: LSCF sintered at 1200 ^oC > 1100 ^oC > 1300 ^oC.

These results clarify the assumption in electrical conductivity part that LSCF sintered at 1100 ^oC shows high electrical conductivity and low E_a value because of HS Co^{3+} and IS Co^{4+}. For the ones sintered at 1200 and 1300 ^oC, the decrease of electrical conductivity and the increase in E_a value are due to HS Co^{2+} and LS Co^{3+}, respectively.

Feature D is assigned to the transition of σ_{1s} electron to σ^* antibonding of adsorbed O_2^- specie. The absorption intensity of LSCFs indicates the amounts of O_2^- species on the surface of materials. According to the reports of Imamura and other researchers [51,75-77], O_2 molecule is adsorbed and reduced to O_2^- at the oxygen vacancies at B site along grain boundaries. Therefore, it can be concluded that the high quantity of O_2^- species of LSCF sintered at 1200 ^oC is due to a lot of oxygen vacancies at Co site along grain boundaries. And the low amounts of O_2^- species observed on LSCFs sintered at 1100 and 1300 ^oC is due to low quantities of oxygen vacancies at Co site along grain boundaries. These results are consistent with XPS analysis of O1*s* core in previous section.

Feature E corresponds to the electronic transition from O1*s* orbital to hybridized O2*p*-Sr4*d*/La5*d* hole state. The equal absorption intensity of this feature indicates the same quantity of available hole state which may be resulted from several factors e.g., structural distortion and the amount of O around La/Sr cations.

Considering the remaining features, their intensity is almost equally for all LSCFs. This may be because these features correspond to the electronic transition from core electrons to Co4*sp* state which locates nearly continuum state. These states have small energetic difference resulting in undistinguishable and broadening peaks. Thus, it is difficult to use them for defect characterization in the materials.

From all XAS results, LSCF sintered at 1200 °C exhibits the highest oxygen vacancy and Co^{2+} contents, and weak structural distortion which means more idealized cubic. These factors lead to great bulk oxygen diffusion as explained previously in oxygen permeation part. According to such properties, it has been chosen for further study.

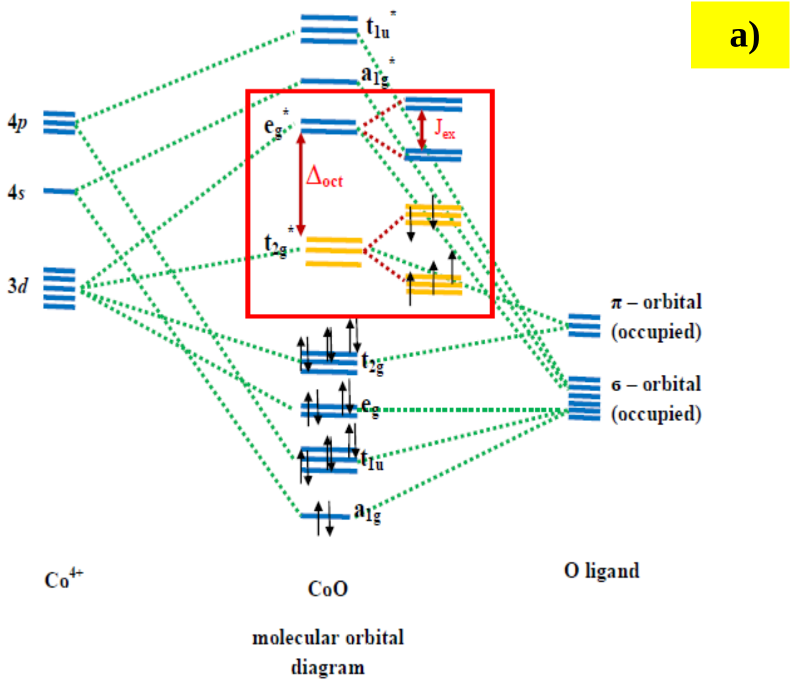

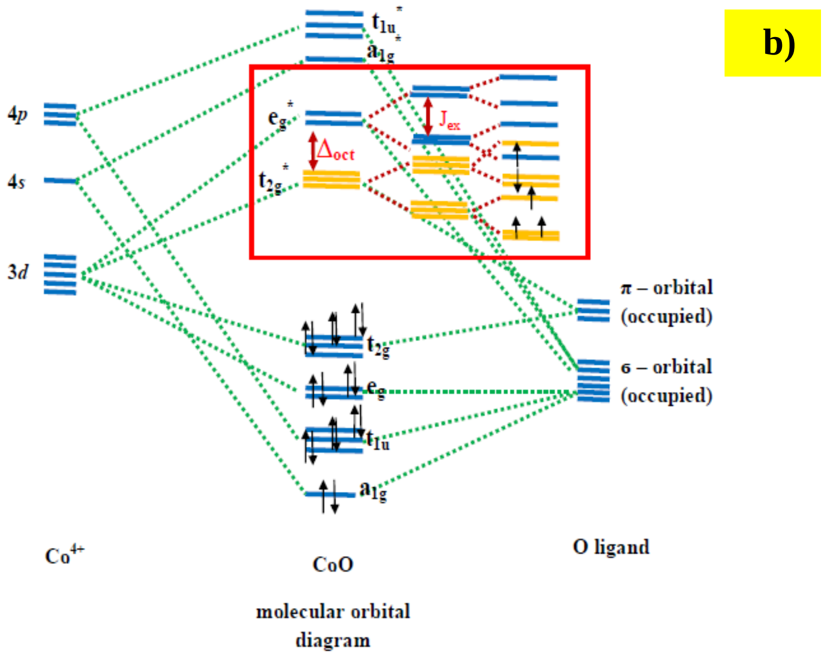

Figure 3.18. Simplified molecular orbital diagram of Co^{4+} ions in octahedral environment a) low spin configuration ($t_{2g}^{*5}e_g^{*0}$) (weak covalency bond and LMCT) b) intermediate spin configuration with Jahn-Teller distortion ($t_{2g}^{*4}e_g^{*1}$) (strong covalency bond and LMCT stabilize t_{2g} and destabilize t_{2g}^* leading to small Δ_{oct} and IS)

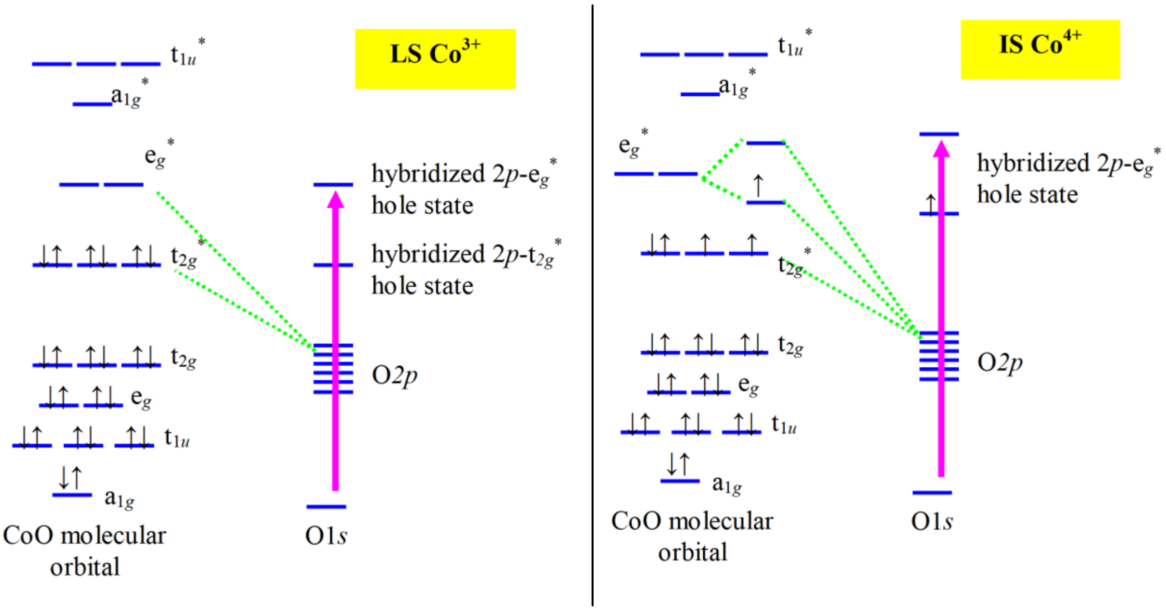

Figure 3.19. O K-edge transitions of LS Co^{3+} (Feature B) and IS Co^{4+} (Feature C)

3.2 Synthesis and properties of $La_{0.3}Sr_{0.7-x}Ca_xCo_{0.9}Fe_{0.1}O_3$ (X = 0 – 0.7)

3.2.1. XRD analyses

The XRD patterns of $La_{0.3}Sr_{0.7-x}Ca_xCo_{0.9}Fe_{0.1}O_3$ (X = 0 – 0.7), Figure 3.20, show that the structures of all compounds are primitive cubic of perovskite phase. CaO and CoO are impurity phases when X=0.6-0.7. The peak intensity decreases with increasing the Ca content, which indicates low crystallinity of the materials due to structural distortion. The lattice parameter is calculated and summarized in Table 3.3. Since Ca (r = 1.34 Å) has smaller size than Sr (r = 1.44 Å), the lattice parameter should theoretically decrease with increasing the Ca content. On the contrary, the lattice parameter of X = 0.1 is slightly higher than that of LSCF. When X = 0.2, the lattice parameter decreases drastically. This may be influenced by the oxidation state of Co ions [36]. Co^{2+} has ionic size larger than Co^{4+}, therefore the material with X = 0.1 should have higher quantity of Co^{2+} ions more than others.

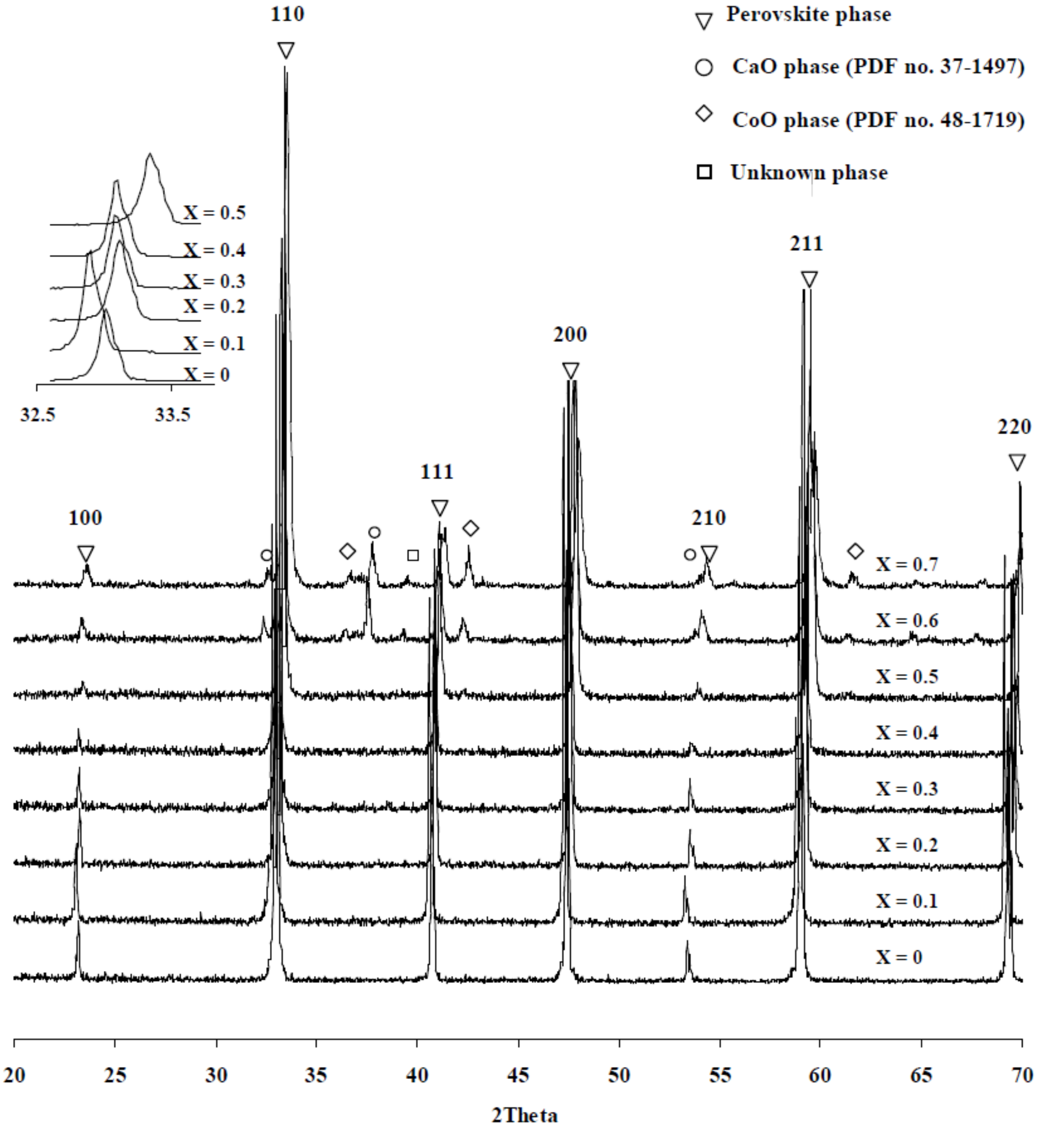

Figure 3.20. XRD patterns of $La_{0.3}Sr_{0.7-x}Ca_xCo_{0.9}Fe_{0.1}O_3$ (X = 0 – 0.7) sintered at 1,200 ^{o}C for 6 hrs

Table 3.3. Lattice parameters of $La_{0.3}Sr_{0.7-x}Ca_xCo_{0.9}Fe_{0.1}O_3$ (X = 0 – 0.5) perovskites sintered at 1200 °C for 6 hrs

Ca content	***Unit cell parameter (Å)**
X = 0	3.834(0)
X = 0.1	3.844(6)
X = 0.2	3.822(9)
X = 0.3	3.824(3)
X = 0.4	3.822(6)
X = 0.5	3.799(6)

*The average lattice parameter is calculated from the diffraction peaks of (110), (111), (200) and (211) planes.

3.2.2. Electrical conductivity analyses

The electrical conductivity of synthesized perovskites is shown in Figure 3.21. The result shows that the conductivity increases after doping small amount of Ca. The highest electrical conductivity is obtained at X = 0.2. When X >0.2, the conductivity is decreased but it is still higher than LSCF except at X = 0.5 which shows the lowest conductivity. Moreover, most of all Ca-doped perovskites have electrical conductivity similar to the undoped one. Their electrical conductivity increases with temperature to reach the maximum value at 550 °C and then decreases. Only X = 0.5 shows constant electrical conductivity in all temperature range.

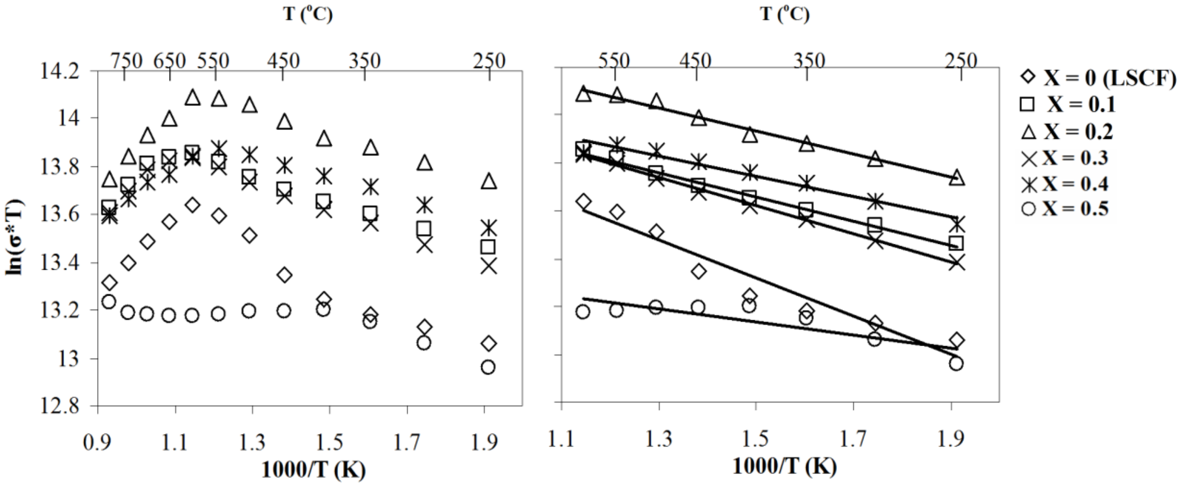

Figure 3.21. Electrical conductivity of $La_{0.3}Sr_{0.7-x}Ca_xCo_{0.9}Fe_{0.1}O_3$ (X = 0-0.5)

Table 3.4 Activation energy (E_a) of $La_{0.3}Sr_{0.7-x}Ca_xCo_{0.9}Fe_{0.1}O_3$ (X = 0-0.5).

Ca content	**E_a (kJ/mol)**
X = 0	6.5992 (250-600 °C)
X = 0.1	4.2312 (250-600 °C)
X = 0.2	4.0325 (250-600 °C)
X = 0.3	4.8864 (250-600 °C)
X = 0.4	3.5303 (250-600 °C)
X = 0.5	2.2806 (250-600 °C)

3.2.3 Oxygen permeation analyses

The oxygen permeation rate of $La_{0.3}Sr_{0.7-x}Ca_xCo_{0.9}Fe_{0.1}O_3$ (X = 0, 0.2, 0.5) discs is shown in Figure 3.22. It has been found that X = 0.5 shows higher oxygen permeation rate than others. The higher oxygen permeation rate of this sample may be explained by great oxygen reduction reaction (ORR) ability and bulk diffusion due to the large numbers of oxygen vacancies and active Co^{2+} cations. Moreover, the smaller size of Ca dopant is also a reason that supports bulk diffusion resulting in a high oxygen permeation rate.

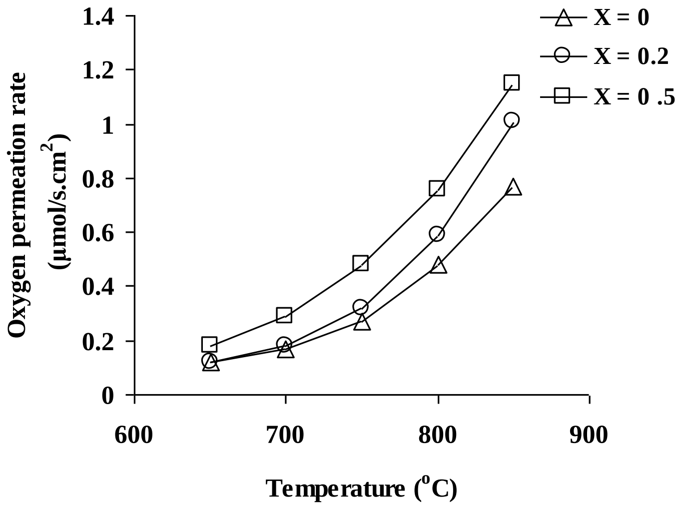

Figure 3.22. Oxygen permeation rate of $La_{0.3}Sr_{0.7-x}Ca_xCo_{0.9}Fe_{0.1}O_3$ (X = 0, 0.2, 0.5)

3.2.4. XPS analyses

From the C1*s* XPS spectra (Figure 3.23), the spectrum of $-CO_3^{2-}$ species at binding energy of ~288 eV indicates that $La_{0.3}Sr_{0.7-x}Ca_xCo_{0.9}Fe_{0.1}O_3$ has the amount of $-CO_3^{2-}$ as following sequence; X = 0.5 > X = 0.2 > X = 0.

The Ca2*p* spectra are shown in Figure 3.24. The Ca2$p_{3/2}$ and Ca2$p_{1/2}$ sub band of CaO locates at ~345eV and ~349 eV, respectively. The intense peak at ~346.5 eV is assigned to the Ca2$p_{3/2}$ sub band of $CaCO_3$ [48,78]. It can be concluded that Ca in these samples presents as both CaO and $CaCO_3$. The amount of $CaCO_3$ increases with increasing the Ca content.

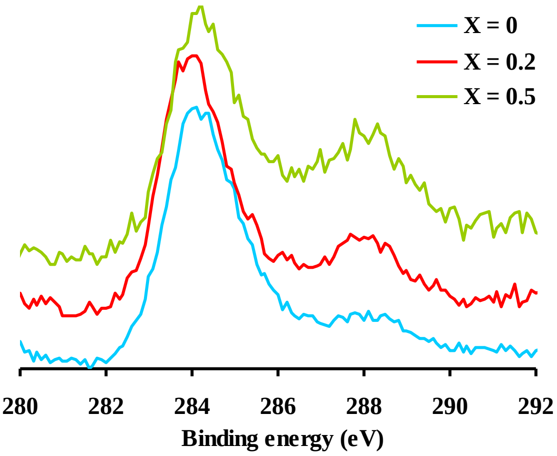

Figure 3.23. Normalized C1*s* core level XPS spectra of $La_{0.3}Sr_{0.7-x}Ca_xCo_{0.9}Fe_{0.1}O_3$ (X = 0, 0.2, 0.5)

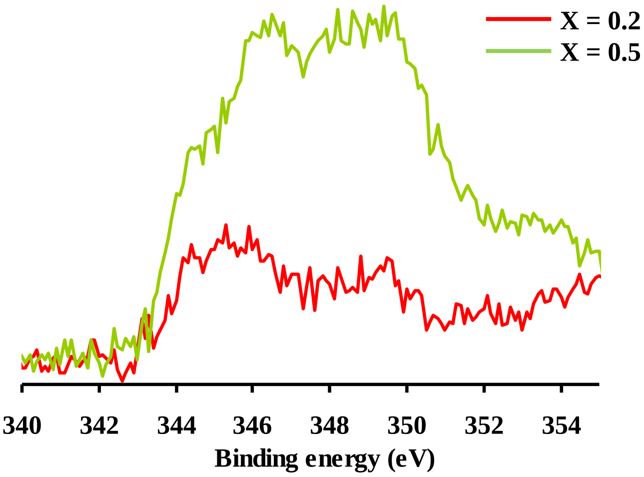

Figure 3.24. Ca2*p* core level XPS spectra of $La_{0.3}Sr_{0.7-x}Ca_xCo_{0.9}Fe_{0.1}O_3$ (X = 0.2, 0.5)

The La3$d_{5/2}$ sub bands of La_2O_3 (Figure 3.25) correspond to $3d^0f^{\,0}$ final state (~833.5 eV) and $3d^0f^{\,n}\underline{L}$ final state (~836 eV) resulted from the charge transfer from O2p to La4f orbitals. It is clear that the peak intensity of $3d^0f^{\,n}\underline{L}$ final state is increased with increasing the Ca content, which indicates strong charge transfer from O2p to La4f orbitals due to structural distortion.

The Sr3d XPS spectra are shown in Figure 3.26. The peaks at binding energy of ~131 and ~133 eV represent 3$d_{5/2}$ sub band of Sr^{2+} surrounded by oxygen vacancies in SrO_{1-x} sub oxide and of the regular Sr in perovskite lattice (SrO), respectively. The peak intensity of Sr in SrO_{1-x} sub oxide of X = 0.2 is lower than those of X = 0 and X = 0.5, suggesting the low content of oxygen vacancy on the surface of X = 0.2.

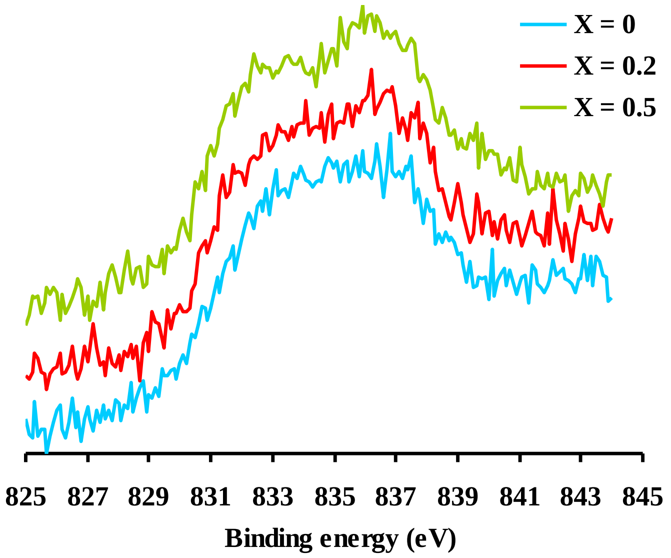

Figure 3.25. Normalized La3d core level XPS spectra of $La_{0.3}Sr_{0.7-x}Ca_xCo_{0.9}Fe_{0.1}O_3$ (X = 0, 0.2, 0.5)

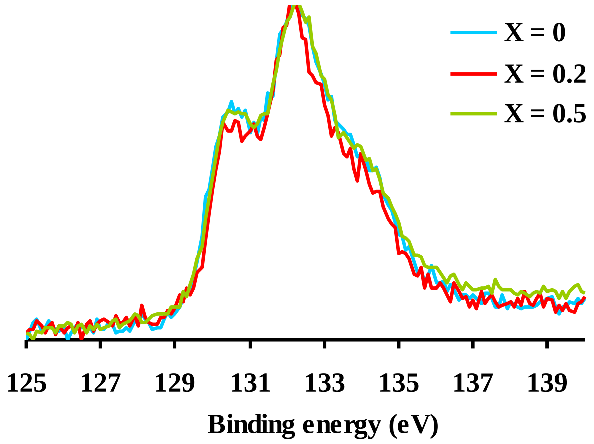

Figure 3.26. Normalized Sr3d core level XPS spectra of $La_{0.3}Sr_{0.7-x}Ca_xCo_{0.9}Fe_{0.1}O_3$ (X = 0, 0.2, 0.5)

From the O1*s* XPS spectra (Figure 3.27), LSCF with X = 0.5 exhibits strong peak intensity of adsorbed O_2^{2-} and O_2^{-} species locating at ~533-537 eV. This indicates high contents of adsorbed O_2^{2-} and O_2^{-} on the surface due to high surface ORR of the material.

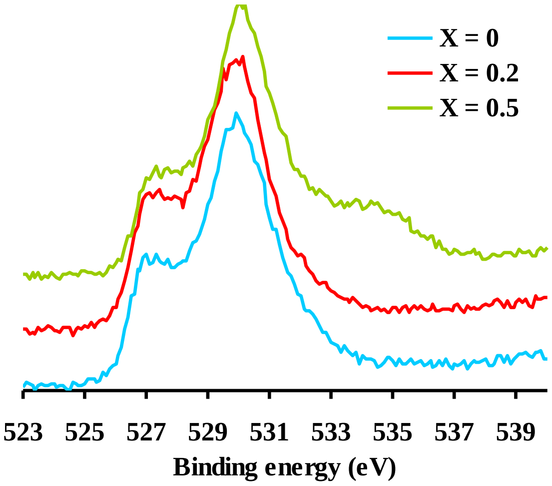

Figure 3.27. Normalized O1*s* core level XPS spectra of $La_{0.3}Sr_{0.7-x}Ca_xCo_{0.9}Fe_{0.1}O_3$ (X = 0, 0.2, 0.5)

Figure 3.28 shows the Fe2$p_{3/2}$ spectra. All samples exhibit the broadening Fe2$p_{3/2}$ peaks corresponding to the different form of Fe in the materials. For X = 0, the most intense peak locates at 712 eV which closes to BE of Fe^{3+} in (FeO)OH (711.6 eV) reported by Barr [53]. Upon doping Ca, the intense peaks at 711 and 710 eV, which belong to Fe^{3+} in Fe_2O_3 and Fe^{2+} in FeO, respectively, are observed [53,57]. In summary, the oxidation state of Fe change from high valence state (Fe^{3+}) to low valence state (Fe^{2+}) after replacing Sr^{2+} with Ca^{2+}.

From the Co2*p* XPS spectra (Figure 3.29), the ΔE for X = 0, 0.2 and 0.5 are 15.3, 15 and 15.5 eV, respectively. The high value indicates the large proportion of HS Co^{2+} [61]. Therefore, it can be concluded that Co presents as HS Co^{2+} for X = 0.5. For X = 0, the coexistence of LS Co^{3+} and HS Co^{2+} are observed due to the decreasing of both ΔE value and the HS Co^{2+} satellite shake up peak intensity. The low ΔE value and the absence of HS Co^{2+} satellite shake up peak of X = 0.2 are distributed to LS Co^{3+}.

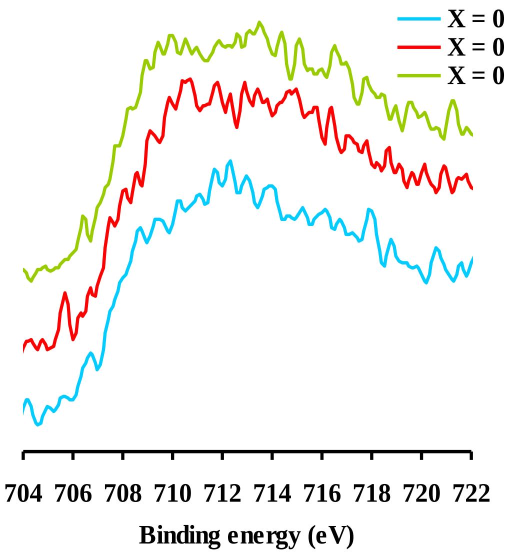

Figure 3.28. Normalized Fe2$p_{3/2}$ core level XPS spectra of $La_{0.3}Sr_{0.7-x}Ca_xCo_{0.9}Fe_{0.1}O_3$ (X = 0, 0.2, 0.5)

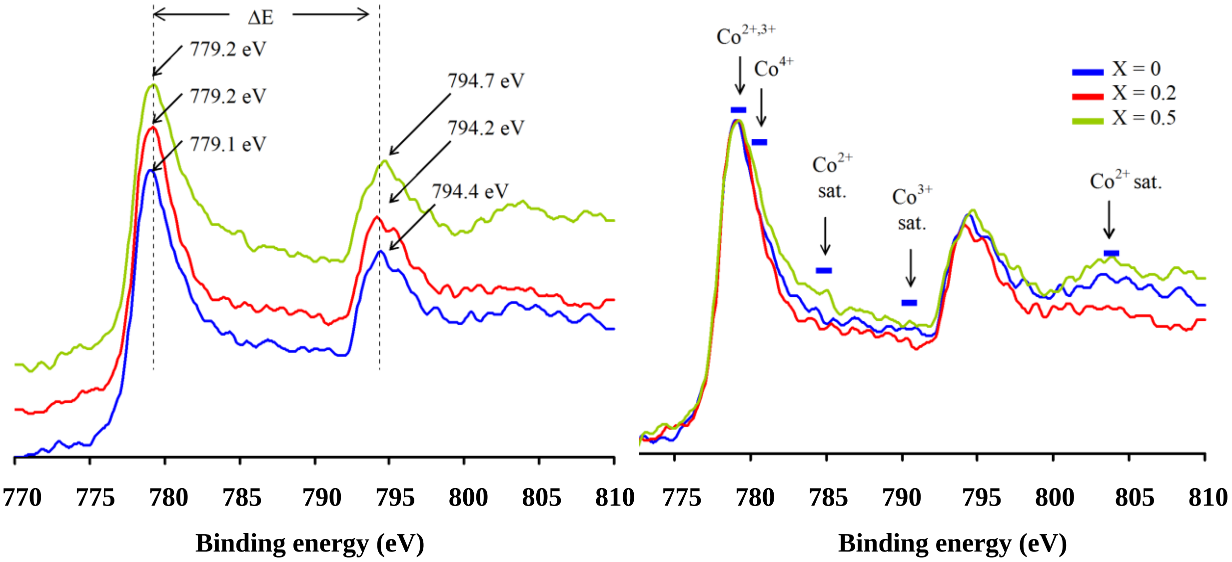

Figure 3.29. Normalized Co2p core level XPS spectra of $La_{0.3}Sr_{0.7-x}Ca_xCo_{0.9}Fe_{0.1}O_3$ (X = 0, 0.2, 0.5)

3.2.5 XAS analyses

3.2.5.1 La M-edge X-ray absorption spectroscopy.

The La M-edge spectra in Figure 3.30 represent the transition of electrons from 3*d* to 4*f* orbitals. The high absorption intensity of X = 0 suggests low electron density in La4*f* orbital which designates weak charge transfer from O2*p* orbital to La4*f* orbital.

The samples with X = 0.2 and X = 0.5 show weak absorption intensity suggesting high electron density in La4*f* orbital. This indicates strong charge transfer from O2*p* orbital to La4*f* orbital. The result is similar to La3*d* XPS result.

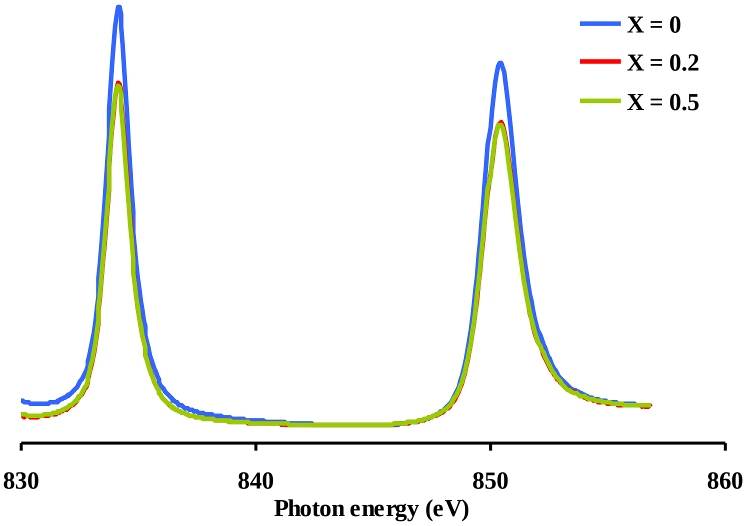

Figure 3.30. Normalized La3*d* X-ray absorption spectra of $La_{0.3}Sr_{0.7-x}Ca_xCo_{0.9}Fe_{0.1}O_3$ (X = 0, 0.2, 0.5)

3.2.5.2 Co L-edge X-ray absorption spectroscopy.

Figure 3.30 shows the X-ray absorption spectra assigned to Co2*p* → Co3*d* transition. The sample with X = 0.2 exhibits the highest peak intensity suggesting low electron density in Co3*d* orbital. This indicates weak charge transfer from O2*p* to Co3*d* due to the distortion of Co-O-Co bond, and the high content of Co^{4+} [74].

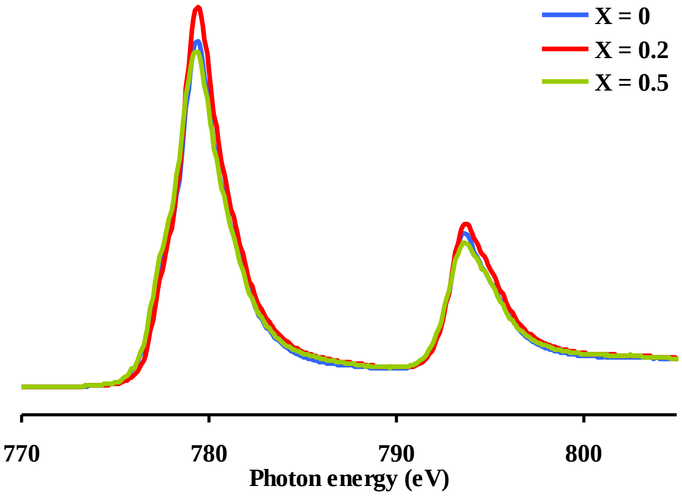

Figure 3.31. Normalized Co2*p* X-ray absorption spectra of $La_{0.3}Sr_{0.7-x}Ca_xCo_{0.9}Fe_{0.1}O_3$ (X = 0, 0.2, 0.5).

3.2.5.3 O K-edge X-ray absorption spectroscopy (O K-edge XAS)

From the O K-edge XAS (Figure 3.32), feature A represents the transition of electrons from O1*s* orbital of lattice O^{2-} to hybridized O2*p*-t_{2g}^{*} hole state dominated by HS Co^{3+}. While feature B and C represent the transition of electrons from O1*s* orbital of lattice O^{2-} hybridized O2*p*-e_g^{*} hole state, which is dominated by LS Co^{3+} and IS Co^{4+}, respectively.

The absorption intensity of feature B and C of the sample with X = 0.2 is higher than those of X = 0 and X = 0.5, respectively. This suggests the high quantity of O2*p*-e_g^{*} hole state in the series of X = 0.2 > X = 0 > X = 0.5. As discussed previously in section 3.1.6.1, Co^{2+} has affected on the transition of feature B and C, thus, it can be concluded that the quantities of LS Co^{3+} and IS Co^{4+} are in the following sequence: the sample with X = 0.2 > X = 0 > X = 0.5, while that of Co^{2+} is in the series of the sample with X = 0.5 > X = 0 > X = 0.2. The absorption intensity of feature A of the sample with X = 0.2 is higher than those of X = 0.5 and X = 0, respectively. This also indicates the order of HS Co^{3+} content as follow: the sample with X = 0.2 > X = 0.5 > X =

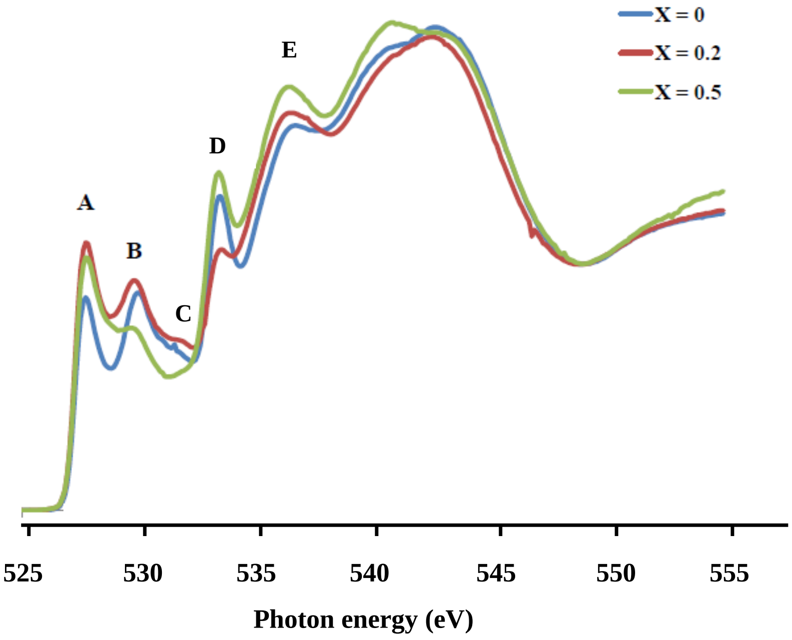

Figure 3.32. Normalized O K-edge region X-ray absorption spectra of $La_{0.3}Sr_{0.7-x}Ca_xCo_{0.9}Fe_{0.1}O_3$ (X = 0, 0.2, 0.05)

Feature D can be assigned to the transition of electrons from σ_{1s} orbital to σ^* resonance of adsorbed O_2^- species produced by Co^{2+} species and oxygen vacancies in the structure. It is revealed that the amount of adsorbed oxygen at X = 0.5 is higher than those of X = 0 and X = 0.2, suggesting high Co^{2+} and oxygen vacancy contents in X = 0.5 comparing to X = 0 and X = 0.2. The result is in agreement with XPS results.

Feature E corresponds to the transition of electrons from O1*s* orbital of lattice O^{2-} to hybridized O2*p*-La5*d*/Sr4*d* hole state. The absorption intensity of this feature increases with the Ca content. This corresponds to the strong Sr-O and La-O bond covalency, and the strong charge transfer from O2*p* to La5*d*/Sr4*d* orbitals due to structural distortion. This result is also in agreement with La3*d* XPS, La M-edge and Co L-edge XAS results.

From XPS and XAS analysis, the properties of material with X = 0.2, e.g., the decrease of lattice parameter, high electrical conductivity and low E_a value, are due to HS Co^{3+} and IS Co^{4+}. For the sample with X = 0.5, its low and temperature-independent electrical conductivity, and high oxygen permeation are due to high quantities of HS Co^{2+} and oxygen vacancy.

3.3 Synthesis and properties of $(La_{0.3}Sr_{0.7})_{1-x}Ca_xCo_{0.9}Fe_{0.1}O_3$

3.3.1 XRD analyses

XRD spectra of $(La_{0.3}Sr_{0.7})_{1-x}Ca_xCo_{0.9}Fe_{0.1}O_3$ (X = 0-0.4)**,** Figure 3.33, indicate pure phase of primitive cubic perovskite structure when X = 0-0.2. When X = 0.3, the intensity of 100 and 110 peaks decreases and absolutely disappears when X = 0.4. This suggests phase transformation from cubic to tetragonal structure. The calculated lattice parameters of all samples are shown in Table 3.5. Despite of smaller size of Ca ions comparing to Sr ions, the sample with X = 0.1 exhibits slightly higher lattice parameter than the undoped one. This may be because of high content of Co^{2+}.

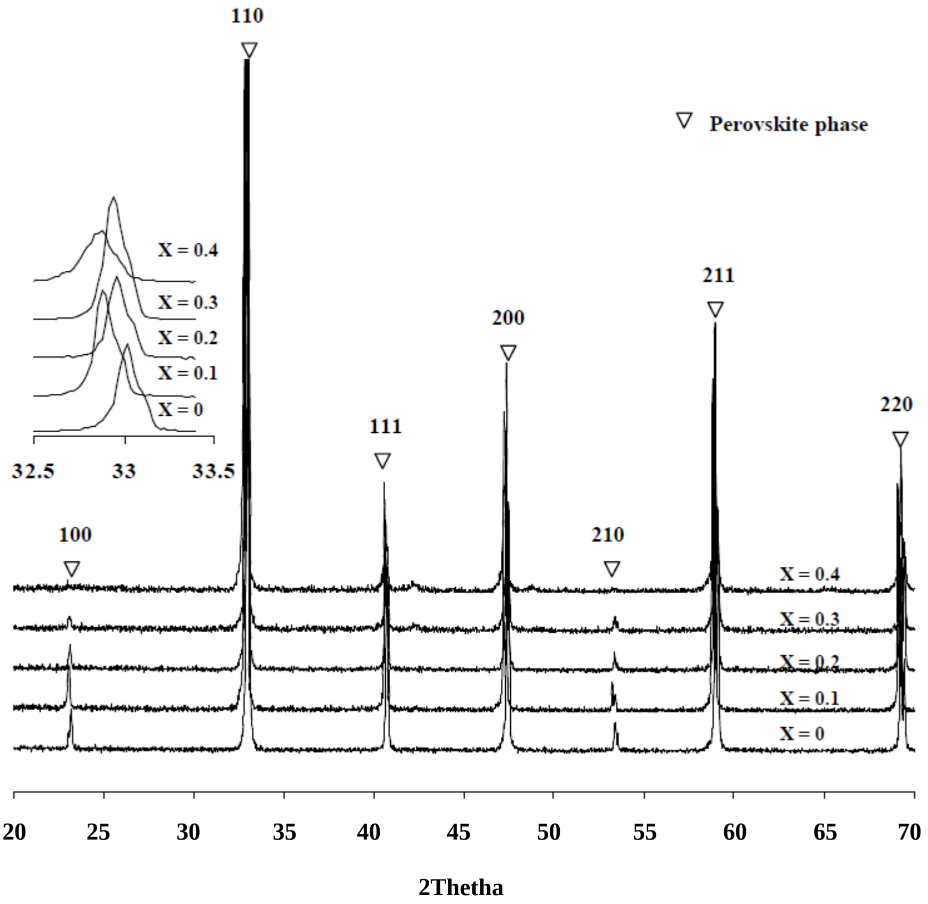

Figure 3.33. XRD patterns of $(La_{0.3}Sr_{0.7})_{1-x}Ca_xCo_{0.9}Fe_{0.1}O_3$ (X = 0 – 0.4) sintered at 1,200 ^{o}C for 6 hrs

Table 3.5. Lattice parameters of $(La_{0.3}Sr_{0.7})_{1-x}Ca_xCo_{0.9}Fe_{0.1}O_3$ (X = 0 – 0.4)

Ca content	Phase structure	*Lattice parameter (Å)
X = 0	Cubic	3.841(7)
X = 0.1	Cubic	3.845(7)
X = 0.2	Cubic	3.837(8)
X = 0.3	Tetragonal	a = 3.836(1) c = 3.848(2)
X = 0.4	Tetragonal	a = 3.827(5) c = 3.871(6)
X = 0.5	Melt	-

*****The average lattice parameter is calculated from the diffraction peaks of (110), (111), (200) and (211) planes.

3.3.2 Electrical conductivity analyses

From Figure 3.34, the highest electrical conductivity is achieved when X = 0.1 and it decreases with the increasing of Ca content. However, the electrical conductivity of Ca-doped perovskites is still higher than LSCF except for X = 0.4. The electrical conductivity behavior of all Ca-doped perovskites is similar to the undoped one, it increases with temperature and reaches the maximum value at 550 ^{o}C and then decreases. The E_a value increases with increasing Ca content. The lowest E_a value is obtained at X = 0.1, which may result from high HS Co^{3+} and Co^{4+} contents. On the contrary, the low electrical conductivity and high E_a value of X = 0.4 are resulted from the phase transformation from cubic to tetragonal structure which provides weak orbital overlapping. These assumptions will be discussed further in the O K-edge XAS analysis, section 3.3.5.3.

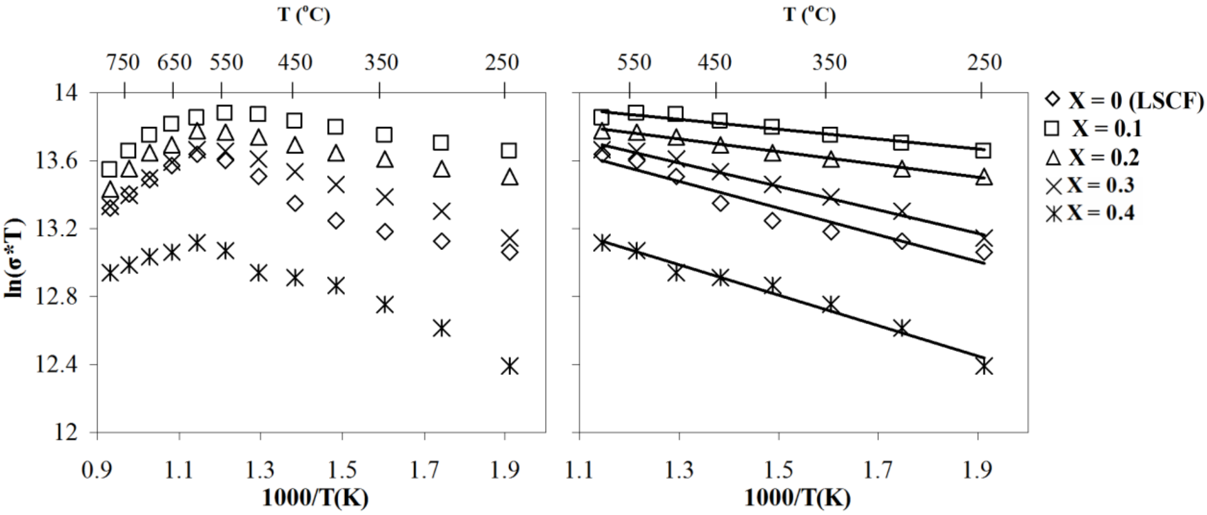

Figure 3.34. Electronic conductivities of $(La_{0.3}Sr_{0.7})_{1-x}Ca_xCo_{0.9}Fe_{0.1}O_3$ (X = 0-0.4).

Table 3.6. Activation energy (E_a) of $(La_{0.3}Sr_{0.7})_{1-x}Ca_xCo_{0.9}Fe_{0.1}O_3$ (X = 0-0.4).

Ca content	**E_a (kJ/mol)**
X = 0	6.5992 (250-600 °C)
X = 0.1	2.4943 (250-600 °C)
X = 0.2	3.1420 (250-600 °C)
X = 0.3	5.7046 (250-600 °C)
X = 0.4	7.4473 (250-600 °C)

3.3.3 Oxygen permeation analyses

The oxygen permeation rates of $(La_{0.3}Sr_{0.7})_{1-x}Ca_xCo_{0.9}Fe_{0.1}O_3$ (X = 0, 0.1, 0.4) discs are shown in Figure 3.35. It has been found that X = 0.1 shows higher oxygen permeation rate than those of other ones. The higher oxygen permeation rate of this sample can be explained by great bulk diffusion due to large unit cell parameter providing more space in the structure. Its great oxygen ORR ability is also expected. But for X = 0.4, the symmetry of tetragonal structure may affect the bulk diffusion.

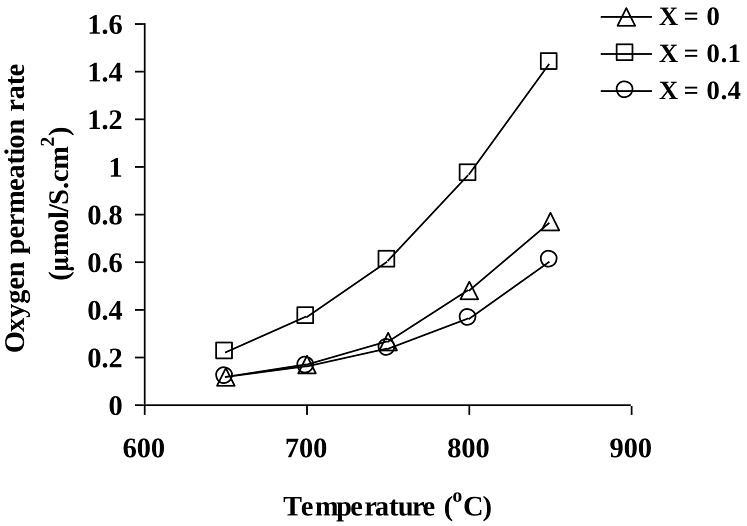

Figure 3.35. Oxygen permeation rate of $(La_{0.3}Sr_{0.7})_{1-x}Ca_xCo_{0.9}Fe_{0.1}O_3$ (X = 0, 0.1, 0.4)

3.3.4 XPS analyses

From the C1*s* XPS spectra (Figure 3.36), the sample with X = 0.4 shows the highest peak intensity of $-CO_3^{2-}$ species at ~288 eV followed by X = 0.1 and X = 0, respectively. This indicates that the quantity of $-CO_3^{2-}$ increases with increasing the Ca content.

The Ca2*p* spectra are shown in Figure 3.37. The sample with X = 0.4 exhibits strong intensity of Ca2$p_{3/2}$ sub band of $CaCO_3$ (~346.5eV). This indicates the high content of $CaCO_3$ in this sample.

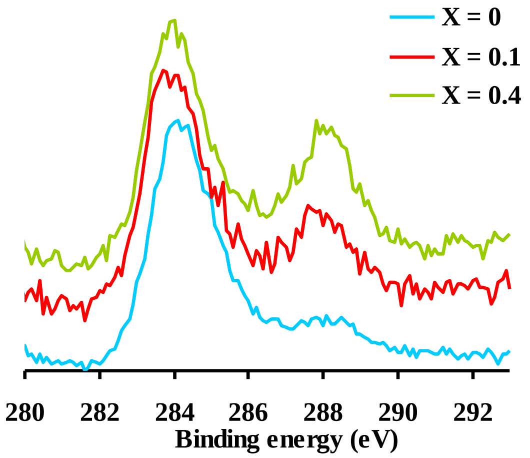

Figure 3.36. Normalized C1*s* core level XPS spectra of $(La_{0.3}Sr_{0.7})_{1-x}Ca_xCo_{0.9}Fe_{0.1}O_3$ (X = 0, 0.1, 0.4)

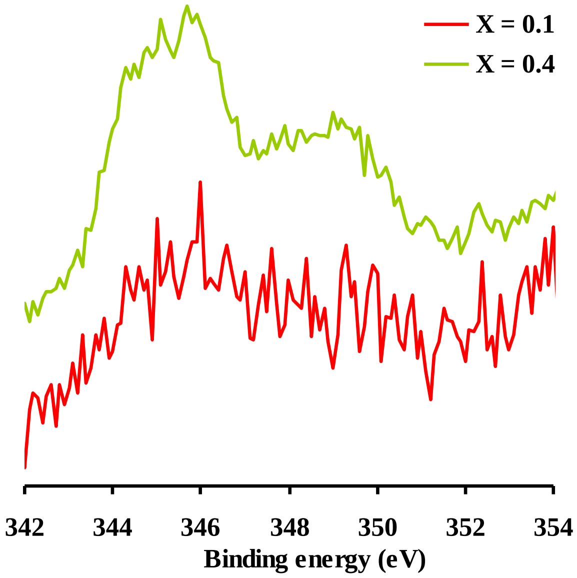

Figure 3.37. Normalized Ca2*p* core level XPS spectra of $(La_{0.3}Sr_{0.7})_{1-x}Ca_xCo_{0.9}Fe_{0.1}O_3$ (X = 0, 0.1, 0.4)

The doublet La3$d_{5/2}$ peak of La_2O_3 (Figure 3.38) indicates inequivalent La ions due to different final states: $3d^0f^0$ final state (~833.5 eV), and $3d^0f^n\underline{L}$ final state (~836 eV). It has been shown that the peak intensity of $3d^0f^n\underline{L}$ final state increases when Ca ions are introduced into the structure. This indicates strong charge transfer from O2*p* to La4*f* orbitals due to structural distortion.

The Sr3*d* XPS spectra are shown in Figure 3.39. The peaks locating at ~131 and ~133 eV correspond to the $3d_{5/2}$ sub band of Sr^{2+} surrounded by oxygen vacancies in SrO_{1-x} sub oxide and of the regular Sr in perovskite lattice (SrO), respectively. The peak intensity of Sr in SrO_{1-x} sub oxide of X = 0.4 is lower than those of others. This indicates the low quantity of oxygen vacancy in this sample.

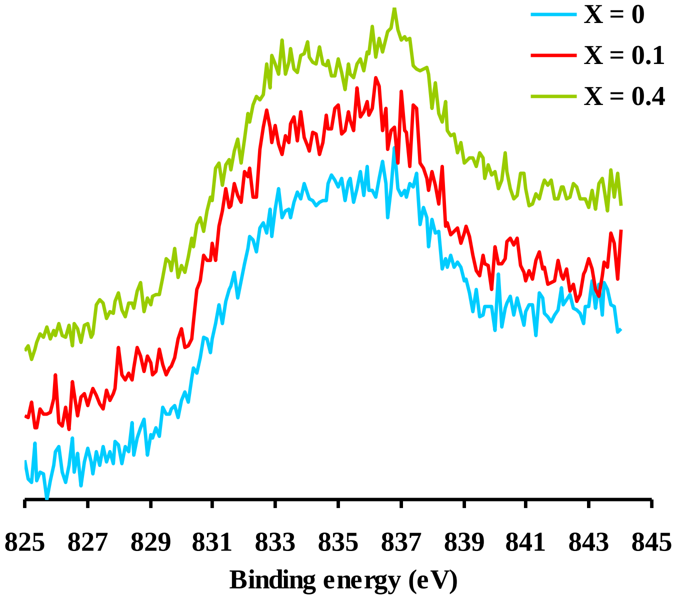

Figure 3.38. Normalized La3*d* core level XPS spectra of $(La_{0.3}Sr_{0.7})_{1-x}Ca_xCo_{0.9}Fe_{0.1}O_3$ (X = 0, 0.1, 0.4)

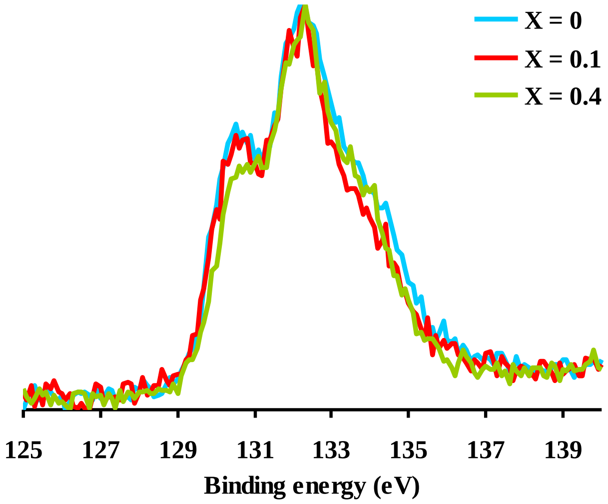

Figure 3.39. Normalized Sr3*d* core level XPS spectra of $(La_{0.3}Sr_{0.7})_{1-x}Ca_xCo_{0.9}Fe_{0.1}O_3$ (X = 0, 0.1, 0.4)

From the O1*s* XPS spectra, Figure 3.40, the sample with X = 0.4 exhibits strong peak intensity of adsorbed -OH specie which locates at ~530 eV. This indicates high quantity of –OH. This specie will block the active Co^{2+} and oxygen vacancy sites for ORR, leading to the decrease of ORR ability of the material [79].

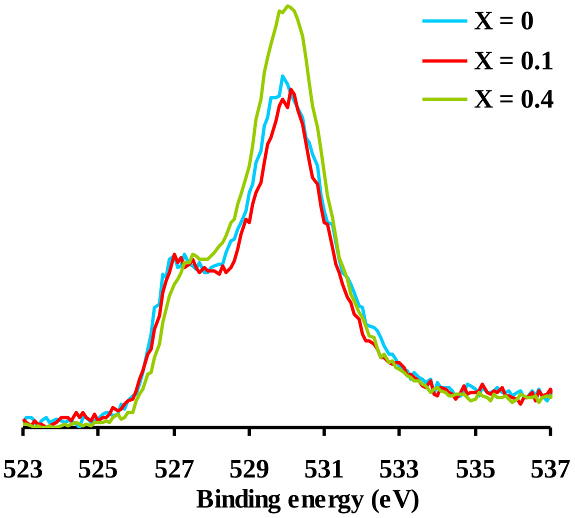

Figure 3.40. Normalized O1*s* core level XPS spectra of $(La_{0.3}Sr_{0.7})_{1-x}Ca_xCo_{0.9}Fe_{0.1}O_3$ (X = 0, 0.1, 0.4)

From the Co2*p* XPS spectra, the ΔE values for the samples with X = 0, 0.1 and 0.4 are 15.3, 15.4 and 15.2 eV, respectively. These values indicate the low proportion of HS Co^{2+}. The intensity of Co^{2+} satellite shake up peak decreases with increasing the Ca content, reflecting to the decrease of HS Co^{2+} amount.

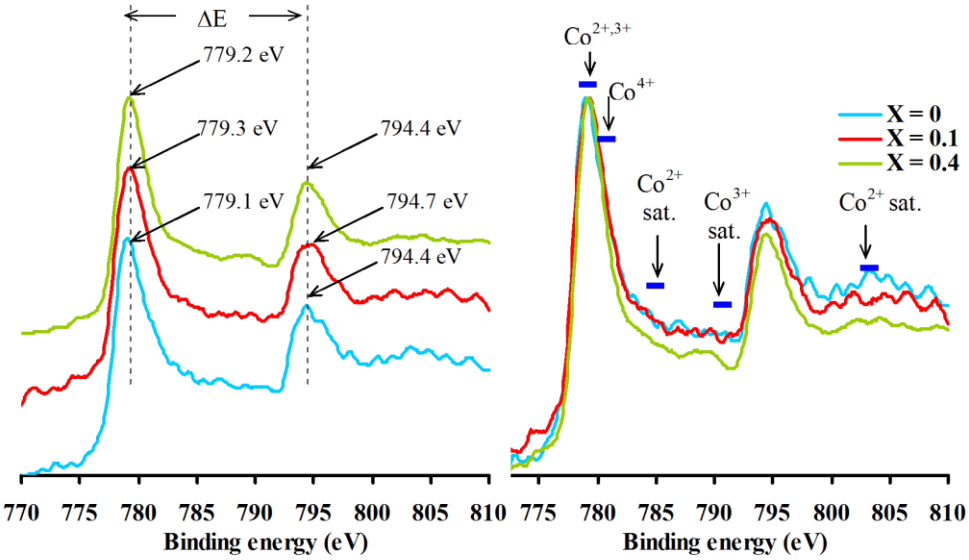

Figure 3.41. Normalized Co2*p* core level XPS spectra of $(La_{0.3}Sr_{0.7})_{1-x}Ca_xCo_{0.9}Fe_{0.1}O_3$ (X = 0, 0.1, 0.4)

3.3.5 XAS analyses

3.3.5.1 La M-edge X-ray absorption spectroscopy (La M-edge XAS)

From the La M-edge spectra (Figure 3.42), the sample with X = 0.4 shows the highest absorption intensity indicating high electron density in La4*f* orbital due to weak charge transfer from O2*p* orbital to La4*f* orbital. This is consequence of the expansion of unit cell along *c* axis in tetragonal structure leading to the long distance between La and O ions. For X = 0.1, its weak absorption intensity indicates strong charge transfer from O2*p* orbital to La4*f* orbital due to structural distortion. The result is consistent with La3*d* XAS result.

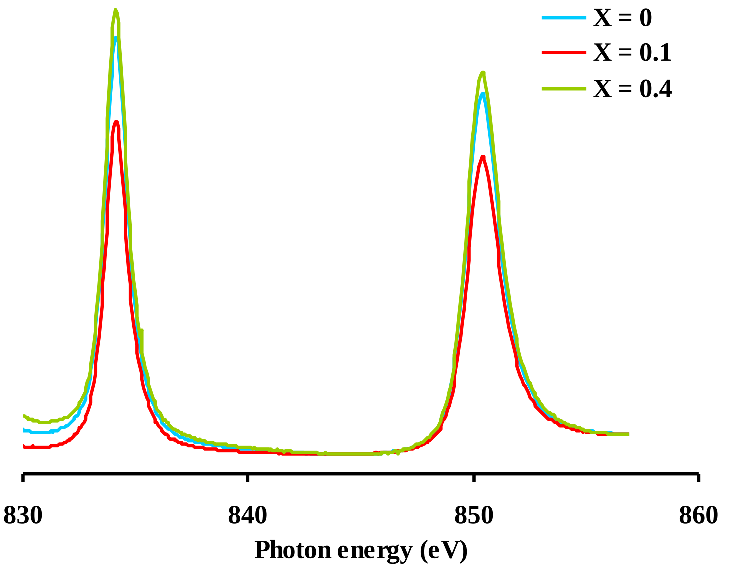

Figure 3.42. Normalized La M-edge region X-ray absorption spectra of $(La_{0.3}Sr_{0.7})_{1-x}Ca_xCo_{0.9}Fe_{0.1}O_3$ (X = 0, 0.1, 0.4)

3.3.5.2 Co L-edge X-ray absorption spectroscopy (Co L-edge XAS)

From the Co L-edge XAS, Figure 3.43, the highest absorption intensity of X = 0.1 attributes to low electron density in Co3*d* orbital. This reflects to weak charge transfer from O2*p* to Co3*d* due to the distortion of Co-O-Co bond. On the contrary, the sample with X = 0 and X = 0.4 show low absorption intensity suggesting high electron density in Co3*d* orbital resulted from strong charge transfer from O2*p* to Co3*d* due to the good alignment of Co-O-Co bond. Moreover, the short distance between Co and O ions along *a* axis in tetragonal structure is a plausible reason for low absorption intensity of the sample with X = 0.4

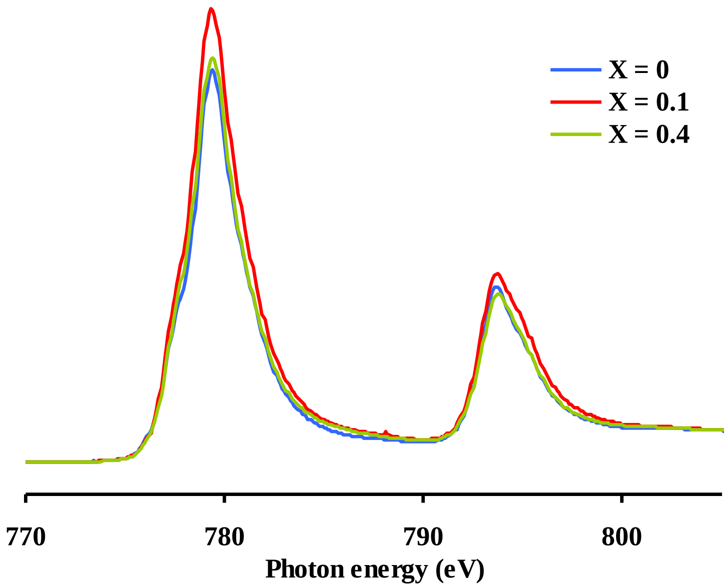

Figure 3.43. Normalized Co L-edge region X-ray absorption spectra of $(La_{0.3}Sr_{0.7})_{1-x}Ca_xCo_{0.9}Fe_{0.1}O_3$ (X = 0, 0.1, 0.4)

3.3.5.3 O K-edge X-ray absorption spectroscopy (O K-edge XAS)

From the O K-edge XAS (Figure 3.44), feature A corresponds to the transition of electrons from O1*s* orbital of lattice O^{2-} to hybridized O2*p*-t_{2g}^* hole state. This feature is dominated by HS Co^{3+}. Feature B and C relate to the transition of electrons from O1*s* orbital of lattice O^{2-} hybridized O2*p*-e_g^* hole state which is influenced by LS Co^{3+} and IS Co^{4+}, respectively.

For feature B, the sample with X = 0 illustrates the highest absorption intensity followed by X = 0.4 and X = 0.1, respectively. This indicates that the content of LS Co^{3+} is in the following sequence: the sample with X = 0 > X = 0.4 > X = 0.1.

The sample with X = 0.1 shows the higher intensity of feature A than those of the sample with X = 0.4 and X = 0, respectively. This reflects the high content of HS Co^{3+} in the series of X = 0.1 > X = 0.5 > X = 0.

The large proportion of HS Co^{3+} results in the increase in lattice parameter and electrical conductivity of the sample with X = 0.1 as explained previously in section 3.1.3. Moreover, HS Co^{3+} affects the great oxide ion diffusion through the bulk of mareial because HS Co^{3+} (r = 0.61 Å) has larger size than LS Co^{3+} (r = 0.545 Å) leading to weak bond strength between Co and O ions as explained in section 3.1.4. For the sample with X = 0.4, LS Co^{3+} is responsible for low electrical conductivity and oxygen permeation properties.

Feature D associates with the transition of electrons from σ_{1s} orbital to σ^* resonance of adsorbed O_2^-. The low absorption intensities of the samples with X = 0.1 and 0.4 correspond to the low content of adsorped O_2^- due to low ORR ability, which results from the low quantity of oxygen vacancy, and the high quantity of surface –OH as shown in Sr3*d* and O1*s* XPS spectra.

Although the sample with X = 0.1 has low ORR ability, it exhibits high oxygen permeation. This indicates that the ORR ability is not the important factor for oxygen permeation. This view is also reported by Diethelm [80] that the oxygen permeation at the temperature range < 850 °C is more influenced by the oxide ion diffusion than ORR ability.

Feature E relates to the transition of electrons from O1*s* orbital of lattice O^{2-} to hybridized O2*p*-La5*d*/Sr4*d* hole state. The absorption intensity of this feature increases with the Ca content indicating to strong Sr-O and La-O bond covalency and LMCT due to structural distortion. This result is in agreement with La3*d* XPS and Co L-edge XAS results.

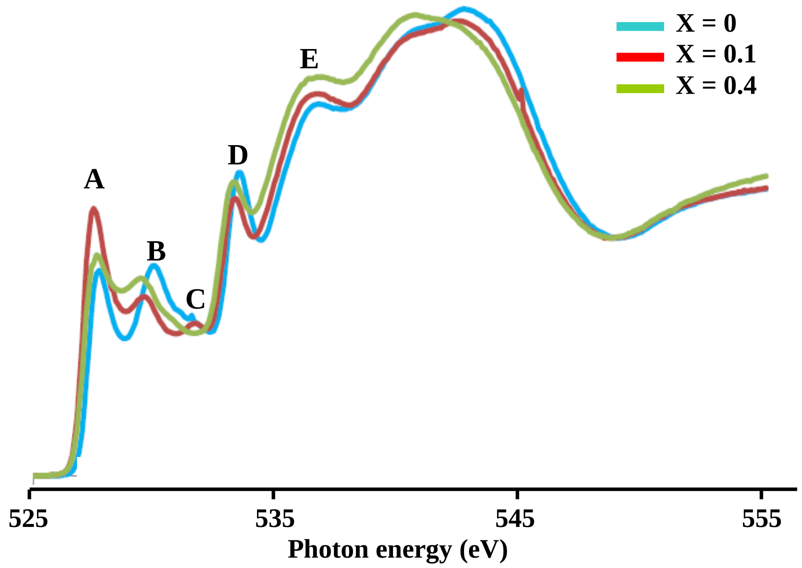

Figure 3.44. Normalized O K-edge region X-ray absorption spectra of $(La_{0.3}Sr_{0.7})_{1-x}Ca_xCo_{0.9}Fe_{0.1}O_3$ (X = 0, 0.1, 0.4)

From the study of Ca-doped perovskites, electrical conductivity of LSCF can be improved by doping Ca in the structure. The highest electrical conductivity is observed on $La_{0.3}Sr_{0.5}Ca_{0.2}Co_{0.9}Fe_{0.1}O_3$. This sample also shows higher oxygen permeation rate comparing to LSCF. According to such great properties, $La_{0.3}Sr_{0.5}Ca_{0.2}Co_{0.9}Fe_{0.1}O_3$ is chosen for improving oxygen permeation in the next study by doping Zn and Mg in the structure.

3.4 Synthesis and properties of $La_{0.3}Sr_{0.5}Ca_2Co_{0.9-y}Zn_yFe_{0.1}O_3$

3.4.1 XRD analyses

The XRD spectra of $La_{0.3}Sr_{0.5}Ca_2Co_{0.9-y}Zn_yFe_{0.1}O_3$ (Y = 0-0.05), Figure 3.45, indicate pure phase of perovskite structure with primitive cubic form when Y = 0-0.03. When Y = 0.04-0.05, an impurity phase is observed. The lattice parameter increases with the Zn content, which corresponds to the changing in oxidation state and/or electronic configuration of Co cation.

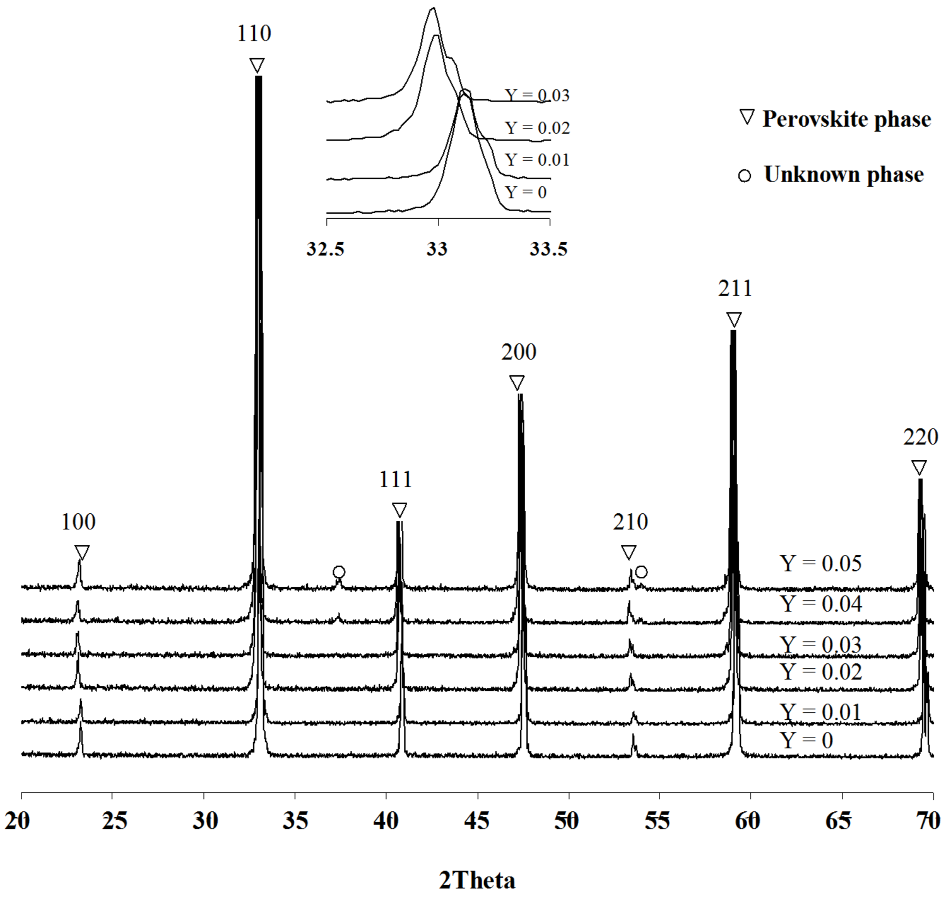

Figure 3.45. XRD patterns of $La_{0.3}Sr_{0.5}Ca_2Co_{0.9-y}Zn_yFe_{0.1}O_3$ (Y = 0-0.05) sintered at 1,200 °C for 6 hrs

Table 3.7. Lattice parameters of $La_{0.3}Sr_{0.5}Ca_2Co_{0.9-y}Zn_yFe_{0.1}O_3$ (Y = 0-0.03) perovskites sintered at 1200 °C for 6 hrs

Ca content	***Lattice parameter (Å)**
Y = 0	3.822(9)
Y = 0.01	3.822(8)
Y = 0.02	3.834(8)
Y = 0.03	3.837(2)

*****The average lattice parameter is calculated from the diffraction peaks of (110), (111), (200) and (211) planes.

3.4.2 Electrical conductivity analyses

The electrical conductivity of LSCF and $La_{0.3}Sr_{0.5}Ca_2Co_{0.9-y}Zn_yFe_{0.1}O_3$ (Y = 0-0.03) is shown in Figure 3.46. The electrical conductivity decreases with increasing the Zn content. However, the electrical conductivities of Zn-doped perovskites are still higher than LSCF except Y = 0.03, which the conductivity is equal to that of LSCF. The electrical conductivity of all perovskites increases with temperature and reaches the maximum value at 550 – 600 °C.

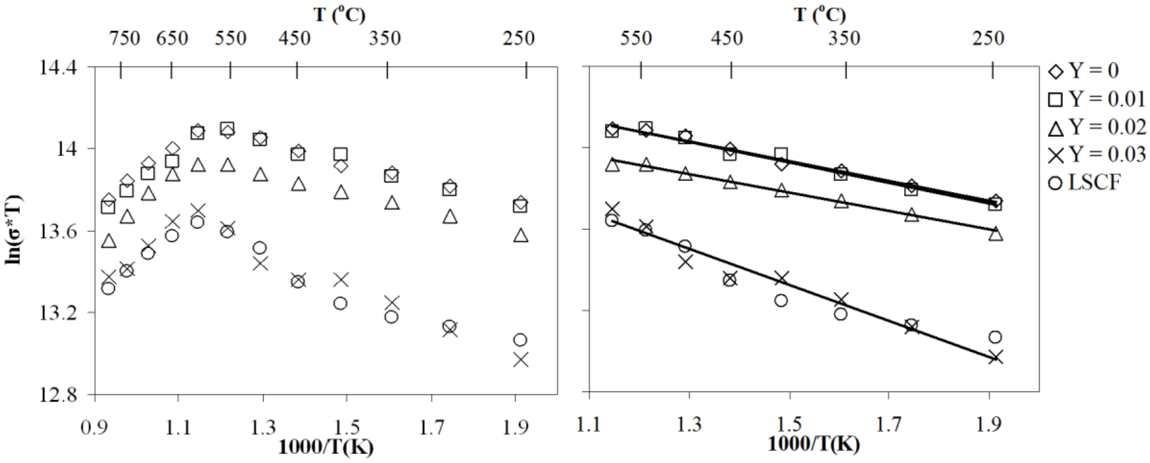

Figure 3.46. Electronic conductivities of LSCF and $La_{0.3}Sr_{0.5}Ca_2Co_{0.9-y}Zn_yFe_{0.1}O_3$ (Y = 0-0.03)

Table 3.8. Activation energy (E_a) of $La_{0.3}Sr_{0.5}Ca_2Co_{0.9-y}Zn_yFe_{0.1}O_3$ (Y = 0-0.03)

Zn content	E_a (kJ/mol)
Y = 0	4.0325 (250-600 °C)
Y = 0.01	4.1789 (250-600 °C)
Y = 0.02	3.7914 (250-600 °C)
Y = 0.03	7.3733 (250-600 °C)

3.4.3 Oxygen permeation analyses

The oxygen permeation rates of LSCF and $La_{0.3}Sr_{0.5}Ca_2Co_{0.9-y}Zn_yFe_{0.1}O_3$ (Y = 0, 0.01, 0.03) discs are shown in Figure 3.47. It has been found that Y = 0.03 shows the highest oxygen permeation rate. This can be deduced from great oxygen ORR ability and bulk diffusion due to high unit cell parameter, Co^{2+} and oxygen vacancy contents.

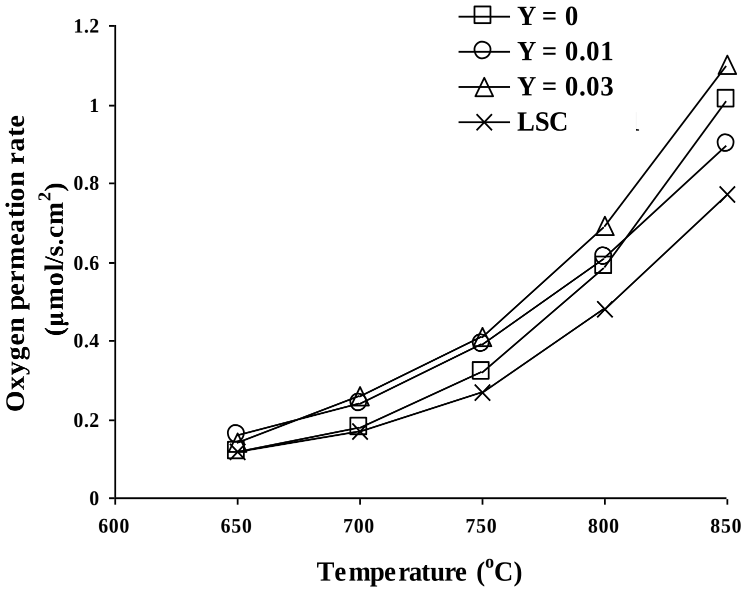

Figure 3.47. Oxygen permeation rate of LSCF and $La_{0.3}Sr_{0.5}Ca_2Co_{0.9-y}Zn_yFe_{0.1}O_3$ (Y = 0, 0.01, 0.03)

3.4.4 XPS analyses

From the C1*s* XPS spectra (Figure 3.48), after introducing Zn ions in the structure, the peak intensity of $-CO_3^{2-}$ specie at ~288 eV is increased, which indicates the high quantity of $-CO_3^{2-}$.

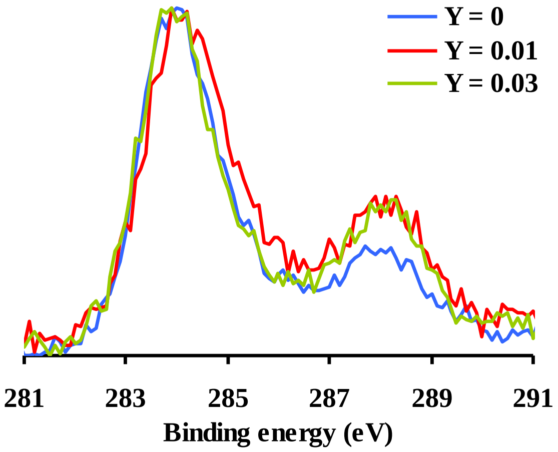

Figure 3.48. Normalized C1*s* core level XPS spectra of $La_{0.3}Sr_{0.5}Ca_2Co_{0.9-y}Zn_yFe_{0.1}O_3$ (Y = 0, 0.01, 0.03)

The Sr3*d* XPS spectra are shown in Figure 3.49. The peak intensity of Sr surrounded by oxygen vacancies (~131 eV) of the sample with Y = 0.03 is higher than those of others, reflecting to the high quantity of oxygen vacancy in this material. On the contrary, the sample with Y = 0.1 exhibits the lowest peak intensity of Sr surrounded by oxygen vacancies, which indicates the low content of oxygen vacancy.

From the Co2*p* XPS spectra, the ΔE values for the samples with Y = 0, 0.01 and 0.03 are 15.2, 15.2 and 14.9 eV, respectively. These values indicate LS Co^{3+}. The intensity of HS Co^{2+} satellite shake up peak of the sample with Y = 0.01 is lower than those of others, reflecting to the low content of HS Co^{2+}.

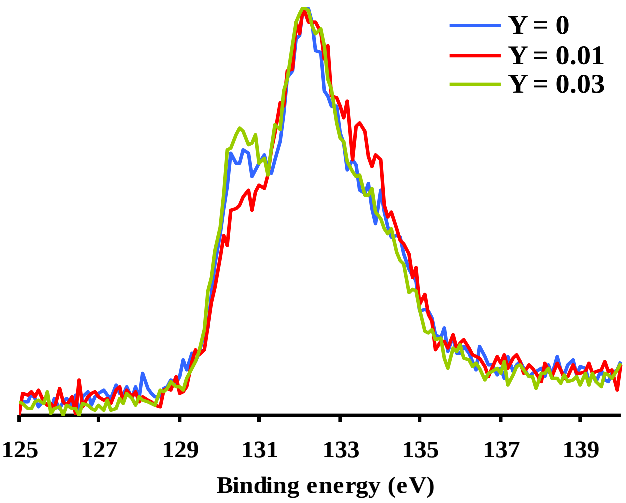

Figure 3.49. Normalized Sr3*d* core level XPS spectra of $La_{0.3}Sr_{0.5}Ca_2Co_{0.9-y}Zn_yFe_{0.1}O_3$ (Y = 0, 0.01, 0.03)

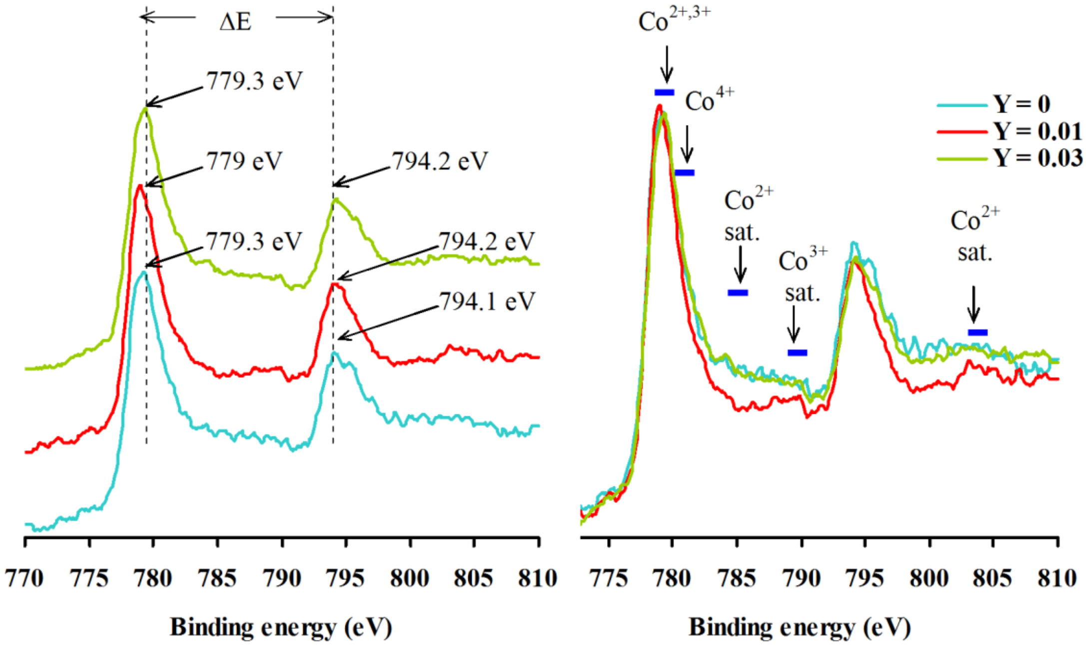

Figure 3.50. Normalized Co2*p* core level XPS spectra of $La_{0.3}Sr_{0.5}Ca_2Co_{0.9-y}Zn_yFe_{0.1}O_3$ (Y = 0, 0.01, 0.03)

3.4.5 XAS analyses

3.4.5.1 La L-edge X-ray absorption spectroscopy (La L-edge XAS)

The La M-edge spectra (Figure 3.51) relate to the transition of electrons from La3*d* to La4*f* orbitals. The sample with Y = 0.01 shows the highest absorption intensity indicating low electron density in La4*f* orbital due to weak due to charge transfer from O2*p* to La4*f* orbitals. This reflects the weak structural distortion of the material. On the other hand, the sample with Y = 0.03 shows the lowest absorption intensity relating to high electron density in La4*f* orbital strong due to structural distortion.

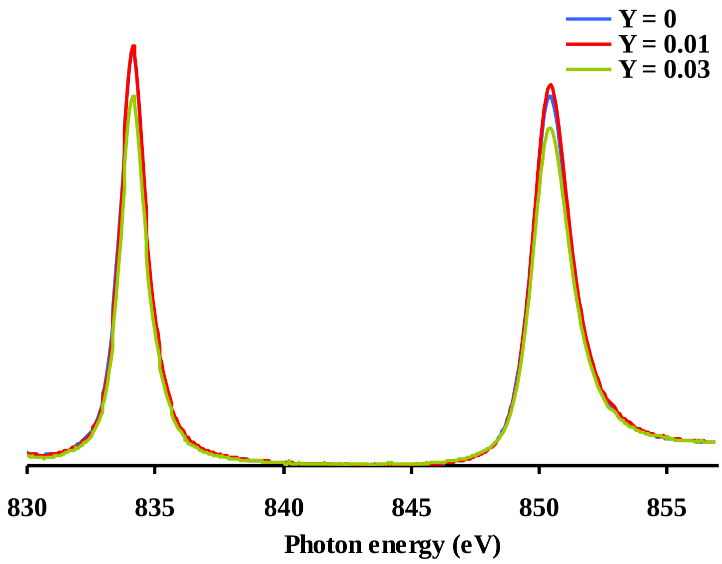

Figure 3.51. Normalized La L-edge region X-ray absorption spectra of $La_{0.3}Sr_{0.5}Ca_2Co_{0.9-y}Zn_yFe_{0.1}O_3$ (Y = 0, 0.01, 0.03)

3.4.5.2 Co L-edge X-ray absorption spectroscopy (Co L-edge XAS)

Co L-edge XAS spectra, Figure 3.52, represent the transition of electrons from Co2*p* to Co3*d* (t_{2g}^{*} and e_g^{*}) orbitals. The sample with Y = 0.01 shows the highest absorption intensity attributing to low electron density in the Co3*d* orbital.

The first peak (~778 eV) of Co2$p_{3/2}$ sub band relates to the transition of electrons from Co2*p* orbital to available t_{2g}^{*} state, which is dominated by HS Co^{3+} [44]. The sample with Y = 0.03 shows the strongest intensity of first peak, indicating the high content of HS Co^{3+}. On the other hand, the weakest intensity of first peak observed on the sample with Y = 0.01 corresponds to the low quantity of HS Co^{3+}.

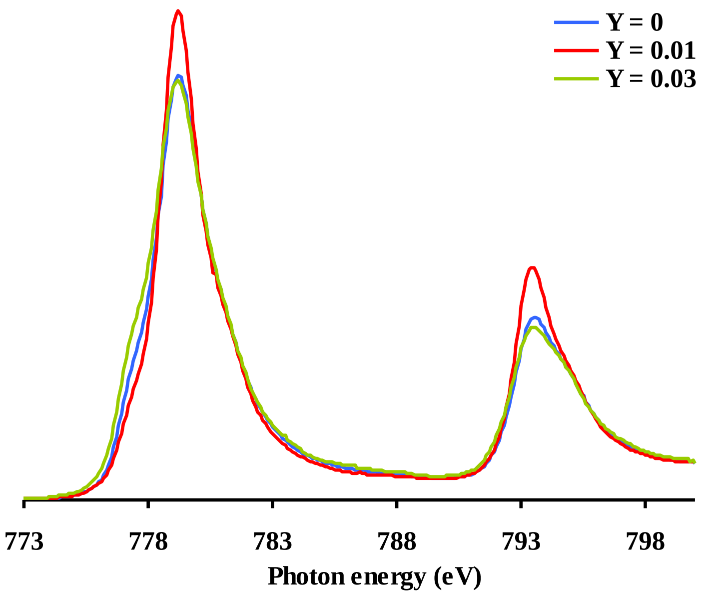

Figure 3.52. Normalized Co L-edge region X-ray absorption spectra of $La_{0.3}Sr_{0.5}Ca_2Co_{0.9-y}Zn_yFe_{0.1}O_3$ (Y = 0, 0.01, 0.03)

3.4.5.3 O K-edge X-ray absorption spectroscopy (O K-edge XAS)

From the O K-edge XAS (Figure 3.53), feature A represents the transition of electrons from O1*s* orbital of lattice O^{2-} to hybridized O2*p*-t_{2g}^* hole state. This feature is dominated by HS Co^{3+}. Feature B and C associate with the transition of electrons from O1*s* orbital of lattice O^{2-} to hybridized O2*p*-e_g^* hole state which is dominated by LS Co^{3+} and IS Co^{4+}, respectively.

It is clear that the peak intensity of feature B and C of the sample with Y = 0.01 is higher than those of Y = 0 and Y = 0.03, respectively. This corresponds to the high quantities of LS Co^{3+} and IS Co^{4+} the series of Y = 0.01 > Y = 0 > Y = 0.03. As reported in section 3.1.6.3 that Co^{2+} will limit the transition of electrons from O1s to hybridized O2*p*-e_g^* hole state. Therefore, it can be concluded that the quantity of Co^{2+} is in the following sequence: Y = 0.03 > Y = 0 > Y = 0.01. For feature A, the sample with Y = 0.03 show the highest absorption intensity followed by the sample with Y = 0 and Y = 0.01, respectively. This suggests the high content of HS Co^{3+} in the series of the sample with Y = 0.03 > Y = 0 > Y = 0.01.

The high content of IS Co^{4+} is a reason for low unit cell parameter, high electrical conductivity and low E_a value of the sample with Y = 0.01 comparing to the sample with Y = 0.03, which exhibits the high quantity of HS Co^{2+} leading to the high unit cell parameter, low electrical conductivity, high E_a value and high oxygen permeation of the material.

Feature D relates to the transition of electrons from σ_{1s} orbital to σ^* resonance of adsorbed O_2^-. The absorption intensity of the sample with Y = 0.03 is higher than those of others, indicating the high content of adsorped O_2^-. This reflects great ORR ability due to the high quantities of HS Co^{2+} and oxygen vacancy.

Feature E corresponds to the transition of electrons from O1*s* orbital of lattice O^{2-} to hybridized O2*p*-La5*d*/Sr4*d* hole state. The highest absorption intensity observed on the sample with Y = 0.03 implies strong hybridization between O2*p* and La5*d*/Sr4*d* due to structural distortion. On the contrary, the sample with Y = 0.01 has the lowest absorption intensity suggesting weak hybridization between O2*p* and La5*d*/Sr4*d* due to weak structural distortion. The result agrees well with La M-edge XAS results.

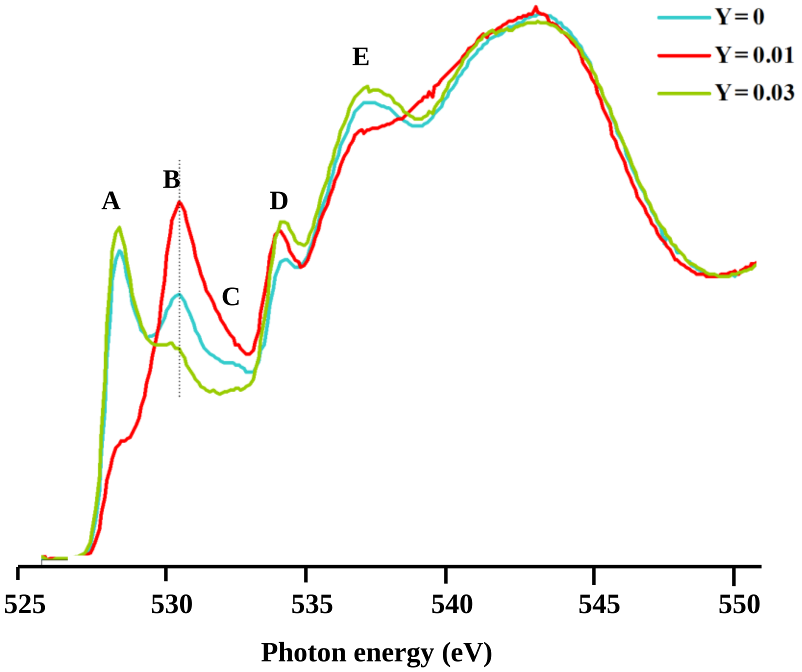

Figure 3.53. Normalized O K-edge region X-ray absorption spectra of $La_{0.3}Sr_{0.5}Ca_2Co_{0.9-y}Zn_yFe_{0.1}O_3$ (Y = 0, 0.01, 0.03)

3.5 Synthesis and properties of $La_{0.3}Sr_{0.5}Ca_{0.2}(Co_{0.9}Fe_{0.1})_{1-y}Zn_yO_3$

3.5.1 XRD analyses

The XRD patterns of $La_{0.3}Sr_{0.5}Ca_{0.2}(Co_{0.9}Fe_{0.1})_{1-y}Zn_yO_3$ (Y = 0, 0.02, 0.04), Figure 3.54, illustrate $SrCoLaO_4$ impurity phase after doping Zn in the structure.

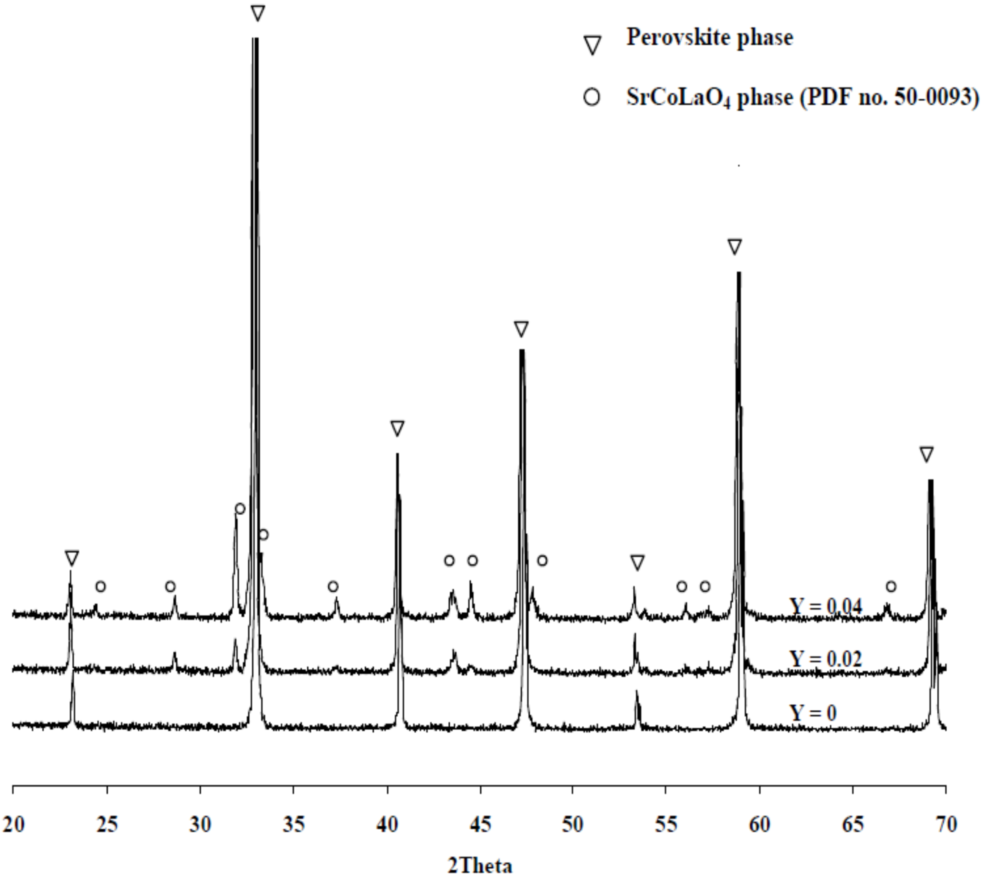

Figure 3.54. XRD patterns of $La_{0.3}Sr_{0.5}Ca_{0.2}(Co_{0.9}Fe_{0.1})_{1-y}Zn_yO_3$ (Y = 0, 0.02, 0.04) sintered at 1200 ^oC for 6 hrs

3.6 Synthesis and properties of $La_{0.3}Sr_{0.5}Ca_{0.2}Co_{0.9-y}Mg_yFe_{0.1}O_3$

3.6.1 XRD analyses

The XRD patterns of $La_{0.3}Sr_{0.5}Ca_{0.2}Co_{0.9-y}Mg_yFe_{0.1}O_3$ (Y = 0 - 0.05) are shown in Figure 3.55. CoO impurity phase is observed after replacing Co with Mg.

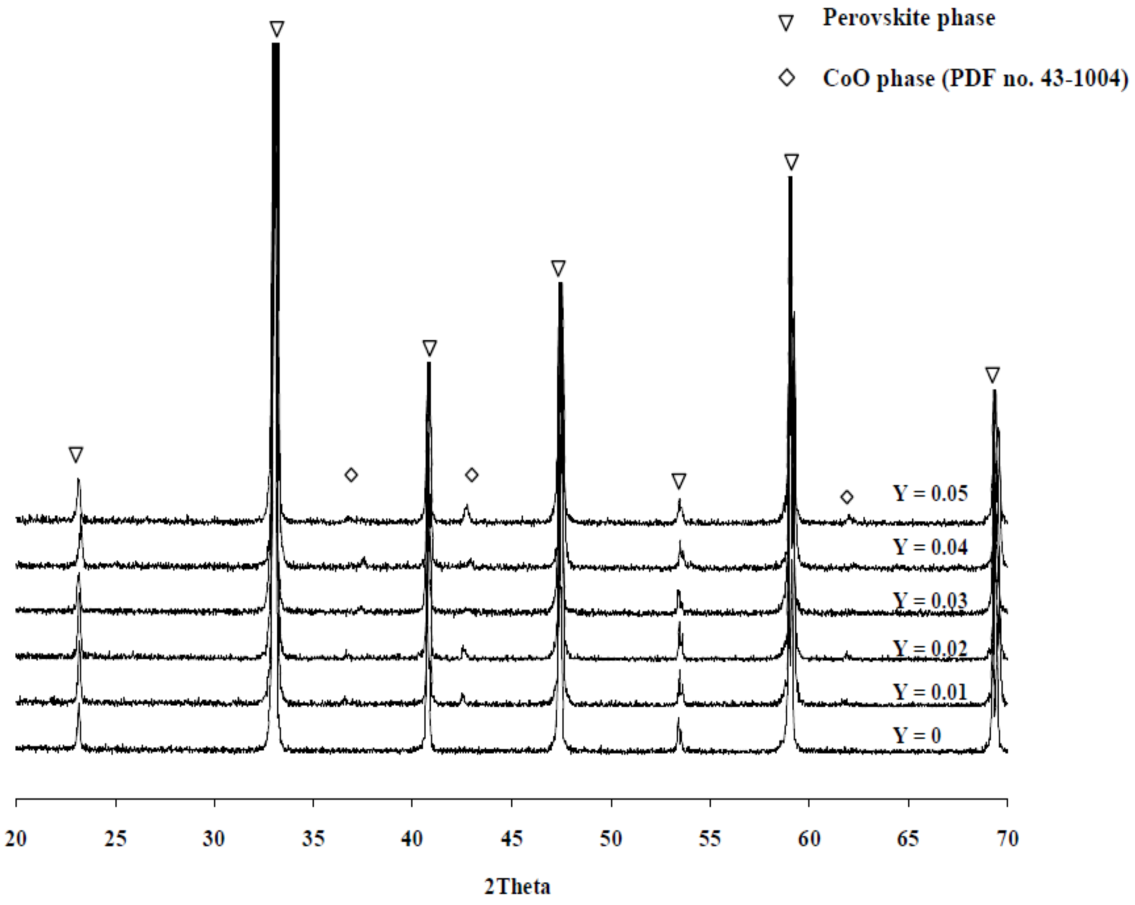

Figure 3.55. XRD patterns of $La_{0.3}Sr_{0.5}Ca_{0.2}Co_{0.9-y}Mg_yFe_{0.1}O_3$ (Y = 0 - 0.05) sintered at 1200 ^{o}C for 6 hrs

3.7 Synthesis and properties of $La_{0.3}Sr_{0.5}Ca_{0.2}(Co_{0.9}Fe_{0.1})_{1-y}Mg_yO_3$

3.7.1 XRD analyses

The XRD patterns of $La_{0.3}Sr_{0.5}Ca_{0.2}(Co_{0.9}Fe_{0.1})_{1-y}Mg_yO_3$ (Y = 0, 0.02, 0.04), Figure 3.56, show CoO and $SrCoLaO_4$ impurity phases when Co and Fe are substituted by Mg.

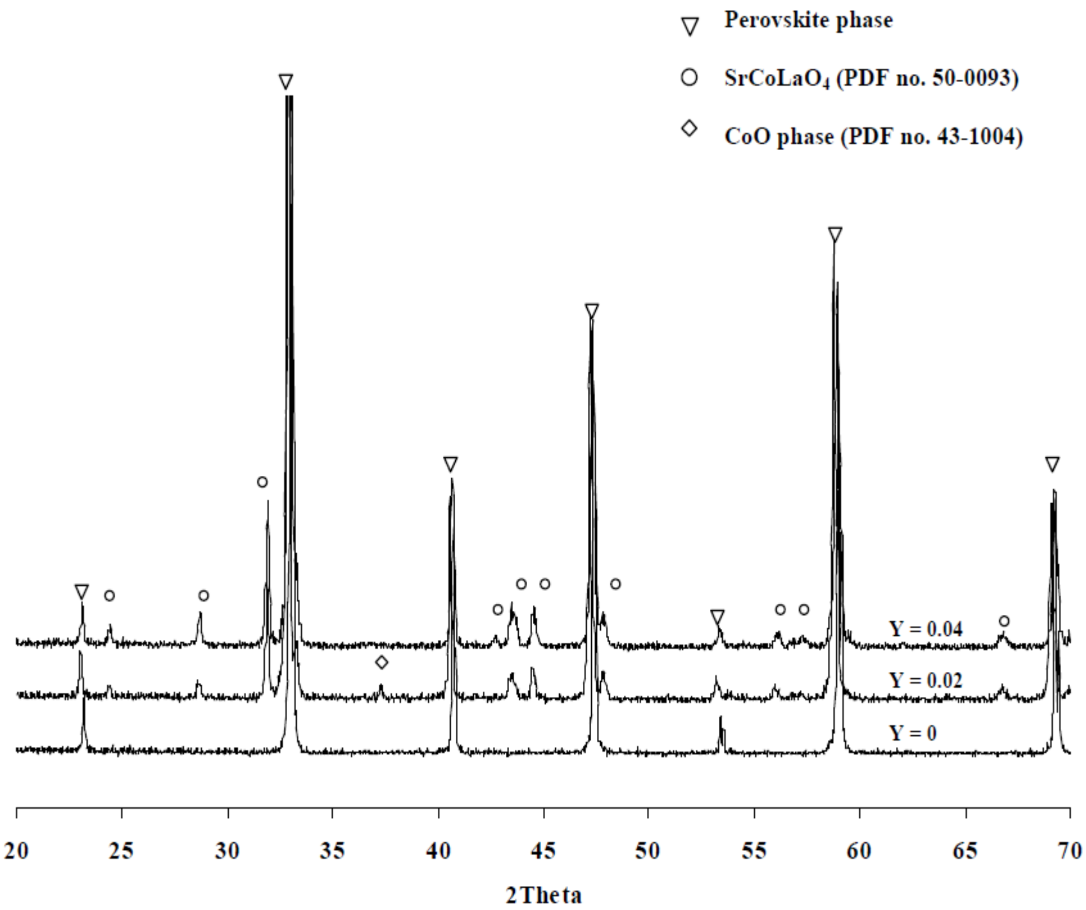

Figure 3.56. The XRD patterns of $La_{0.3}Sr_{0.5}Ca_{0.2}(Co_{0.9}Fe_{0.1})_{1-y}Mg_yO_3$ (Y = 0, 0.02, 0.04) sintered at 1200 C for 6 hrs.

CHAPTER IV

CONCLUSIONS

4.1 Conclusions

The following materials: (a) $La_{0.3}Sr_{0.7}Co_{0.9}Fe_{0.1}O_3$ (LSCF), (b) $La_{0.3}Sr_{0.7-x}Ca_x Co_{0.9}Fe_{0.1}O_3$ (X = 0 - 0.7) and $(La_{0.3}Sr_{0.5})_{1-x}Ca_xCo_{0.9}Fe_{0.1}O_3$ (X = 0 - 0.4), (c) $La_{0.3}Sr_{0.5}Ca_{0.2}Co_{0.9-y}Zn_yFe_{0.1}O_3$ and $La_{0.3}Sr_{0.5}Ca_{0.2}(Co_{0.9}Fe_{0.1})_{1-y}Zn_yO_3$ (Y = 0 - 0.05), and (d) $La_{0.3}Sr_{0.5}Ca_{0.2}Co_{0.9-y}Mg_yFe_{0.1}O$ and $La_{0.3}Sr_{0.5}Ca_{0.2}(Co_{0.9}Fe_{0.1})_{1-y}Mg_yO_3$ (Y = 0 - 0.05), were synthesized by modified citrate method. Phase structure, surface chemistry and bulk properties were examined by XRD, XPS and XAS, respectively. The conducting properties were studied for electrical conductivity and oxygen permeation.

LSCF had a primitive cubic phase with ABO_3-perovskite structure. The electrical conductivity of LSCF sintered at 1100 ^oC exhibited metallic-like behavior whereas LSCFs sintered at higher temperatures exhibited semiconducting-like behavior. LSCF sintered at 1200 ^oC showed the highest oxygen permeation rate, more idealized cubic, a lot of oxygen vacancies and Co^{2+} cations.

$La_{0.3}Sr_{0.7-x}Ca_xCo_{0.9}Fe_{0.1}O_3$ showed pure perovskite structure with primitive cubic form when X = 0 – 0.5, while $(La_{0.3}Sr_{0.5})_{1-x}Ca_xCo_{0.9}Fe_{0.1}O_3$ exhibited pure perovskite structure with primitive cubic and tetragonal form when X = 0 – 0.2 and X = 0.3 – 0.4, respectively. Doping of Ca in the structure improved electrical conductivity due to the increase in the quantities of IS Co^{4+} and HS Co^{3+}. The highest electrical conductivity was achieved on $La_{0.3}Sr_{0.5}Ca_{0.2}Co_{0.9}Fe_{0.1}O_3$.

$La_{0.3}Sr_{0.5}Ca_{0.2}Co_{0.9-y}Zn_yFe_{0.1}O_3$ exhibited pure perovskite phase with primitive cubic structure when Y = 0 – 0.03 whereas $La_{0.3}Sr_{0.5}Ca_{0.2}(Co_{0.9}Fe_{0.1})_{1-y}Zn_yO_3$ exhibited $SrLaCoO_4$ and CoO impurity phases. Doping of Zn in the structure decreased electrical conductivity but increased oxygen permeation because HS $Co^{2+,3+}$ and oxygen vacancies were formed. The highest oxygen permeation rate was achieved on $La_{0.3}Sr_{0.5}Ca_{0.2}Co_{0.87} Zn_{0.03}Fe_{0.1}O$.

$La_{0.3}Sr_{0.5}Ca_{0.2}Co_{0.9-y}Mg_yFe_{0.1}O_3$ and $La_{0.3}Sr_{0.5}Ca_{0.2}(Co_{0.9}Fe_{0.1})_{1-y}Mg_yO_3$ showed CoO and $SrLaCoO_4$ impurity phases when Mg was introduced into the structure.

This work successfully improves electrical conductivity and oxygen permeation of LSCF by doping Ca^{2+} and Zn^{2+}, respectively. $La_{0.3}Sr_{0.5}Ca_{0.2}Co_{0.87}Zn_{0.03}Fe_{0.1}O$ is a good candidate for cathode material in SOFC because of its high electrical conductivity and oxygen permeation.

4.2 Suggestion

1) Sr, Fe, Ca, Mg and Zn should be characterized by XAS in order to obtain more details about oxidation state, electronic configuration, structural distortion and oxygen vacancy of the material.

2) The compatibility with electrolytes, and cell performance of $(La_{0.3}Sr_{0.5})_{0.9}Ca_{0.1}Co_{0.9}Fe_{0.1}O_3$ and $La_{0.3}Sr_{0.5}Ca_{0.2}Co_{0.87}Zn_{0.03}Fe_{0.1}O$ should be tested because these samples show good properties in both electrical conductivity and oxygen permeation.

REFERENCES

[1] Stambouli, A. B., Traversa, E. Solid oxide fuel cells (SOFCs): a review of an environmentally clean and efficient source of energy. Renewable & Sustainable Energy Reviews 6 (2002) : 433–455.

[2] Singhal, S.C. Advances in solid oxide fuel cell technology. Solid State Ionics 135 (2000) : 305–313.

[3] Song, C. Fuel processing for low-temperature and high-temperature fuel cell challenges, and opportunities for sustainable development in the 21th century. Catalysis Today 77 (2002): 17-47.

[4] Minh, N.Q. Ceramic Fuel Cells. Journal of the American Ceramic Society 76 (1993) : 563-588.

[5] Escudero M.J., Aguadero, A., Alonso, J.A., Daza, L. A kinetic study of oxygen reduction reaction on La_2NiO_4 cathode. Electroanalytical chemistry 115 (2007) : 107-116.

[6] Sammes, N.M., Cai, Z. Ionic conductivity of ceria/yttria stabilized zirconia electrolyte materials. Solid State Ionic 100 (1997) : 39-44.

[7] Johnsson, M., Lemmens, P. Crystallography and Chemistry of Perovskites [online]. (n.d.). Available from: http://onlinelibrary.wiley.com/doi/10.1002/9780 470022184.hmm411/full [2013, January 2]

[8] Perovskite structure [online]. Available from: http://pubs.rsc.org/en/content/articlelanding/2006/cp/b600485g [2012,December 8]

[9] Richer, J., Holtappels, P., Graule, T., Nakamura, T., Gauckler, J.L. Materials design for perovskite SOFC cathodes. Monatshefte fur Chemie 140 (2009) : 985-999.

[10] Tai, L.W., Nasrallah, M.M., Anderson, H.U., Sparlin, D.M., Sehlin, S.R. Structure and electrical properties of $La_{1-x}Sr_xCo_{1-y}Fe_yO_3$. Part 1. The system $La_{0.8}Sr_{0.2}Co_{1-y}Fe_yO_3$. Solid State Ionics 76 (1995) : 259-271.

[11] Tai, L.W., Nasrallah, M.M., Anderson, H.U., Sparlin, D.M., Sehlin, S.R. Structure and electrical properties of $La_{1-x}Sr_xCo_{1-y}Fe_yO_3$. Part 2. The system $La_{1-x}Sr_xCo_{0.2}Fe_{0.8}O_3$. Solid State Ionics 76 (1995) : 273-283.

[12] Carter, S., Selcuk, A., Chater, R.J., Kajda, J., Kilner, J.A., Steele, B.C.H. Oxygen transport in selected nonstoichiometric perovskite-structure oxides. Solid State Ionics 53 (1992) : 579-605.

[13] Ullman, H., Trofimenko, N., Khanbu, A.A. Correlation between thermal expansion and oxide ion transport in mixed conduction perovskite-type oxide for SOFC cathodes. Solid State Ionics 138 (2000) : 79-90.

[14] Thursfield, A., Metcalfe, I.S. The use of dense mixed ionic and electronic conductivity membranes for chemical production. Journal of Materials Chemistry 14 (2004) : 2475-2485.

[15] Kharton, V.V., Viskup, A.P., Marozau, I.P., Naumovich, E.N. Oxygen permeability of perovskite-type $Sr_{0.7}Ce_{0.3}MnO_3$. Materials Letters 57 (2003) : 3017-3021.

[16] Suzuki, M., Suzuki. I.S. Lecture note on solid state physics, Superexchange interaction [online]. (n.d.). Available from: www.binghamton.edu/physics/ docs/super-exchange.pdf [2013, January 2].

[17] Cousin, P., Ross, R.A. Preparation of mixed oxide: a review. Materials Science and Engineering A-Structural Materials Properties Microstructure and Processing 130 **(1990)** : 119-125.

[18] Nagamoto, H., Hayashi, K., Inoue, H. Methane oxidation by oxygen transported through solid electrolyte. Journal of Catalysis 126 (1990) : 671-673.

[19] Lenntech. Calcination [Online]. Available from:http://www.lenntech.com/ chemistry/calcination.htm [2012, December 17]

[20] Kuczynski, G.C. Transaction of the American Institute of Mining, Metallurgical, and Petroleum Engineering. Journal of Applied Physisc 21 (1950) : 632-637.

[21] Sintering mechanism [online]. Available from: http://www.substech.com/ dokuwiki/doku.php?id=sintering_of_ceramics [2012, December 17]

[22] Mineshige, A., Kobune, M., Fujii, S., Ogumi, Z., Inaba, M., Yao, T., Kikuchi, K. Metal-insulator transition and crystal structure of $La_{1-x}Sr_xCoO_3$ as functions of Sr-content, temperature and oxygen partial pressure. Journal of Solid State Chemistry 142 (1999) : 374-381.

[23] Hueso, J.L., Holgado, J.P., Pereniguez, R., Mun, Simon., Salmeron, M. Chemical and electronic characterization of cobalt in a lanthanum perovskites. Journal of Solid State Chemistry 183 (2010) : 27-32.

[24] Cherry, M., Islam, M.S., Catlow, C.R.A. Oxygen ion migration in perovskite-type oxides. Journal of Solid State Chemistry 118 (1995) :125-132.

[25] Petric, A., Huang, P., Tietz, F. Evaluation of La–Sr–Co–Fe–O perovskites for solid oxide fuel cells and gas separation membranes. Solid State Ionics 135 (2000) : 719-725.

[26] Onuma, S., Yashiro, K., Miyoshi, S., Kaimai, A., Matsumoto, H., Nigara, Y., Kawada, T., Mizusaki, J., Kawamura, K., Sakai, N., Yokokawa, H. Oxygen nonstoichiometry of the perovskite-type oxide $La_{1-x}Ca_xCrO_3$ (x = 0.1, 0.2, 0.3). Solid State Ionics 174 (2004) : 287-293.

[27] Ding, X., Gao, L., Liu, Y., Zhen, Y. Thermal expansion and electrochemical properties of $La_{0.7}AE_{0.3}CuO_3$ (AE = Ca, Sr, Ba) cathode materials for IT-SOFCs. Journal of Electroceramics 18 (2007) : 317-322.

[28] Hung, M.H., Madhava Rao M.W., Tsai D.S. Microstructures and electrical conductivities of calcium substituted $LaFeO_3$ as SOFC cathode. Matererials Chemistry and Physics 101 (2007) : 297-302.

[29] Xia, T., Liu, X.D., Li, Q., Menga, J., Cao, X.Q. Synthesis, structural and electrical characterizations of $Sr_2Fe_{1-x}M_xNbO_6$ (M = Zn and Cu) with double perovskite structure. Journal of Alloys and Compounds 422 (2006) : 264-272.

[30] Lakshminarayanan, N., Choi, H., Kuhn, J.N., Ozkan, U.S. Effect of additional B-site transition metal doping on oxygen transport and activation characteristics in $La_{0.6}Sr_{0.4}(Co_{0.18}Fe_{0.72}X_{0.1})O_3$ (where X= Zn, Ni or Cu) perovskite oxides. Applied Catalysis B : Environmental 103 (2011) : 318-325.

[31] Vijayanandhini, K., Kutty, T.R.N. Effects of Zn substitution on the magnetic and transport properties of $La_{0.6}Sr_{0.4}Mn_{1-y}Zn_yO_3$ ($0 \leq y \leq 0.3$). Solid State Communications 141 (2007) : 252-257.

[32] Datta, P., Majewski, P., Aldinger, F. Structural studies of Sr- and Mg-doped $LaGaO_3$. Journal of Alloys and Compounds 438 (2007) : 232-237.

[33] Choi, S.M., Lee, K.T., Kin, S., Chun, M.C., Lee, H.L. Oxygen ion conductivity and cell performance of $La_{0.9}Ba_{0.1}Ga_{1-x}Mg_xO_3$ electrolyte. Solid State Ionics 131 (2000) : 221-228.

[34] Suresh, M.B., Yeh, T-H., Chou, C-C. Zn doped LSCF as a novel cathode material for solid oxide fuel cell. Integrated Ferroelectrics 121 (2010) : 113-119.

[35] Tkach, A., Vilarinho, P.M., Kholkin, A. Effect of Mg doping on the structural and dielectric properties of strontium titanate ceramics. Applied Physisc A 79 (2004) : 2013-2020.

[36] Kostogloudis, G.C., Fertis, P., Ftikos, C.H. Electronic conductivity in the $Pr_{1-x}Sr_xCo_{1-y}Mn_yO_3$ system. Solid State Ionic 118 (1999) : 241-249.

[37] Shannon, R.D. Revised effective ionic radii and systematic studies of interatomic distances in halides and chalcogenides. Acta Crystallographica Section A 32 (1976) : 751-767.

[38] Sagdahl, L.T., Einarsrud, M.A., Grande, T. Sintering behaviour of $La_{1-x}Sr_xFeO_3$ mixed conductors. Journal of the European Ceramic Society 26 (2006) : 3665-36673.

[39] Vashook, V., Franke, D., Vasylechko, L., Fichtner, W., Schmidt, M., Wen, T.L., Guth, U. Electrical conductivity and oxygen non-stoichiometry of the double B mixed perovskite series $La_{0.6}Ca_{0.4}Mn_{1-y}Me_yO_3$ with Me = Fe, Co, Ni and Y = 0 – 0.6. Solid State Ionics 179 (2008) : 1101 – 1107.

[40] Kharton, V.V., Figueiredo, F.M., Kovalevsky, A.V., Viskup, A.P., Bashmakov, I.A., Marques, F.M.B. Processing, microstructure and properties of $LaCoO_3$ ceramic. Journal of the European Ceramic Society 21 (2001) : 2301–2309.

[41] Mineshige, A., Kobune, M., Fujii, S., Ogumi, Z., Inaba, M., Yao,T., Kikuchi, K. Metal-insulator transition and crystal structureof $La_{1-x}Sr_xCoO_3$ as functions of Sr-content, temperature and oxygen partialpressure. Journal of Solid State Chemistry 142 (1999) : 374–381.

[42] Potze, R.H., Sawatzky, G.A., Abbate, M. Possibility for an intermediate-spin ground state in the charge-transfer material $SrCoO_3$. Physical Review B 51 (1995) : 11501-11506.

[43] Koc, R., Anderson, H.U. Electrical and Thermal Transport Properties of $(La,Ca)(Cr,Co)O_3$. Journal of the European Ceramic Society 15 (1995) : 867 – 874.

[44] Hu, Z., Grazioli, C., Knupfer, M., Mazumdar, C., Kaindl, G. Difference in spin state and covalence between $La_{1-x}Sr_xCoO_3$ and $La_{2-x}Sr_xLi_{0.5}Co_{0.5}O_4$. Journal of Alloys and Compounds 343 (2002) : 5-13.

[45] Kharton, V.V., Naumovich, E.N., Kovalevsky, A.V., Viskup, A.P., Figueredo, F.M., Bashmakov, I.A. Mixed electronic and ionic conductivity of $LaCo(M)O_3$ (M = Ga, Cr, Fe or Ni): Effect of preparation method on oxygen transport in $LaCoO_3$. Solid State Ionics 138 (2000) : 135–148.

[46] Yoon, W.S., Kim, K.B., Kim, M.G., Lee, J.S., Shin, H.J., Yo, C.H. Oxygen contribution on Li-ion intercalation in $LiCoO_2$ investigated by O K-Edge and Co L-Edge X – ray absorption spectroscopy. Journal of Physical Chemistry B 106 (2002) **:** 2526 – 2532.

[47] Singh, K., Acharya, S., Atkare, D.V. Qualitative analysis of tolerance factor, electronegativity and chemical bonding of some ferroelectric perovskites through MOT. Ferroelectrics 315 (2005) : 91-110.

[48] Batis, N.H., Delichere, P., Batis, H. Physicochemical and catalytic properties in methane combustion of $La_{1-x}Ca_xMnO_3$ ($0 \leq X \leq 1$; $-0.04 \leq Y \leq 0.24$) perovskite-type oxide. Applied Catalysis A : General 282 (2005) : 173-180.

[49] Polini, R., Falsetti, A., Traversa, E., Schaf, O., Knauth, P. Sol–gel synthesis, X-ray photoelectron spectroscopy and electrical conductivity of Co-doped $(La,Sr)(Ga,Mg)O_3$ perovskites. Journal of the European Ceramic Society 27 (2007) : 4291– 4296.

[50] Mickevicius, S., Grebinskij, S., Osinniy, V., Druebe, W. Investigation of epitaxial $LaNiO_3$ thin films by high-energy XPS. Journal of Alloys and Compounds 423 (2006) : 107-111.

[51] O’ Connell, M., Norman, A.K., Morris, M.A. Catalytic oxidation over lanthanum-transition metal perovsite materials. Catalysis Today 47 (1999) : 123-132.

[52] Lui, B., Zhang, Y., Tang, L. X-ray photoelectron spectroscopic studies of $Ba_{0.5}Sr_{0.5}Co_{0.8}Fe_{0.2}O_3$ cathode for solid oxide fuel cells. International Journal of Hydrogen Energy 34 (2009) : 435-439.

[53] Barr, T.L. An ESCA study of the termination of the passivation of elemental metals. Journal of Physical Chemistry 82 (1978) : 1081.

[54] Qiu, S.L., Lin, C.L., Chen, J., Stongin, M. Photoemission studies of the low-temperature reaction of metals and oxygen. Physical Review B 41 (1990) : 7467-7473.

[55] Qiu, S.L., Lin, C.L., Chen, J., Stongin, M. The formation of metal-oxygen species at low temperature. Journal of Vacuum Science and Technology 8 (1990) : 2595.

[56] Kaliaguine, S., Van Neste, A., Szabo, V., Muzychuk, R. Perovskite-type oxide synthesized by reactive grinding Part I. Preparation and characterization. Applied Catalysis A 209 (2001) : 345-358.

[57] Bucher, E., Sitte, W., Klauser, F., Bertel, E. Oxygen exchange kinetics of $La_{0.58}Sr_{0.4}Co_{0.2}Fe_{0.8}O_3$ at 600 ^oC in dry and humid atmospheres. Solid State Ionics 191 (2011) : 61-67.

[58] Tabata, K., Matsumoto, I., Kohiki, S. Surface characterization and catalytic properties of $La_{1-x}Sr_xCo_3$. Journal of Matterials Science 22 (1987) : 1882-1886.

[59] Barreca,D., Massignan, C., Armelao, L., Tondello, E. Composition and microstructure of cobalt oxide thin films obtained from a novel cobalt (II) precursor by chemical vapor deposition. Chemistry of Materials 13 (2001) : 588-593.

[60] Ivanova, T., Naumkin, A., Sidorov, A., Kiskin, M. X-ray photoelectron spectra and electron structure of polynuclear cobalt complexes. Journal of Electron Spectroscopy and Related Phenomena 156 (2007) : 200-203.

[61] Okamoto, Y., Nakano, H., Imanaka, T., Teranishi, S. X-ray photo electron spectroscopic studies of catalysts-supported cobalt catalysts. Bulletin of the Chemical Soceity of Japan 48 (1975) : 1163-1168.

[62] Briggs, D., Gibson, V.A. Direct observation of multiplet splitting in 2*p* photoelectron peaks of cobalt complexes. Chemical Physics Letters 25 (1974) : 493-496.

[63] Ichimura, K., Inoue, Y., Yasumori, I. Catalyst by mixed oxide perovskites. I. hydrogenolysis of ethylene and ethane on $LaCoO_3$. Bulletin of the Chemical Soceity of Japan 53 (1980) : 3044-3049.

[64] Carlson, T.A., Carver, J.C., Seathre, L.J., Vernon, G.A. Multicomponent structure in x-ray photoelectron spectroscopy of transition metal compounds. Journal of Electron Spectroscopy and Related Phenomena 5 (1974) : 247-258.

[65] Wallbank, B., Main, I.G., Johnson, C.E. 2*p* and 2*s* shake-up satellites in solid compounds of 3*d* ions. Journal of Electron Spectroscopy and Related Phenomena 5 (1974) : 259-266.

[66] Kim, K.S., Winograd, N. Charge transfer shake-up saterllites in x-ray photoelectron spectra of cations and anions of $SrTiO_3$, TiO_2 and Sc_2O_3. Chemical Physics Letters 31 (1975) : 312-317.

[67] Kim, K.S. Charge transfer transition accompanying x-ray photoionization in transition-metal compounds. Journal of Electron Spectroscopy and Related Phenomena 3 (1974) : 217-226.

[68] Frost, D.C., McDowell, C.A., Wallbank, B. Charge transfer shake-up satellites in x-ray photoelectron spectra of solid compounds of $3d^0$ ions. Chemical Physics Letters 40 (1976) : 189-193.

[69] Karvonen, L., Valkeapää, M., Lui, R-S., Chen, J-M., Tamauchi, H., Karppinen, M. O-K and Co-L XANES study on oxygen intercalation in perovskite $SrCoO_3$. Chemistry of Matererials 22 (2010) : 70-76.

[70] Wu, Z.Y., Benfatto, M., Pedio, M., Cimino, R., Mobilio, S., Barman, S.R., Maiti, K., Sarma, D.D. Theoretical analysis of X-ray-absorption near-edge fine structure at the O and metal K edges of $LaFeO_3$ and $LaCoO_3$. Physical Review B 56 (1997) : 2228-2233.

[71] Molecular orbital of O_2 [online]. Available from: http://en.citizendium.org/wiki/ oxidative_stress [2013, January 2]

[72] Toulemone, O., Guyen, N.N., Studer, F. Spin state transition in $LaCoO_3$ with temperature or strontium doping as seen by XAS. Journal of Solid State Chemistry 158 (2001) : 208-217.

[73] Ravindran, P., Korzhavyi, P.A., Fjellvag, H., Kjekshus, A. Electronic structure, phase stability, and magnetic properties of $La_{1-x}Sr_xCoO_3$ from first-principles full-potential calculations. Physical Review B 60 (1999) **:** 16423-16427.

[74] Abbate, M., Zampieri, G., Okamoto, J., Fujimori, A., Kawasaki, S., Takano, M. X-ray absorption of the negative charge-transfer material $SrFe_{1-x}Co_xO_3$. Physical Review B 65 (2002) : 165120-165126.

[75] Imamura, M., matsubayashi, N., Shimada, H. Catalytically active oxygen species in $La_{1-x}Sr_xCoO_3$ studied by XPS and XAFS spectroscopy. Journal of Physical Chemistry B 104 (2000) : 7348-7353.

[76] Merino, N.A., Babero, B.P., Eloy, P., Cadus, L.E. $La_{1-x}Ca_xCoO_3$ perovskite-type oxide: Identification of the surface oxygen species by XPS. Applied Surface Science 253 (2006) : 1489-1494.

[77] Rousseua, S., Loridant, S., Delichere, P., Vernoux, P. $La_{1-x}Sr_xCo_{1-y}Fe_yO_3$ perovskites prepared by sol-gel method: Characterization and relationships with catalytic properties for total oxidation of toluene. Applied Catalysis B 88 (2009) : 438-443.

[78] Ji, X., Chen, Y., Zhao, G., Wang, X., Liu, W. Tribological properties of $CaCO_3$ nanoparticles as an additive in lithium Grease. Tribology Letters 41 (2011) : 113-119.

[79] Cai, Z., Kubicek, M., Fleig, J., Yildiz, B. Chemical heterogeneities on $La_{0.6}Sr_{0.4}CoO_3$ thin film-Correlations to cathode surface activity and stability. Chemistry of Materials 24 (2012) : 1116-1127.

[80] Diethelm, S., Herle, J.V., Sfeir. J., Buffat, P. Correlation between oxygen transport properties and microstructure in $La_{0.5}Sr_{0.5}FeO_3$. Journal of the European Ceramic Society 25 (2005) : 2191–2196.

APPENDICES

APPENDIX A

Ionic radii of some metal ions

Table A.1 Ionic charge, coordination number, and ionic radii of concerned metal ions [37].

Metal ion	Ionic charge	Coordination No.	Ionic radius (Å)
La	3+	12	1.36
Sr	2+	12	1.44
Ca	2+	12	1.34
Co	2+ (HS)	6	0.745
	2+ (LS)		0.65
	3+ (HS)		0.61
	3+ (LS)		0.545
	4+ (HS)		0.53
Fe	2+ (HS)	6	0.78
	2+ (LS)		0.61
	3+ (HS)		0.645
	3+ (LS)		0.55
	4+		0.585
Zn	2+	6	0.74
Mg	2+	6	0.72

HS = High spin configuration, LS = Low spin configuration

APPENDIX B

Activation energy (E_a)

Arrhenius equation (B.1) is shown below. The plot of lnσT versus 1000/T(K) gives a straight line, whose slope can be used to determine the E_a of small polaron conduction.

$$\sigma = (A/T)e^{(-Ea/RT)}$$

$$\ln(\sigma T) = \ln A\ e^{(-Ea/RT)}$$

$$\ln(\sigma T) = \ln e^{(-Ea/RT)} + \ln A \tag{B.1}$$

$$\underbrace{\ln(\sigma T)}_{\text{y}} = \underbrace{(-E_a/R)}_{\text{slope}}\ \underbrace{(1000/T)}_{\text{x}} + \underbrace{\ln A}_{\text{intercept y axis}}$$

$$-E_a/R = \text{Slope of the linear}$$

$$E_a = -\text{slope x R}$$

Where A = material constant including the carrier concentration term

σ = specific conductivity (S/cm)

E_a = activation energy (kJ/mol)

T = temperature (K)

R = gas constant = 8.314472 J/K.mol

VITAE

Mr. Anucha Koedtruad was born on December 11, 1987 in Khon Kaen, Thailand. He graduated with Bachelor's Degree in Chemistry (2nd class honor) from Faculty of Science, Chulalongkorn University in 2009. He continued the Master's degree in program of Chemistry (Inorganic Chemistry), Faculty of Science, Chulalongkorn University in 2010 and completed in 2012.

PRESENTATION

October 17-19, 2009.

Poster Presentation: "EFFECTS OF SINTERING TEMPERATURE ON PROPERTIES OF $La_{0.3}Sr_{0.7}Co_{0.9}Fe_{0.1}O_3$ PEROVSKITES" The 38th congress on science and technology of Thailand (STT38), Empress Convention Center, Chiang Mai, Thailand.

His present address is 173 M.11, Tasala sub-distric, Manchakiri district, Khon Kaen, Thailand 40160. Tel: 087-7152646, E-mail: nuchy_kt@hotmail.com